Marco António Ferreira Pinto

IMPLEMENTATION OF A CYCLOTRON-BASED NEUTRON BEAMLINE: A VIABILITY STUDY

Dissertação de Mestrado na área científica de Engenharia Biomédica, especialidade Imagem e Radiação, orientada pelos Professor Doutor Rui Ferreira Marques, Professor Doutor Francisco Alves e Professor Doutor Paulo Crespo e apresentada ao Departamento de Física da Faculdade de Ciências e Tecnologia da Universidade de Coimbra.

Setembro de 2010

Universidade de Coimbra

Implementation of a Cyclotron-Based Neutron Beamline: A Viability Study

Physics Department
Faculty of Sciences and Technology
University of Coimbra

To obtain the degree of
Master of Science in Biomedical Engineering

M.Sc. dissertation

Marco António Ferreira Pinto
Coimbra, Portugal

September 2010

Supervisor:	Prof. Dr. Rui Ferreira Marques
Co-supervisor:	Prof. Dr. Francisco Alves
Co-supervisor:	Prof. Dr. Paulo Crespo

Submission date:	06.09.2010
Public examination date:	14.09.2010

There are no physicists in the hottest parts of hell,
because the existence of a 'hottest part' implies a temperature difference,
and any marginally competent physicist would immediately use this to run a heat engine
and make some other part of hell comfortably cool.
This is obviously impossible.

Richard Davisson

Para todos os que me têm aturado ...

Index

List of Figures

List of Tables

List of Acronyms and Abbreviations

BNCT	Boron Neutron Capture Therapy
CCD	Charge-Coupled Device
CF	Compound Factor
DNA	Deoxyribonucleic Acid
GBM	Glioblastoma Multiforme
GdNCT	Gadolinium Neutron Capture Therapy
IAEA	International Atomic Energy Agency
ICNAS	Instituto de Ciências Nucleares Aplicadas à Saúde, Coimbra, Portugal
LET	Linear Energy Transfer
MRI	Magnetic Ressonance Imaging
NAA	Neutron Activation Analysis
NCT	Neutron Capture Therapy
PLD	Potentially Lethal Damage
RBE	Relative Biological Effectiveness
SLD	Sublethal Damage

Visão global

Sumário

Têm sido instalados um pouco por todo o mundo ciclotrões capazes de acelerar protões até 20 MeV, principalmente para produção de radioisótopos para tomografia por emissão de positrões. No entanto, muitos desses ciclotrões estão equipados com várias linhas de feixe que podem ser usadas para outros fins, nomeadamente investigação científica. Cada linha de feixe consegue ter tipicamente uma corrente de protões até 150 μA (10^{15} partículas/s). Neste trabalho é estudada a viabilidade de implementar um sistema experimental de produção de neutrões numa das linhas de feixe do ciclotrão de protões recentemente instalado na Universidade de Coimbra, Portugal. Cada linha de feixe consegue entregar protões com energia de 18 MeV. Uma implementação deste tipo poderia permitir estudos de radiobiologia (incluindo BNCT - terapia de captura de neutrões com boro, boron neutron capture therapy, em inglês). Outras utilizações incluem terapia de neutrões rápidos, investigação de materiais, imagem biomédica, segurança interna e investigação fundamental em física, entre outras.

Objectivos desta dissertação

Este estudo é essencialmente um estudo de viabilidade, um estudo de pré-implementação. Nele tentam dar-se respostas e soluções para uma eventual instalação de um sistema de produção de neutrões. Todo este estudo foi feito com o auxílio de ferramentas de simulação de Monte Carlo e várias opções foram exploradas.

Esboço deste trabalho

O primeiro capítulo é uma introdução aos conceitos físicos do trabalho. Não se pretende que este capítulo seja muito exaustivo, muito pelo contrário: é uma forma de delinear as bases físicas necessárias para compreender o trabalho, tanto para quem lê como para quem escreve. O capítulo começa com um sumário do processo de fragmentação (spallation process, em inglês) e as reacções nucleares que lhe estão associadas nas energias relevantes deste trabalho. Seguidamente são descritas algumas das características relacionadas com neutrões no que concerne às suas interacções com a matéria, energias e fontes. O capítulo termina com a descrição das características do ciclotrão instalado na Universidade de Coimbra no Instituto de Ciências Nucleares Aplicadas à Saúde (ICNAS).

No capítulo 2 são revistas algumas das possíveis aplicações que um feixe de neutrões poderá ter. Este capítulo inicia com a apresentação da terapia de captura de neutrões com boro, passando pela imagem com neutrões e terminando na análise por activação com neutrões (neutron activation analysis, em inglês). Neste capítulo o enfoque está no BNCT pois foi a pensar nessa aplicação que este estudo se iniciou. No entanto, rapidamente se verificou que

várias outras aplicações seriam possíveis e portanto duas delas são incluídas também.

Como foram usadas ferramentas de simulação genéricas, não criadas para os objectivos deste trabalho, é prudente recorrer a validações que permitam inferir se as simulações serão fiáveis. Este trabalho de validação é descrito no capítulo 3.

No capítulo 4 encontra-se o estudo, por simulação, das possibilidades para implementar o feixe de neutrões e as características que se podem esperar desse mesmo feixe.

Por fim, as conclusões desta dissertação e sugestões para trabalho futuro são apresentadas no capítulo 5.

Overview

Summary

Cyclotrons capable of accelerating protons up to 20 MeV have been worldwide installed, mainly for positron emission tomography radioisotope production. Nevertheless, most of these cyclotrons are equipped with several beamlines which may be used for other purposes, namely scientific research. Each beamline may typically deliver proton currents up to 150 μA (10^{15} particles/s). Here it is study the viability of implementing an experimental setup dedicated to neutron production at one of the beamlines of the 18-MeV proton cyclotron recently installed at the University of Coimbra, Portugal. Such implementation of a neutron beamline should allow radiobiological studies (including BNCT - boron neutron capture therapy) to be performed. Possible fall out applications comprise, besides neutron-based radiobiology, fields such as fast neutron therapy, materials research, biomedical imaging, homeland security, and fundamental research in physics, among others.

Objectives of this dissertation

This study is essentially a feasibility study. Here we try to give answers and solutions for an eventual implementation of a neutron beamline. The entire study was made with Monte Carlo simulation tools and several options were explored.

Outline

The first chapter is an introduction to the physical concepts needed for this work. It is not intended to be a very thorough chapter, quite the contrary: it is a way to delineate the physical basis necessary to understand this work, both for those who read and write. The chapter begins with a summary of the spallation process and the nuclear reactions related to it, and with the energies relevant for this work. Some of the characteristics associated with neutrons such as their interactions with matter, energy ranges, and sources are presented after. The chapter ends with a description of the cyclotron installed at the University of Coimbra in Instituto de Ciências Nucleares Aplicadas à Saúde (ICNAS).

In chapter 2 a review is made about some possible applications that a neutron beam may have. This chapter begins with the presentation of boron neutron capture therapy (BNCT) and then neutron imaging and neutron activation analysis are also focused. In this chapter BNCT is more discussed because it was the trigger of this study. However, it was realized soon that several other applications are possible and therefore two of them are also included.

Since generic simulation tools were used, it is prudent to use validations that should infer if the simulations are reliable. This validation work is described in chapter 3.

In Chapter 4 the simulation study is presented together with some of the possibilities to implement the neutron beam and the characteristics that might be expected of such beam.

The conclusions from this dissertation, together with future work suggestions, are presented in chapter 5.

Part I

Introduction

Chapter 1

Physics Background

1.1 Spallation process

The word spallation comes from spall and it means small pieces of material that are ejected from a target after some sort of projectile collides with it. There is no general definition of the term 'spallation reaction', nevertheless this type of reaction is observed in astrophysics, geophysics, radiotherapy, radiobiology, and at all applications together with accelerators [Fil09]. But for all practical purposes, spallation refers to nonelastic nuclear reactions that occur when energetic particles interact with an atomic nucleus. These particles can be protons, neutrons or pions [Fil09]. Although one possible definition refers to a minimum energy of the incident particles around tens of MeV, there is no clear separation of spallation from the lower energy nuclear reactions [Fil09]. A definition for spallation to be specified in the context of accelerator driven systems or high-intensity neutron sources is *the disintegration of a nucleus by means of high energetic proton-induced reactions* [Fil09]. Assuming that the projectile has sufficient energy to break the Coulomb barrier, two main nuclear reactions can occur, compound-nucleus reaction and/or direct reaction.

1.1.1 Compound-nucleus reaction

This kind of reaction assumes the formation of an intermediate state before the release of the outgoing particles. Admitting that the projectile has sufficient energy to overcome the Coulomb barrier, this reaction begins when the projectile enters the target nucleus and interacts with one of the nucleons. After this first step, the less energetic projectile and the recoiling nucleon will have successive collisions and the process carries on until there is no excess energy available. In this intermediate state a combined system between projectile and nucleus is created (compound-nucleus). Although the average energy gain per nucleon is small and not enough for ejection to occur, statistically some (few) nucleons may exist with sufficient energy to escape the nucleus (Figure 1.1) [Kra88].

1.1.2 Direct reaction

Direct reactions are those in which the interaction occurs primarily with only one nucleon and at the surface of the target nucleus, so they are also known as peripheral reactions. The probability of this type of reaction increases with increasing projectile energy (or with the

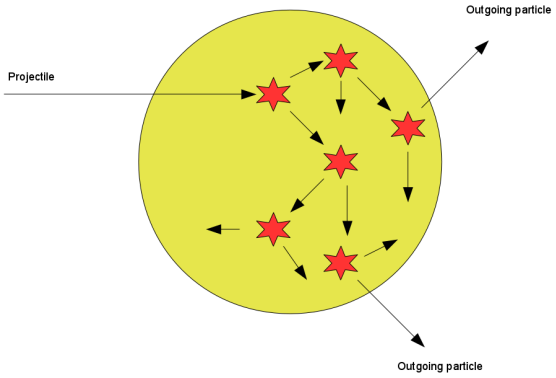

Figure 1.1: Compound-nucleus reaction scheme. Up to 10^{-16} s the outgoing particles are nucleons, and after, if emission occurs, gammas are produced [Kra88]. Image for illustrative purposes only without considering all possibilities.

decrease of the projectile wavelength according to the de Broglie relation - the smaller the wavelength, the higher the probability of the projectile '*to see*' the nucleons and interact with them [Kra88]. It should be noticed that another type of direct reaction exists, the central reactions. These reactions are only seen for higher energies[1] and they are characterized by the complete fragmentation of the target nucleus [Pau05].

1.2 Reaction probability

Considering a general case of incoming particles of type A incident on a target of type B with the reaction [Roh94]:

$$A + B \rightarrow FINAL\ STATE \tag{1.1}$$

The final state can be any possible outcome. The rate at which one given final state is produced is called transition rate. The probability for A + B to produce a certain final state or group of final states is specified by the interaction cross section, σ, which is defined to be [Roh94]:

$$\sigma = \frac{transition\ rate: A + B \rightarrow FINAL\ STATE}{\Phi} = \frac{R}{\Phi} \tag{1.2}$$

Here Φ is the incident flux of the particles of type A, defined by the number of projectiles of type A (ΔN) per covered area in target B (a) and per unit of time (Δt) and with R as transition rate [Roh94]:

$$\Phi = \frac{\Delta N}{a\Delta t} = \frac{R_i}{a} \tag{1.3}$$

[1] Compared with the energies available for this work.

With $\Delta N/\Delta t$ as R_i (rate of incident particles in the target).

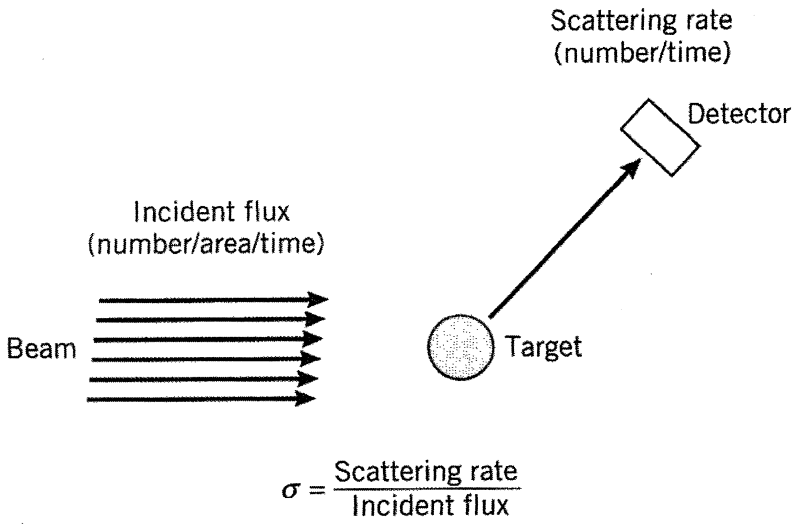

Figure 1.2: Definition of cross section in the particular case of scattering. However this example can be extrapolated to other cases. After [Roh94]

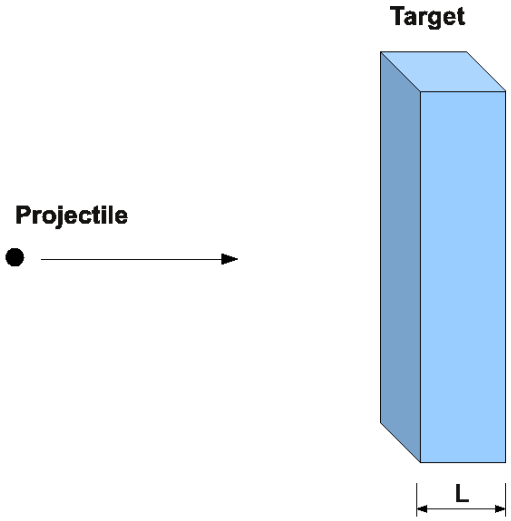

Figure 1.3: Scheme of a projectile fired towards a target of thickness L.

Now looking at the example depicted in figure 1.3, the number of nuclei per area of target ($N_{nucleus}/a$) is given by [Roh94]:

$$\frac{N_{nucleus}}{a} = \frac{N_A L \rho}{M} \tag{1.4}$$

Where N_A is Avogadro's number, ρ is the density, and M is the molar mass.

Since each incident particle has a chance to interact with the target nuclei along the thickness of the target, it is useful to calculate the cross section per target nucleus. Therefore, the

corresponding incident flux should be [Roh94]:

$$\Phi = \frac{R_i N_{nucleus}}{a} = \frac{R_i N_A L \rho}{M} \tag{1.5}$$

Given that the cross section is expressed by the transition rate divided by the incident flux, the cross section per target nucleus is [Roh94]:

$$\sigma = \frac{R}{\Phi} = \frac{R}{\left[\frac{R_i N_A L \rho}{M}\right]} = \frac{R}{R_i}\frac{M}{N_A L \rho} \tag{1.6}$$

Cross section has units of area. The unit of cross section, barn (b), is defined to be $10^{-28}\ m^2$.

In several situations it is useful to express cross section as a function of energy, $\sigma(E)$, sometimes called excitation function (figure 1.4). With this function it is possible to choose the most favorable energy for a given reaction [Alv08].

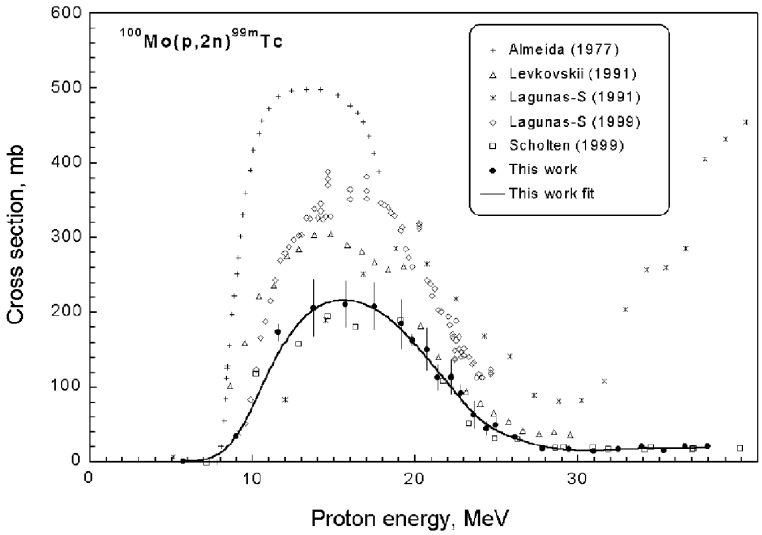

Figure 1.4: Plot of an excitation function. Adapted from [Tak03]

1.2.1 Thick target yields

Thick target yield is an important practical quantity to express the final state yield (about final state, refer to the section 1.2) for one such target. The expected thick target yield (Y) is given by [Alv08]:

$$Y = \frac{N_A H}{M z q_e} \int_{E_{in}}^{E_{out}} \left(\frac{dE}{dx}\right)^{-1} \sigma(E) dE \tag{1.7}$$

Where N_A is the Avogadro's number, M and H are the atomic mass and the isotopic abundance of the target, respectively, z is the atomic number of the projectile, and q_e is the electron charge. The remaining part of the expression contains the integration of the inverse stopping

power[1] times the excitation function between the energy of the incoming particle (E_{in}) and its energy upon crossing the target (E_{out}) [Alv08].

1.3 Neutrons

Neutron was observed for the first time by Bothe and Becker when they were bombarding a beryllium target with alpha particles. The emerging particles were first mistaken with highly energetic gammas but, soon after, Curie and Joliot realized that if those particles were gammas they should have at least 52 MeV, an unlikely scenario. It was Chadwick who proposed an explanation for those particles with the hypothesis of being neutral and, therefore, rather penetrating [Kra88].

1.3.1 Neutron-matter interactions

Since neutrons are neutral, the reactions that they can undergo are different from those induced by charged particles. An example of this is the fact that, being neutral, neutrons do not ionize directly [Kra88] and can enter the nucleus without feeling the Coulomb barrier. However, neutrons can ionize indirectly because they can produce high energetic particles capable of ionizing [Alp98]. According to Reuss, the *neutron-induced reactions* can be [Reu08]:

- *Scattering*: any reaction with at least one neutron in the final state
- *Absorption*: any reaction that terminates the neutron travel in a free state
- *Fission* (induced): the absorption leads to the fission of the compound-nucleus formed
- *Capture*: any other type of absorption

Scattering reactions can be divided in two main types: elastic and inelastic. In elastic scattering processes, a neutron collides with a nucleus, transfers some energy to it and, consequently, is deviated from its initial direction of motion. Conversely, in the process of inelastic scattering the incident neutron goes into the nucleus and a compound-nucleus is formed. Then, the neutron is re-emitted with lower kinetic energy and the nucleus is left in an excited state. The return to the ground state is accompanied by the emission of gamma rays [Pod06]. Neutron capture is similar to inelastic scattering but without the re-emission of the neutron, other particle being in general emitted [Alp98]. By convention, this reaction happens at low energies (*i. e.*, around thermal energy - section 1.3.2). When this reaction is seen at higher energies, it is called nonelastic scatter [Alp98].

When the goal is to reduce the neutron kinetic energy, low atomic mass materials should be used [Lev01] because of the higher probability (cross section) for elastic scattering. This process of slowing down the neutrons, called moderation, is ruled by equation 1.8, where $(\triangle E_k)_{max}$ is the maximum possible energy transfer to the target nucleus, m_n is the neutron mass, and M is the target nucleus mass [Pod06].

$$(\triangle E_k)_{max} = E_{k_i} \frac{4 m_n M}{(m_n + M)^2} \tag{1.8}$$

[1] See appendix A

With equation 1.8 it is easy to understand why low atomic mass materials are preferred: the lower the atomic mass, the higher can be the maximum energy transfer and, therefore, a more effective moderation can be achieved.

Besides of moderators one should mention reflectors, materials which, as the name implies, can reflect neutrons back to the desirable track. In these materials, neutrons should not lose much energy and so, reflector materials must have a high elastic scattering cross section and, according to the equation 1.8, a high atomic mass to minimize energy transfer [Lev01, Pod06]. Examples of these materials are Pb, Bi and PbF_2 [Lev01].

1.3.2 Neutron energy ranges

By convention, several designations are given to neutrons according to their energies. Unfortunately, there is no agreement within the scientific community pertaining to this convention, as can be seen in several publications such as [Kra88, Pod06, Reu08, And09, Lev01]. The exception for this is the energy of the so called thermal neutrons[1].

Given the lack of a clear definition of such terms, the designations used in this work are:

- *Cold neutrons*: energies bellow 0.025 eV
- *Thermal neutrons*: energies around 0.025 eV
- *Epithermal neutrons*: energies between 0.5 eV and 10 keV
- *Fast neutrons*: energies above 10 keV

1.3.3 Neutron sources

Neutrons do not have charge so they cannot be accelerated as charged particles are. The only solution to tune the energy of a neutron beam is to produce it through nuclear reactions and then moderate the beam if its energy is too high for the envisaged purpose [Kra88]. According to Krane, there are five main neutron sources, alpha-beryllium sources, photo-neutron sources, spontaneous fission, nuclear reactions, and reactor sources [Kra88]. They can be summarized as follow:

- *Alpha-beryllium sources*: they make use of the reaction $^4He + {}^9Be \rightarrow {}^{12}C + n$. The alpha-emitting material can be, for example, ^{226}Ra and with this solution it is possible to have a constant rate of neutron production [Kra88].
- *Photo-neutron sources*: its principle is similar to the alpha-beryllium sources, but use gammas instead of alphas and the reaction is $\gamma + {}^9Be \rightarrow {}^8Be + n$. Sodium-24 and antimony-124 can be used as gamma source [Kra88].
- *Spontaneous fission*: the source that is widely used with this kind of nuclear reaction is californium-252.

[1] The expression thermal neutrons comes from the fact that those neutrons have a characteristic room temperature (300 K) energy, 25.85 meV [And09]. This measure leads to the agreement about the thermal neutron energy.

- *Nuclear reactions*: nuclear reactions are those associated with the spallation process (section 1.1).
- *Reactor sources*: near the core of a nuclear fission reactor the neutron flux can be very high (typically 10^{14} neutrons/cm^2/s), therefore a neutron beam can be achieved with a small hole in the reactor's shield [Kra88].

Californium-252

There are about 100 radionuclides that decay by spontaneous fission with neutron emission [Kar97]. Despite this high number of neutron emitting radionuclides, californium-252 has been the choice for the vast majority of applications that require a small and/or portable neutron source. Reasons such as inadequate half-life (too short or too long), rareness, and production difficulties are the main motives to overlook the other radionuclides in favor of californium-252 [Kar97]. Californium-252 decays by alpha emission (96.91%) and spontaneous fission (3.09%), which gives a half-life of 2.645 years with a neutron emission of $2.314 \times 10^6\ s^{-1}\mu g^{-1}$ [Mar99]. The neutron energy spectrum was measure by Smith *et al.* and a function was proposed to model this emission (equation 1.9), where N represents the relative number of neutrons and E is the neutron energy in MeV [Smi57]. This equation was validated for the energy range between 0.2 MeV and 7.0 MeV [Smi57].

$$N(E) \approx e^{-0.88E} \sinh[(2.0E)^{\frac{1}{2}}] \tag{1.9}$$

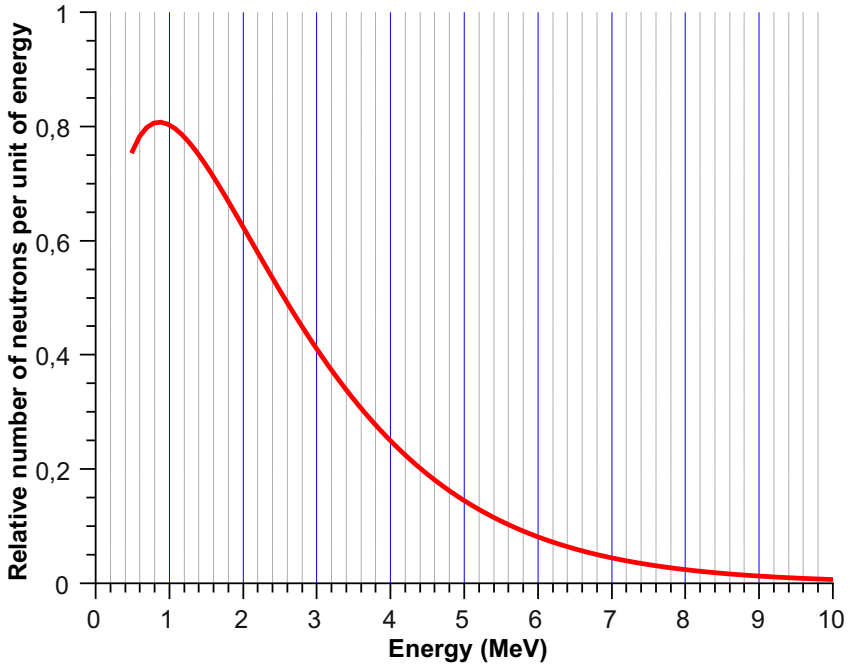

Figure 1.5: Graph of the equation 1.9 representing the approximated neutron energy spectrum of californium-252.

For this emission spectrum, the most probable energy and the average energy are about 0.7 MeV and 2.1 MeV, respectively [Mar99], and are released 3.756 ± 0.010 neutrons [Gol73] and 7.98 ± 0.40 gammas [Val99] per fission, making this source suitable for many applications.

For example, at the Californium User Facility for Neutron Science in Oak Ridge National Laboratory, californium-252 has been used for such different situations as land mine detection system, neutron damage testing solid-state detectors, irradiation of human cancer cells (BNCT experiments), and irradiation of rice to induce genetic mutations [Mar99].

1.4 ICNAS cyclotron

The cyclotron present at ICNAS is an IBA Cyclone® 18/9 HC capable of accelerating protons (18 MeV) and deuterons (9 MeV). The announced beam currents are 150 μA and 40 μA for protons and deuterons, respectively. Besides of this 'commercial' informations, through a contact with IBA Molecular some more details were obtained.

1.4.1 Energy

Cyclotron accelerates protons up to 18.5 MeV, but the particles lose about 1 MeV when they interact with the materials at the port of the cyclotron (figure 1.6). At ICNAS, the materials used on the beam port are [Alv10a]:

- *Havar®*[1]: to maintain the necessary low operating pressure inside the cyclotron
- *Gaseous helium*: to act as a cooling system
- *Aluminum or titanium*: to separate the gaseous helium from the exterior of cyclotron, support the sample and act as a thermal bridge between the helium and the sample

Therefore, it is possible to have an external proton beam with about 17.5 ± 0.2 MeV (uncertainty given by [Alv10b]). With deuterons, the loss in the port materials is about the same and since the accelerated beam reaches 9.2 MeV, it is possible to have an external deuteron beam of about 8.2 ± 0.1 MeV (after [Alv10b]).

1.4.2 Beam density and dispersion

Beam density for protons and deuterons is approximately Gaussian with 80% and 70% inside 10 *mm* at 30 cm after cyclotron port and the remain 20% and 30% within 3σ, respectively [Alv10b]. The beam profile was measured by Tamburella and Giles and its Gaussian shape was confirmed [Tam08].

The dispersion of the beam is mainly the result of its interaction with Havar® [Alv10b] and so in section 4.1 a simulation study of a pencil beam passing through a foil of this material is presented.

[1] See appendix B.

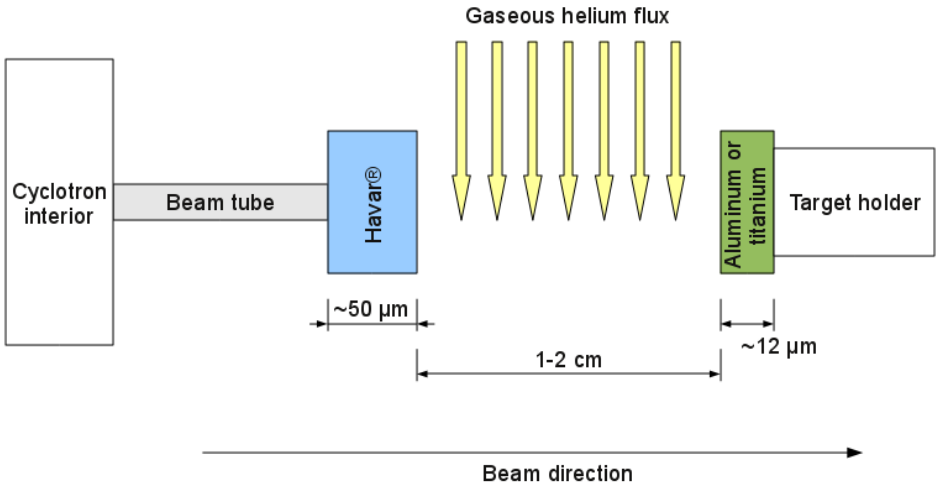

Figure 1.6: Scheme of a typical cyclotron's double-window system. The materials and their thicknesses depicted in the picture are specific for the IBA Cyclone® 18/9 HC present at ICNAS. After [Alv10a]

.

Chapter 2

Neutron Applications

The field of neutron applications is vast. This study aims at radiobiological studies, but many more uses can be found for neutrons: materials research, biomedical imaging, homeland security, and fundamental research in physics, among others.

2.1 Neutron capture therapy

2.1.1 Principles

Neutron capture therapy (NCT) was proposed by Locher in 1936 [Sal04, Lev01] after Goldhaber had discovered that boron-10 captures thermal neutrons and then disintegrates into an energetic alpha particle back to back with a recoiling lithium-7 ion [Lev01]. The lithium-7 nucleus and the alpha particle have a combined track length in soft tissues of about 14 μm [Ryy02], therefore within cell dimensions [Chu99], and both are high linear energy transfer (LET) particles causing sublethal and potentially lethal damage to DNA [Bar92]. In theory, boron neutron capture therapy (BNCT) provides a way to selectively destroy malignant cells and spare normal cells if a sufficient amount of boron-10 is delivered to the tumor beforehand [Bar05].

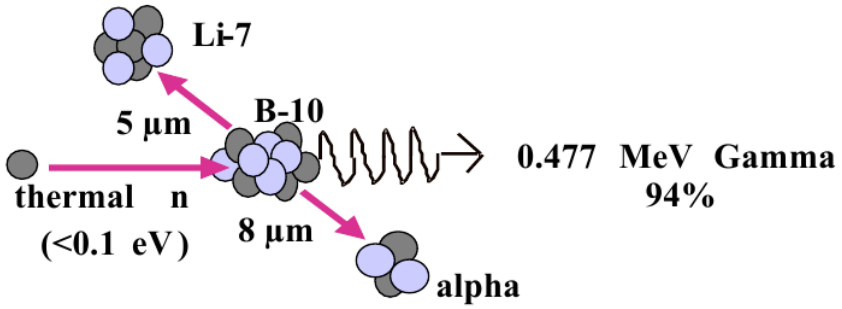

Figure 2.1: Nuclear reaction of boron-10 irradiated by thermal neutrons (with 94% probability). After [Lev01].

First tumors to be treated with BNCT were brain tumors, particularly glioblastoma multiforme (GBM) [Lev01], which is one of the most malignant and therapy resistant tumors known. GBM is usually fatal because of regrowth or resistance of the primary tumor. It is rare to

see metastases from GBM, although its growth pattern can lead to the involvement of regions of the brain at some distance from the primary tumor [Gup03]. Meanwhile, since the initial clinical trials, BNCT was also used to treat other types of brain tumors [Nak03], primaries or cerebral metastases of melanomas [Bar03, Bar05], head and neck tumors [Bar05], and liver tumors [Bar05]. For some cases the results seem to be equivalent to and, for others, the results surpass conventional radiotherapy (survival rate and survival time). There is some ambiguity among the published results which is due to the complexity of BNCT. BNCT is currently undergoing Phase I and Phase I/II clinical trials [Gup03].

2.1.2 Compounds for NCT

Boron has been the main element used in NCT since the initial proposal by Locher. Other nuclides also have high capture cross section for thermal neutrons, sometimes even higher than boron-10 (tables 2.1 and 2.2) [Sol97], but boron-10 has three great advantages:

1. High capture cross section for thermal neutrons (tables 2.1 and 2.2) with emission of high LET particles limited to a very short track length (equations 2.1 and 2.2) [Sol97, Lev01]
2. Boron compounds rival carbon in their extensive covalent chemistry and stability, allowing for the synthesis of many, very different chemical entities [Sol97]
3. Boron-10 is not a radioactive isotope and it is non-toxic [Sal04]

$$n + {}^{10}B \rightarrow {}^{11}B^{*} \rightarrow {}^{4}He\ (1.78\ MeV) + {}^{7}Li\ (1.01\ MeV)\ \ [4\%] \tag{2.1}$$

$$n + {}^{10}B \rightarrow {}^{11}B^{*} \rightarrow {}^{4}He\ (1.47\ MeV) + {}^{7}Li\ (0.84\ MeV) + \gamma\ (0.478\ MeV)\ \ [96\%] \tag{2.2}$$

Table 2.1: Thermal neutron capture cross sections (σ_{th}) for selected stable isotopes. Adapted from [Sal04].

Isotope	σ_{th} **(barn)**	**Neutron capture reaction**
^{3}H	5333	(n,p)
^{6}Li	941	(n,α)
^{10}B	3838	(n,α)
^{113}Cd	20600	(n, γ)
^{147}Sm	40140	(n, γ)
^{151}Eu	9200	(n, γ)
^{155}Gd	60900	(n, γ)
^{157}Gd	255000	(n, γ)
^{199}Hg	2150	(n, γ)

Besides the advantages of boron-10, gadolinium-157 has been studied as a NCT agent, alone or mixed with boron-10 [Cul04]. Gadolinium-155 and gadolinium-157 are isotopes of interest for NCT due to both their high capture cross section for thermal neutrons and the products of that capture reaction. Moreover, the latter isotope has the highest thermal neutron capture

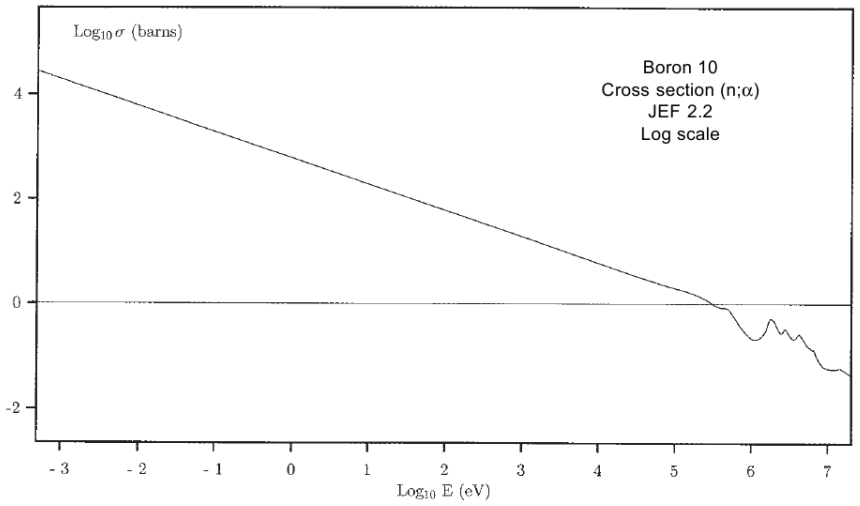

Figure 2.2: Cross section of the boron-10 (n,α) reaction. It is possible to visualize the general $\frac{1}{v}$ behaviour of the capture cross sections for neutrons at low energies, where v is the velocity of the neutron. After [Reu08].

Table 2.2: Thermal neutron capture cross sections (σ_{th}) of the elements commonly present in mammalian tissues. Adapted from [Sal04].

Isotope	σ_{th} **(barn)**	**Weight % in mammalian tissues**
^{1}H	0.333	10.0
^{12}C	0.0035	18.0
^{14}N	1.83	3.0
^{16}O	0.00019	65.0
^{23}Na	0.43	0.11
^{24}Mg	0.0053	0.04
^{31}P	0.18	1.16
^{32}S	0.53	0.20
^{35}Cl	32.68	0.16
^{39}K	2.1	0.20
^{40}Ca	0.4	2.01
^{56}Fe	2.57	0.01

cross section of all stable nuclides in the periodic table [Sal04]. The reaction ^{157}Gd(n,α)^{158}Gd generates prompt gamma emission up to 7.8 MeV [Sta01], with average energy around 2.2 MeV and a path length of several centimeters in live tissue [Sal04]. In this reaction other particles are produced, but the most biologically relevant are the five Auger electrons emitted in each neutron capture [Sta05, Sal04]. These low energy Auger electrons have a path length of only several nanometers in aqueous solutions (5-40 nm) [Sal04]. Despite the absolute low energy, the very short path length of these Auger electrons makes them high LET particles within a mean free path length of 12.5 nm [Sal04] that may induce double-strand damage in DNA [Sta01]. Since this ionizing radiation is limited to molecular dimensions, for significant DNA damage induction in tumor cells, it is essential to place the gadolinium atoms into the DNA helix or as near as possible, *i.e.*, within the nucleus [Sal04, Sta05]. Furthermore, gadolinium has two other reasons to be a potentially good neutron capture therapy agent:

1. Several gadolinium compounds are known to target brain gliomas, because of brain blood barrier disruption in these tumors (they are in fact used as tumor contrast-enhancing agents for magnetic resonance imaging (MRI)) [Sta01]
2. The search of gadolinium compounds to be used with MRI allowed for a wealth of information about pharmacokinetics, biodistribution, and tolerance of those compounds to be assembled [Sta01]
3. Gadolinium compounds should allow MRI monitoring of the treatment [Sal04]

Boronated compounds

These compounds were the first to be applied to NCT and they are being developed for about 50 years now [Bar05]. The most important requirements for a successful boron delivery agent are [Bar05]:

- Low systemic toxicity and normal tissue uptake with high tumor uptake and tumor/blood concentration ratio higher than 3-4:1
- Tumor concentrations of boron-10 around 20 μg per gram of tumor
- Rapid clearance from blood and normal tissues and persistence in tumor during treatment

However, until 2005 no single boron delivery agent achieved these criteria [Bar05] and until 2009 the progress made was almost none [Bar09]. In the first BNCT clinical trials, boric acid and some of its derivatives were used, but those simple chemical compounds were non-selective and had poor tumor retention [Bar05]. In the 1960s, two other boron compounds emerged, BPA[1] (compound 1 in figure 2.7) and BSH[2] (compound 2 in figure 2.7) [Bar05, Bar09]. These compounds had low toxicity, persisted longer in animal tumors compared with related molecules, and had tumor/brain and tumor/blood boron ratios greater than 1 [Bar05, Sal04]. Boron-10-enriched BSH and BPA, complexed with fructose to improve its water solubility, have been used clinically in Japan, the United States, Europe, and Argentina. Although these drugs are not ideal, their safety following intravenous administration has been established [Bar05], and pharmacokinetics models can predict tumor, blood, and normal tissue boron-10 concentrations (figure 2.4) [Kig03, Kor04, Ryy02]. The new generation of BNCT delivery agents mainly consists of a stable boron group attached via a hydrolytically stable linkage to a tumor-targeting functional group, such as low molecular weight biomolecules or monoclonal antibodies [Bar05].

Table 2.3: Comparison between features of BSH and BPA important to BNCT. After [Chu99].

Compound	Concentrations of boron-10 in tumor (ppm)	Tumor/normal tissue ratio	Tumor/blood ratio
BSH	3-20	>10	~1
BPA	15-45 and higher	2-4	3-5

One of the main concerns about BNCT is how to measure boron-10 concentrations in real-time during treatment. The gammas emitted in 94% of the neutron captures are one option.

[1] (L)-4-dihydroxy-borylphenylalanine
[2] Sodium mercaptoundecahydro-closo-dodecaborate

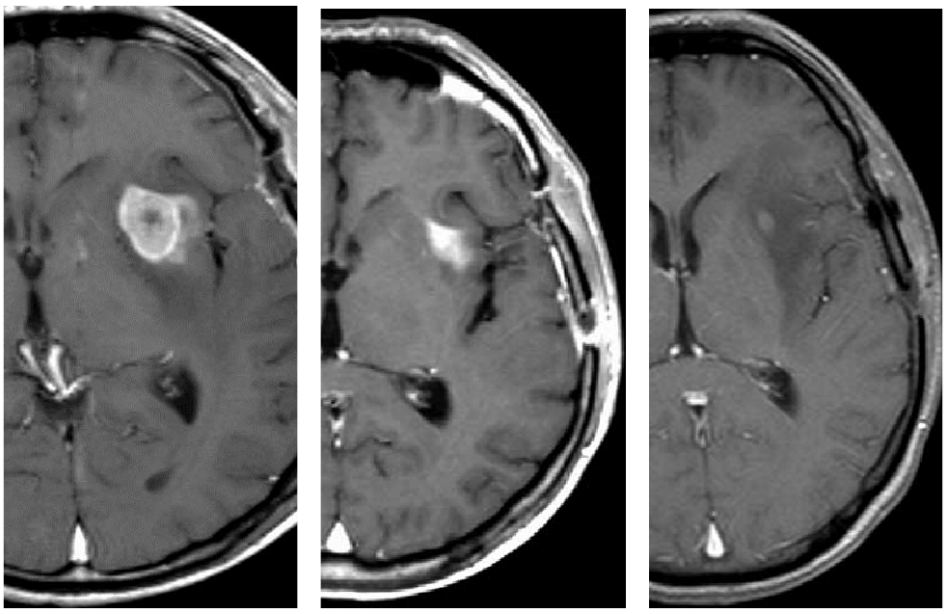

Figure 2.3: An example of a BNCT treatment outcome in a 39-year-old man with histologically confirmed glioblastoma multiforme. Left panel: A MRI scan taken 10 days after brain surgery showing an enhancing tumor. Middle panel: A MRI taken one month following BPA-based BNCT suggesting tumor response. Right panel: A MRI three months following BNCT. After [Joe03].

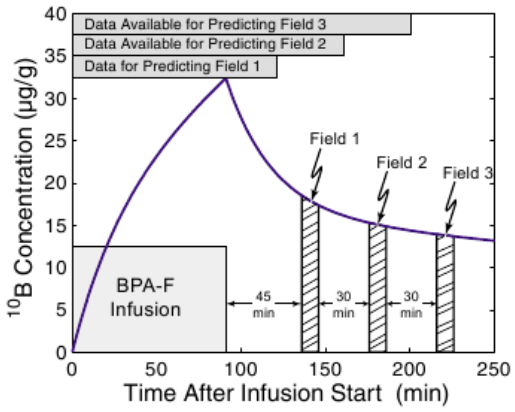

Figure 2.4: BPA-fructose concentration model was achieved considering the dose and duration as actually administered to each patient. Three simulated irradiation fields are delivered, with the first starting 45 minutes after the end of infusion and with 30 minutes between fields. Only blood samples taken up until 15 minutes before the start of each irradiation were used to determine the model prediction of boron-10 concentration for each field, as indicated by the three horizontal bars at the top. After [Kig03].

The work of Burlon *et al.* demonstrated that this is feasible with prompt gamma-ray analysis (figures 2.5 and 2.6) [Bur05].

On the other side, measurements of the concentration of boron-10 *in vitro* and *ex vivo* can be made with the same prompt gamma-ray analysis [Kig03], and with ICP-AES[1] [Kor04, Kig03]. Studies *in vivo* can be done using a form of fluorine-18-labeled-BPA and a positron emission

[1] Inductively coupled plasma atomic emission spectroscopy

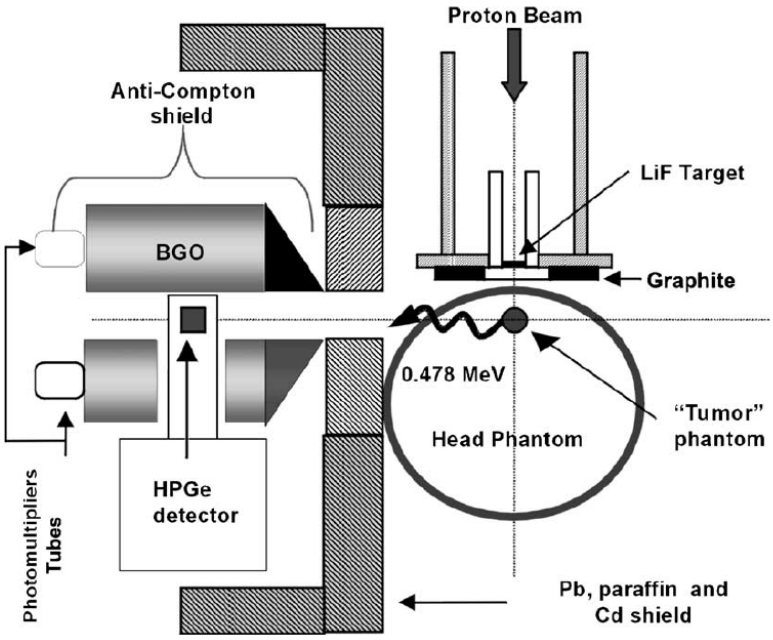

Figure 2.5: Scheme of a gamma-detection system with an anti-Compton shield. After [Bur05].

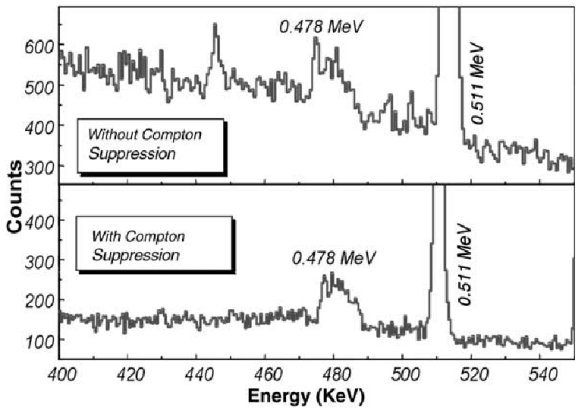

Figure 2.6: High-Purity Germanium gamma spectra with and without anti-Compton suppression obtained with the setup of figure 2.5. After [Bur05].

tomography (PET) scan (figure 2.8) [Kig03, Kab97, Ima98].

Gadolinium compounds

Until 2001 gadolinium neutron capture (GdNCT) did not undergo clinical trials [Sta01], however, several studies have been made to test the benefits of this approach [Sta01, Sta05, Sal04, Cul04]. Due to its availability and tumor-seeking properties [Sta01], standard gadolinium contrast agents for MRI have been explored to be used as GdNCT compounds as well [Sta01, Sta05, Sal04]. Examples of these agents are Gd-DTPA[1] and Gd-DOTA[2] [Sal04, Sta05]. Two

[1] Gadolinium-diethylene triamine pentaacetic acid
[2] Gadolinium-tetraazacyclododecane tetraacetic acid

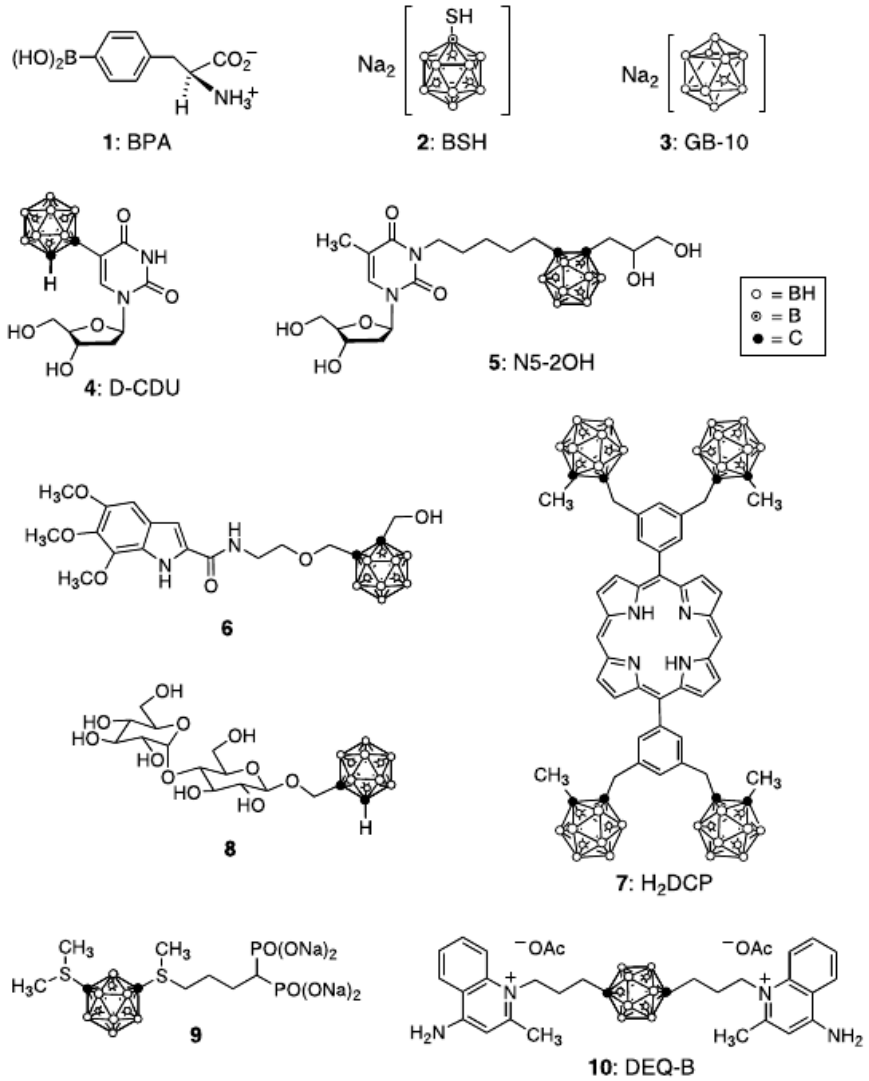

Figure 2.7: BPA, BSH and some low molecular weight BNCT agents under investigation. BPA (compound 1) and BSH (compound 2) are currently in clinical use. GB-10 (compound 3) has shown promising results in animal models, as have the nucleoside derivatives β-5-o-carboranyl-2´-deoxyuridine (D-CDU; compound 4) and N5-2OH (compound 5). Compound 6, a trimethoxyindole derivative, has shown promise *in vitro* and compound 7, H_2DCP, a porphyrin derivative, was shown to be tumor selective. The maltose derivative, compound 8, has shown low cytotoxicity and tumor cell uptake *in vitro*, the biphosphonate, compound 9, has tumor-targeting ability, and the dequalinium derivative dequalinium-B (DEQ-B; compound 10) has shown promise in *in vitro* studies. After [Bar05].

other compounds have been developed, Gd-Tex[1] as a radiosensitizer, and HDG as a DNA-targeting contrast agent [Sal04]. Good results were already obtained for HDG for *in vitro* and *in vivo* experiments (table 2.4) [Sal04].

Although the two main BNCT drugs, BPA and BSH, have different delivery mechanisms, they share a common limitation: because the products of the (n,α) reaction of boron-10 have low path lengths, it is necessary to have boronated compounds inside every tumor cell, so an

[1] Motexafin gadolinium

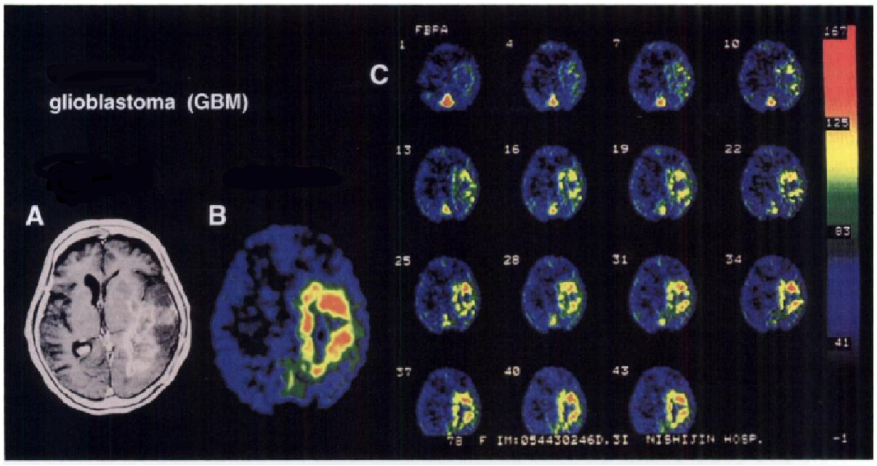

Figure 2.8: Typical PET images of fluorine-18-labeled-BPA in patients with GBM. (A) MRI image with gadolinium enhancement; (B) PET images corresponding to the MRI; (C) Dynamic PET study. Adapted from [Ima98].

Table 2.4: Gadolinium nucleus uptake criteria (Q_{Gd}) determined for four GdNCT agents on TB10 GBM cell cultures. Adapted from [Sal04].

Contrast agent/radiation sensitizer	Q_{Gd}	**GBM cell nucleus uptake (% cells)**
Gd-DTPA	0.2	2.5
Gd-DOTA	14	14
Gd-Tex	2.5	92
HDG	20	100

Note: $Q_{Gd} = \frac{Gd_{intracelullar}}{Gd_{extracelullar}}$ after 74h exposure.

uniform intercellular drug uptake is needed [Cul04]. Thus, despite the limitations of these compounds, such uptake is also related to tumor vascularization and cell metabolism [Cul04]. This issue is relevant when there are quiescent tumor cells (less active or even dormant tumor cells) that some studies found to have extremely limited uptake of BPA [Cul04]. This is related to the very low metabolic rate of those cells and, although BSH is less dependent on this factor, there are no studies that can confirm the uptake of BSH in all quiescent cells [Cul04]. Since almost all products of the (n,γ) reaction of gadolinium-157 have longer ranges than those of the boron-10 reaction, GdNCT can kill tumor cells without stringent requirements on uptake uniformity [Cul04]. Another significant advantage of gadolinium compounds over boronated ones is the fact that the latter are retained in the lysosomes which are randomly distributed throughout the cytoplasm and around the cell nucleus [Sta01]. No selective concentration into the cell nucleus has yet been demonstrated for boronated compounds whereas the study of Stasio *et al.* has demonstrated that gadolinium preferentially concentrates in the cell nucleus [Sta01].

Some studies have shown that GdNCT has more limitations than BNCT, mainly due to the longer interaction lengths of the low-LET neutron capture products of gadolinium [Cul04]. GdNCT is less localized and, consequently, results in lower increase of tumor dose over the healthy tissue dose and in a decreased therapeutic ratio [Cul04]. However, gadolinium compounds can be combined with boronated compounds and some possible advantages can come from this combined approach [Sal04, Tak05].

Apart from MRI, there are some techniques to study the location of gadolinium *in vitro* and/or *in vivo*. Due to the impossibility of detecting Gd-DOTA and Gd-DTPA by the conventional approach (fluorescence microscopy and autoradiography), Stasio *et al.* used synchrotron spectromicroscopy, ICP-MS[1], ToF-SIMS[2], and MEPHISTO[3] spectromicroscopy [Sta05]. In the study of Takahashi *et al.*, they used prompt gamma-ray analysis and α-autoradiography to assess the biodistribution *ex vivo* of a mixture compound of BPA and Gd-DTPA [Tak05]. It is also possible that real-time monitoring during treatment can be achieved with prompt gamma-ray analysis knowing the gamma-ray spectrum (figure 2.9) and with a system similar to the one shown in figure 2.5.

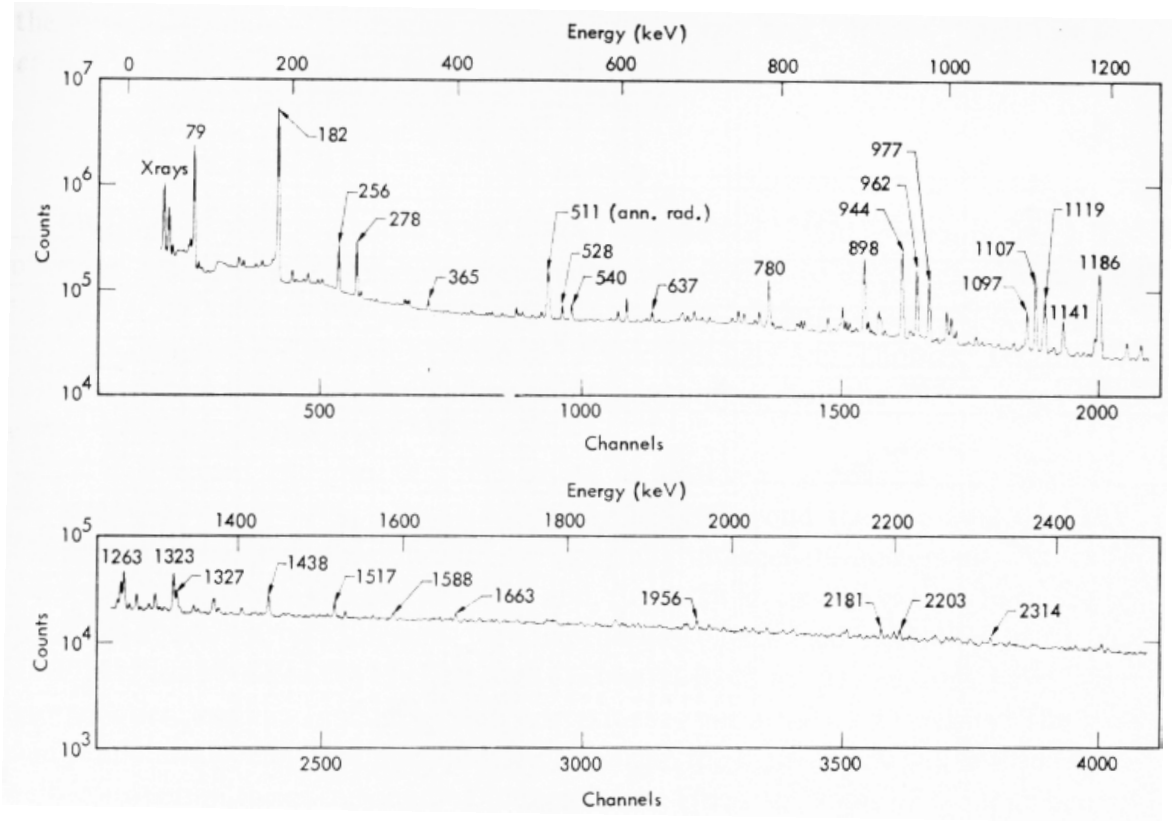

Figure 2.9: Gamma-ray spectrum of ^{158}Gd. After [Whi73].

2.1.3 Neutron beamline requirements

For NCT, an adequate thermal neutron field has to be created in the boron-labeled tumor cells within a prescribed target volume [Lev01]. This means that for target volumes well below surface, epithermal beams will generally be best, while for target volumes near the surface, thermal beams will suffice (figure 2.10) [Lev01].

Current experience with BPA and BSH shows that a desirable minimum beam intensity would be 10^9 epithermal neutrons cm^{-2} s^{-1}. Beams of 5×10^8 n cm^{-2} s^{-1} are usable, but result in

[1] Inductively coupled plasma mass spectrometry
[2] Time-of-flight secondary ion mass spectrometry
[3] From the French, microscope à émission de photoélectrons par illumination synchrotronique de type onduleur (photoelectron emission microscope by synchrotron undulator illumination)

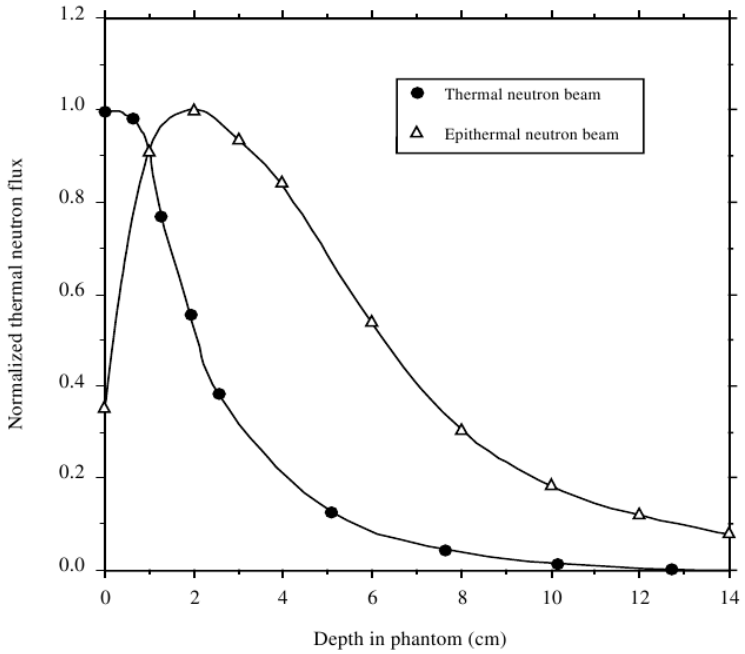

Figure 2.10: Comparison of flux-depth distributions for thermal and epithermal neutrons. After [Lev01].

rather long irradiation times [Lev01]. When higher intensity beams are available the advantages of shorter irradiation times must be weighted against those of improved beam quality[1]. Where there is a choice to be made, most practitioners would rather have better quality rather than more intensity, within the constraint of having a reasonable treatment time (possibly extending up to one hour) [Lev01, Bar05]. It should be noticed that if the currently used values of boron concentration can be raised, beam intensity requirement (or treatment time) will be reduced proportionately and the values presented do not take fractionation into account [Lev01]. Beam quality is determined by three main parameters and they are discussed below by order of importance.

1. **Fast neutron component**: fast neutrons, which invariably accompany the incident beam, have a number of undesirable characteristics such as the production of high LET protons with a resulting energy dependence on their induced biological effects. Therefore, it is one of the main objectives of BNCT beam design to reduce the fast neutron component of the incident beam as much as possible [Lev01].

2. **Gamma ray component**: because of the energy range of the gamma radiation, it results in a non-selective dose to both tumor tissue and a large volume of healthy tissue. Hence, it is desirable to remove as much gamma radiation from the beam as possible. Since there are also (n,γ) reactions occurring inside the patient, the importance of this component in the incident beam is somewhat reduced [Lev01].

3. **Ratio between thermal flux[2] and epithermal flux**: to reduce damage to the scalp,

[1] With higher intensity beams it is possible to choose moderators for achieving better beam quality (*i.e.* better energy distribution) without concerns about loosing beam intensity. In contrast, with lower intensity beams the main concern is to reach neutron epithermal energies without significant reduction of beam intensity, sometimes overlooking beam quality

[2] The neutron flux is defined by the number of neutrons per unit of area per unit of time (neutrons cm^{-2} s^{-1})

thermal neutrons in the incident beam should be minimized. A target number for the ratio of thermal to epithermal flux should be 0.05 [Lev01].

The beam size is not defined and can change as needed. Circular apertures of 12 to 14 cm diameter are being used in the present clinical trials. However, sizes of up to 17 cm have been proposed for irradiation of brain tumors. Other cancers in the body might require even larger apertures. These maximum sized apertures are reduced in accordance with the tumor size and position as determined by the treatment planning requirements [Lev01].

Since an epithermal neutron beam is needed, one should use moderators to reduce neutrons kinetic energy [Lev01, Bar05, Chu99, Gup03]. Any moderator materials chosen must not decompose in a high radiation field, nor produce moisture. Any neutron activation products from the materials should be short lived. Suitable candidates are Al, C, S, Al_2O_3, AlF_3, D_2O, and $(CF_2)_n$. Combinations of Al followed by Al_2O_3 or AlF_3 downstream are very efficient because O and F cross sections fill in the valleys between the energy resonance peaks of Al [Lev01, Mau98, Lud97]. Furthermore, a mixture of 60% Al and 40% AlF_3 was proposed [Lud97]. Fluental™ [1] was developed by the technical Research Centre of Finland and stands up well to radiation, but is very expensive. Teflon™ is susceptible to radiation damage, but even so, may be acceptable when exposed to the relatively modest neutron fluences projected for the facility over its anticipated lifetime [Lev01].

2.1.4 Radiobiological considerations

Dose calculations

Given an incident radiation beam similar to those applied in BNCT, there are four dose components when the beam enters the tissue (figure 2.11) [Lev01, Chu99]:

- *The gamma dose*: the dose due to gamma rays accompanying the neutron beam as well as gamma rays induced in the tissue itself. In the latter case, hydrogen in tissue absorbs thermal neutrons in ^{1}H(n,*gamma*)^{2}H reactions and emits 2.2 MeV gamma rays (table 2.2), to which tissue is quite transparent.
- *The neutron dose or proton-recoil dose*: epithermal and fast neutrons cause 'knock-on' recoil protons from hydrogen in tissue in ^{1}H(n,n')^{1}H reactions resulting in locally deposited energy from recoiling protons.
- *The nitrogen dose*: nitrogen-14 in tissue absorbs a thermal neutron and emits a proton in a ^{14}N(n,p)^{14}C reaction (table 2.2). Dose results from locally deposited energy from the energetic proton and the recoiling ^{14}C nucleus.
- *The boron dose*: boron-10 absorbs a thermal neutron in a ^{10}B(n,α)^{7}Li reaction. The energetic alpha particle emitted and the recoiling lithium-7 ion result in locally deposited energy averaging about 2.33 MeV. In about 94% of events the recoiling lithium-7 ion is produced in an excited state and de-excites in flight, emitting a 477 keV gamma ray. In the remaining events, lithium-7 is emitted in the ground state with no gamma ray emission. Because the emitted gamma rays from boron-10 neutron capture are about two orders of magnitude less prevalent and about one-quarter the energy of the 2.2 MeV

[1] Fluental™ is a patented material with AlF_3 (69%-weight), aluminum (30%-weight) and LiF (1%-weight) [Lev01]

gamma rays from hydrogen capture, they can be ignored from a dosimetric perspective, although they are frequently utilized for boron-10 analysis purposes (figures 2.5 and 2.6).

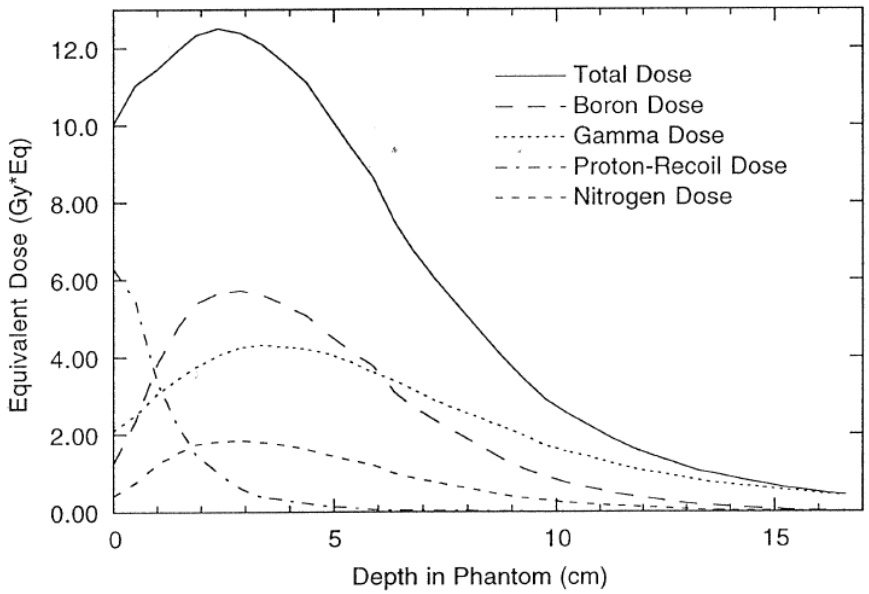

Figure 2.11: Normal tissue depth-dose curves in a phantom for epithermal neutrons. After [Chu99].

Neutrons not captured by boron-10 nuclei produce unwanted background radiation through a number of reactions with nuclei in normal tissue, such as nitrogen, hydrogen, carbon, and chlorine [Lev01, Chu99]. Additionally, there are contaminations in the neutron beam, such as gamma rays or fast neutron components not filtered out from the beam. These background radiations contribute equally to the dose in normal tissue and tumor volumes independent of boron-10 concentration [Chu99]. However, a higher concentration of boron-10 in the tumor will result in it receiving a higher total dose than that of adjacent normal tissues [Bar05, Chu99, Lev01, Bar92]. This is the basis for the therapeutic gain in BNCT [Bar05].

Therapy planning of BNCT using epithermal neutron beams requires calculation of the biological dose distributions in tumor and normal tissues. In this calculation, one must take into consideration the fact that different kinds of radiation contributing to the total dose have different values of relative biological effectiveness[1] (RBE). Furthermore, the biological boron dose due to neutron capture by the boron-10 nuclei depends on the compound factor[2] (CF) [Chu99]. This CF is related to the mode and route of drug administration, boron distribution within the tumor, normal tissues, and even more specifically within cells, and even the size of the nucleus within the target cell population all can influence the experimental determination of the CF factor [Bar05]. CF, therefore, are fundamentally different from the classically defined RBE, which is primarily dependent on the quality (*i.e.*, LET) of the radiation administered [Bar05]. CF is strongly influenced by the distribution of the specific boron delivery agent and can differ substantially, although they all describe the combined effects of alpha particles and lithium-7 ions. The CF for the boron component of the dose are specific for both the boron-10 delivery

[1] Relative biological effectiveness is the ratio of the absorbed dose of a reference source of radiation (*e.g.* X-rays) to that of the test radiation that produces the same biological effect [Bar05].

[2] Some authors denominate this factor as compound biological effectiveness (CBE) factor.

agent and the tissue [Bar05, Lev01, Chu99]. The compound factor and RBE make it possible to add the different dose components and calculate the total dose, D_{total}, in a photon-equivalent dose expressed in gray-equivalent (Gy-Eq) units [Chu99, Bar05]:

$$\begin{aligned} D_{total} &= CF \times D_{boron-10} \\ &+ RBE_{nitrogen} \times D_{nitrogen} \\ &+ RBE_{fast\ neutron} \times D_{fast\ neutron} \\ &+ RBE_{\gamma} \times D_{\gamma} \end{aligned} \tag{2.3}$$

Where each RBE_i is the specific RBE for the radiation type i and D_i is the absorbed dose of radiation i.

Fractionation

The basis of fractionation in radiotherapy can be understood in simple terms. Dividing a dose into a number of fractions spares normal tissues because of repair of sublethal damage between dose fractions and repopulation of cells if the interval time is sufficiently long. At the same time, dividing a dose into a number of fractions increases damage to the tumor because of reoxygenation and reassortment of cells into radiosensitive phases of the cycle between dose fractions[1]. The advantages of prolongation of treatment are to spare early reactions and to allow adequate reoxygenation in tumors. Excessive prolongation, however, allows surviving tumor cells to proliferate during treatment [Hal00]. As a summary of the basis of fractionation, here comes the four R's of radiobiology [Hal00]:

- Repair of sublethal damage
- Reassortment of cells within the cell cycle
- Repopulation
- Reoxygenation

The alpha particles produced in the ^{10}B(n, α)^{7}Li reaction have an average LET of 200 keV/μm and at most, it takes only a few of them discharging their energy within a malignant cell to kill it. They are equally as lethal to hypoxic cells, oxygenated cells, and nondividing cells [Bar92]. Sublethal damage (SLD) and potentially lethal damage[2] (PLD) induced by BNCT are not subject to repair, whereas SLD and PLD produced by gamma photons and X-rays are repairable. These properties are advantageous for the treatment of glioblastomas and melanomas in which significant DNA repair may occur [Bar92].

Fractionation hardly moderates (if at all) the effects of high LET radiation. In BNCT, the issue is much more complicated because of the mix of high and low LET radiation encountered [Gup03]. A further concern is the adequate delivery of boron-10 to all parts of the tumor.

[1] The reassortment is the redistribution of cells throughout the phases of the cell cycle and this is relevant because the radiosensitivity of mammalian cells varies throughout the cell cycle [Nia98]

[2] According to IAEA, radiation damage to mammalian cells can be divided into three categories: (1) lethal damage, which is irreversible, irreparable and leads to cell death, (2) sublethal damage, which can be repaired in hours unless additional sublethal damage is added that eventually leads to lethal damage, and (3) potentially lethal damage, which can be manipulated by repair when cells are allowed to remain in a non-dividing state [Sun05]

Since, in principle BNCT, delivers high LET radiation to tumor cells, fractionation affects normal tissues and tumor differently [Gup03]. The existence of low LET components in BNCT may allow the delivery of higher doses, or add an additional factor of safety, to normal tissues during a fractionated dose delivery. In the tumor, the most important gain from fractionation is thought to be due to retargeting of the boron compound [Gup03].

Although, in theory, no advantages emerge from a fractionated protocol, several studies demonstrate that this is not clear yet [Bar92, Gup94, Mor01, Gah89]. Moreover, the effect of different treatment variables on the treatment time and tumor dose has been shown to be very significant. It has also been shown that the location of the maximum dose shifts significantly, depending on some of the treatment variables, mainly the fractionation scheme used. These results further emphasize the fact that dose prescription in BNCT is very complicated and nonintuitive [Gup94]. Above all, the example depicted in figure 2.12 demonstrates the great potential of BNCT and the hypothesis of considering and studying a fractionated protocol for it.

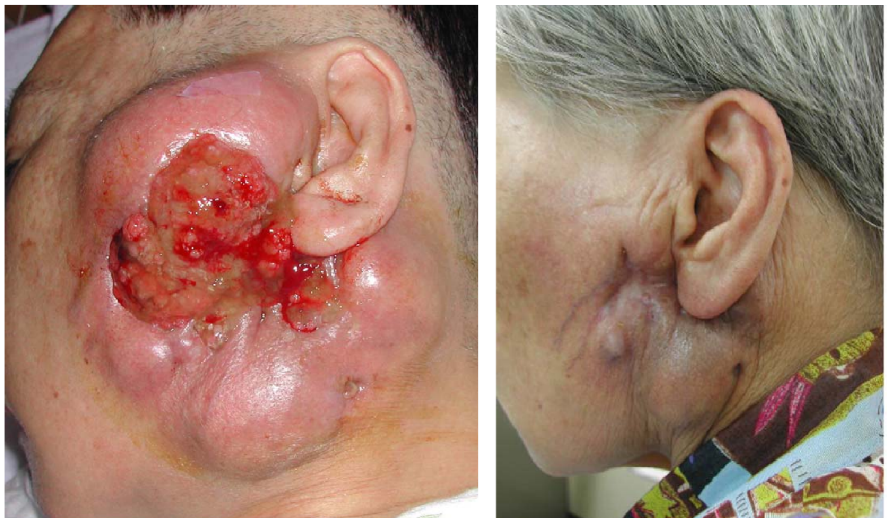

Figure 2.12: Clinical appearance of a case in a clinical trial (mucoepidermoid carcinoma of parotid gland). Before BNCT (left) and 22 months after the first BNCT treatment. Although it can not be considered as a standard fractionation scheme, three BNCT treatments were used in this case (the second treatment was one month after the first; the third was one year after the first). After [Kat04].

2.1.5 Challenges

The success of BNCT depends on a number of parameters including tumor location and depth, boron-10 content in tumor and normal tissues (more selective and effective boron-10 delivery agents [Bar05]), and neutron fluence. Calculations have shown that 10^9 boron-10 atoms per cell and thermal neutron fluences of 10^{12}-10^{13} n cm^{-2} are needed [Bar92]. This high number of boron-10 atoms is required for the radiation dose from the alpha particles to exceed that delivered by the unavoidable background contributions of the capture reactions of hydrogen and nitrogen [Bar92]. Theoretically, it should be possible with BNCT to increase significantly and selectively the radiation dose delivered to tumors to levels higher than those achieved with conventional therapy while simultaneously restricting the normal tissue doses to levels lower than their tolerance [Bar92]. This will depend on the energy of the neutrons, dose rate, and

fractionation [Bar92].

Also, the development of methods to provide semiquantitative estimates of tumor boron content before treatment, improvements in clinical implementation of BNCT, and a need for randomized clinical trials with an unequivocal demonstration of therapeutic efficacy are other critical issues that must be addressed [Bar05]. If these issues could be adequately addressed, then BNCT could move forward as a treatment modality [Bar05].

Another challenge for BNCT is the ambiguity of published data as it was mentioned in section 2.1.1. The BNCT community needs to, and is already in the process of, standardize each aspect of the design and implementation of clinical trials. If this goal is achieved, it will allow meaningful use of the available multi-institutional data. Only after some of these challenges are met and all the data is sorted out, will it be possible to move ahead into Phase III clinical trials [Gup03].

BNCT represents an extraordinary joining together of nuclear technology, chemistry, biology, and medicine to treat cancer. Sadly, the lack of progress in developing more effective treatments for high-grade gliomas has been part of the driving force that continues to propel research in this field [Bar05]. BNCT may be best suited as an adjunctive treatment, used in combination with other modalities, including surgery, chemotherapy, and external beam radiation therapy, which, when used together, may result in an improvement in patient survival. Clinical studies have shown the safety of BNCT. The challenge clinicians and researchers are facing is how to get beyond the current impasse [Bar05].

2.2 Neutron imaging

2.2.1 Principles

Neutron radiography is a powerful nondestructive imaging technique that produces a two-dimensional attenuation map of neutrons that have penetrated an object being examined [And09]. The method was initially developed after X-ray radiography, and the techniques share many similarities in setup and practice. X-ray and neutron radiography are often complementary techniques, especially when low-energy neutrons are used. X-rays interact with orbital electrons and are strongly tied to the physical density of the examined object [And09, Par08]. Neutrons interact with the nucleus rather than its orbital electrons, so there is usually no tie to the object's electron density, but rather its elemental composition. Because the technique is based on attenuation from a well-collimated beam, either scattering or absorption will result in intensity variations to create an image [And09, Par08].

As it happens with X-ray, neutron imaging can also be thought to be three-dimensional (neutron tomography).

2.2.2 Comparison with other imaging modalities

In section 2.2.1 some comparisons were already made between neutron and X-ray imaging. Those two methods rely on different matter interactions (figure 2.13), therefore the information that can be gathered from each imaging technique is distinct. To make this clear, some example images are shown.

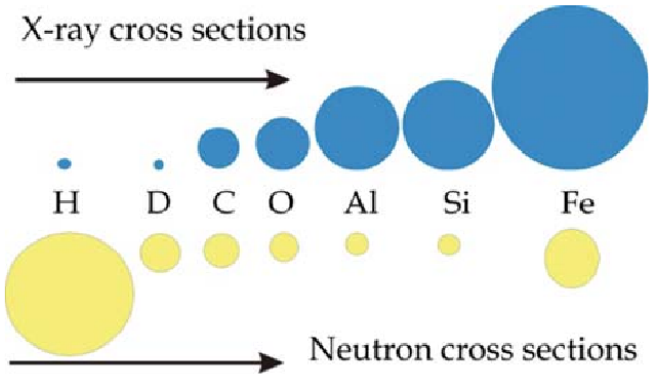

Figure 2.13: X-ray and neutron cross sections for different elements. The sizes of the circles symbolize the strengths of the scattering cross sections. After [And09].

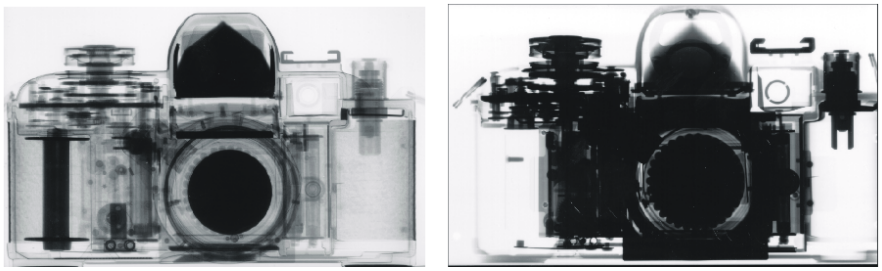

Figure 2.14: Comparison of neutron (left) and X-ray (right) images. After [Ins].

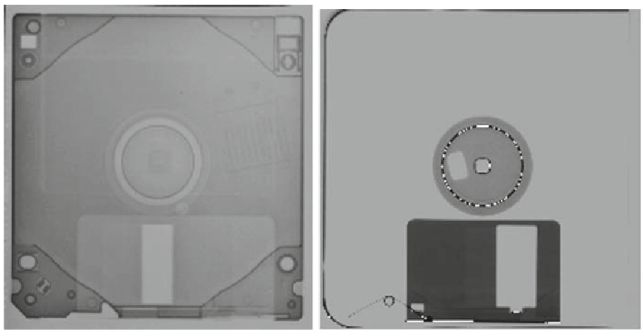

Figure 2.15: Radiograph of a computer floppy disk using neutrons (left) and X-rays (right). With neutrons it is possible to see the polymeric components clearly, while X-rays are sensitive only to the metallic components. After [And09].

2.2.3 Neutron beamline requirements

A neutron radiography system consists of a neutron source, a moderator to thermalize the neutrons, an aperture and a collimator to organize neutrons into a beam, and a detector to visualize the image (figure 2.17) [And09].

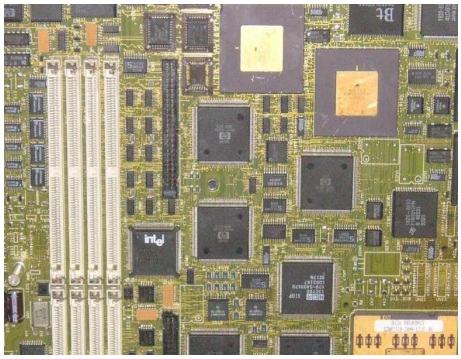

(a) Photograph of a printed circuit board.

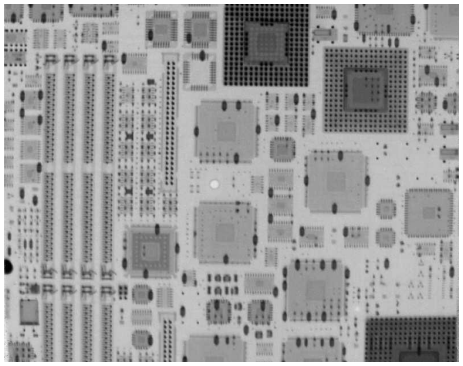

(b) X-ray image. Most contrast is given by the metal pins.

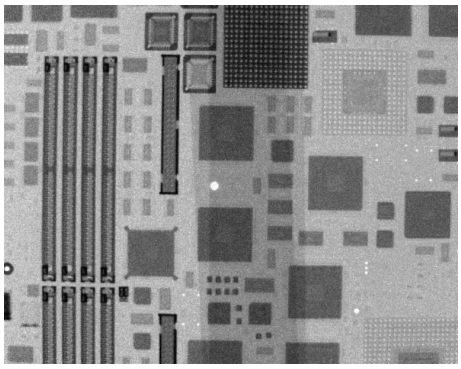

(c) Neutron image. Most contrast is given by plastic parts and the metal pins are nearly transparent.

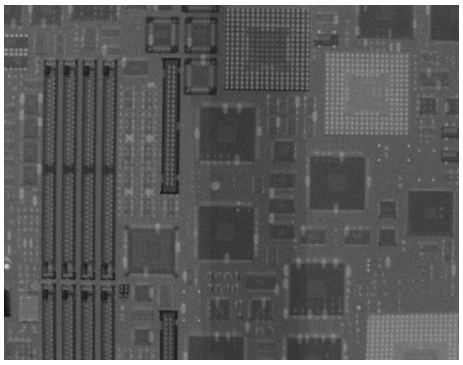

(d) Combination of both images. The X-ray image was subtracted from the neutron image.

Figure 2.16: Comparison and combination of X-ray and neutron images. After [Sch]

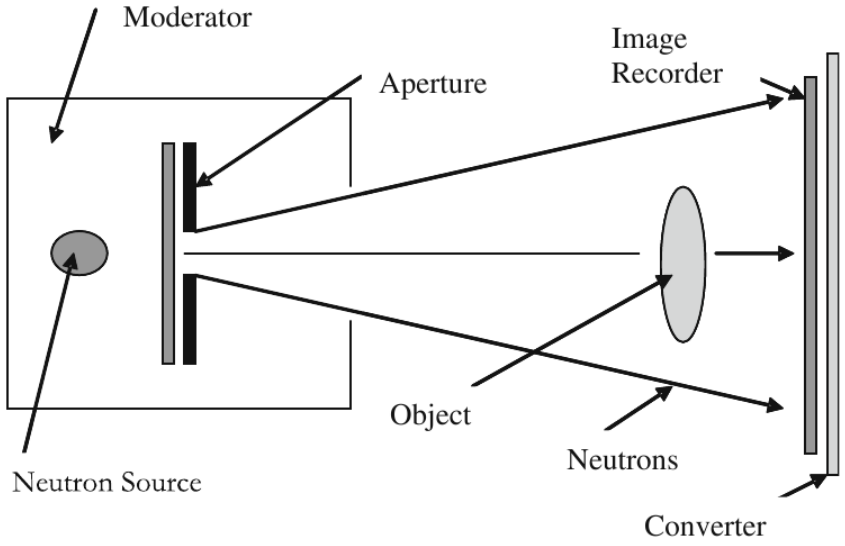

Figure 2.17: Illustration of a typical neutron imaging system. After [And09].

Energy

Neutron imaging requires neutron energies in the thermal/epithermal energy range (0.025 eV - 10 keV) [And09]. Thus some form of moderation is needed to slow down neutrons to this

energy [And09]. Since the principle is the same, the materials depicted in section 2.1.3 are also applicable in this case.

Collimation

Once low-energy neutrons are produced, they must be formed into a usable beam. Neutrons are emitted and then scattered randomly in the moderator and, because of their neutral charge, they cannot be focused like electrons [And09]. Those neutrons traveling in the desired solid angle can, however, be selected by the introduction of a tube into or adjacent to the moderator. This has the effect of allowing neutrons to stream down the tube axis toward the object being radiographed [And09]. The walls of the collimator tube are lined with a neutron opaque material having a high absorption cross section (such as boron, gadolinium, and cadmium), which prevents background neutrons from entering and also reduces low-angle scattering within the collimator [And09]. The most common collimator design is a divergent collimator (figure 2.18) with a small entrance aperture and a larger exit. This maximizes the neutron flux and permits a larger field at the imaging plane [And09].

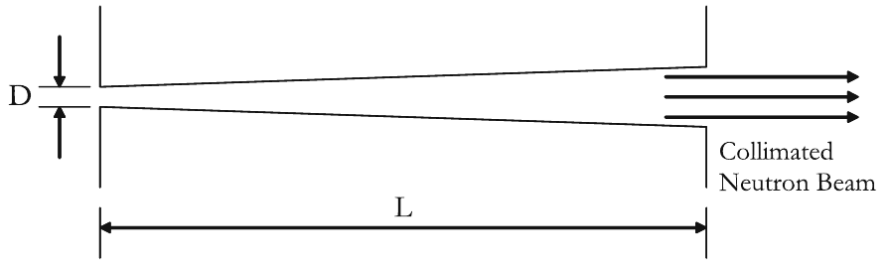

Figure 2.18: Divergent collimator of a neutron imaging system illustrating the collimator tube length (L) and its aperture diameter (D). After [And09].

Exposure times

Although the exposure time depends on the facility characteristics, the reactor at the Institute of Atomic and Subatomic Physics in Vienna has a thermal flux of 1.3×10^5 n cm^{-2} s^{-1} and it can have exposure times as low as 20 seconds per image [Ins]. This means that it is possible to perform a set of measurements necessary for neutron tomography (about 200 images) within a few hours [Ins].

2.2.4 Detectors

Since neutrons are neutral, they do not produce direct ionization events and detecting neutrons must be based on detecting secondary events produced by nuclear reactions. These nuclear reactions can be (n,p), (n,α), (n,γ) or (n,fission), or by nuclear scattering from light charged particles which are then detected [Kra88]. In table 2.5 some neutron detectors are listed along with their efficiencies. There are three main classes of detectors for neutrons in general and for neutron imaging in particular. They are [And09]:

- Scintillator and storage phosphor detectors

- Gas detectors
- Solid-state detectors

Table 2.5: Typical values of efficiency for some common neutron detectors. The neutron detection efficiency is for neutrons with the specified energy striking the detector face at right angles. Adapted from [Cra91].

Detector type	Size	Neutron active material	Incident neutron energy	Neutron detection efficiency (%)
Plastic scintillator	5 cm thick	^{1}H	1 MeV	78
Liquid scintillator	5 cm thick	^{1}H	1 MeV	78
Loaded scintillator	1 mm thick	^{6}Li	thermal	50
Hornyak button	1 mm thick	^{1}H	1 MeV	1
Methane (7 atm)	5 cm diam	^{1}H	1 MeV	1
^{4}He (18 atm)	5 cm diam	^{4}He	1 MeV	1
^{3}He (4 atm), Ar (2 atm)	2.5 cm diam	^{3}He	thermal	77
^{3}He (4 atm), CO_2 (5%)	2.5 cm diam	^{3}He	thermal	77
BF_3 (0.66 atm)	5 cm diam	^{10}B	thermal	29
BF_3 (1.18 atm)	5 cm diam	^{10}B	thermal	46
^{10}B-lined chamber	0.2 mg/cm^2	^{10}B	thermal	10
Fission chamber	2.0 mg/cm^2	^{235}U	thermal	0.5

Scintillator and storage phosphor detectors

A neutron scintillator is a material that absorbs neutrons and emits low-energy photons. The scintillator is then coupled to an optical system to detect the photons created in the scintillator. As the optical system changes, the detectors can be [And09]:

- *Photographic scintillation detector*: a photographic film is used to make the readout. This solution has two disadvantages, low light collection efficiency and the need to change the film to make the readout [And09]. More recently, the use of charge-coupled device (CCD) cameras has transformed this technology into a competitive high resolution imaging system [And09]. A typical system is depicted in figure 2.19
- *Counting scintillation detectors*: the light detection is made with photomultipliers [And09]

Another type of detector is the *storage phosphors*. These detectors are functionally similar to scintillators, except that, instead of a prompt light emission, energy is stored. The phosphor is read by photostimulation (typically by scanning with a laser), inducing light emissions (figure 2.20).

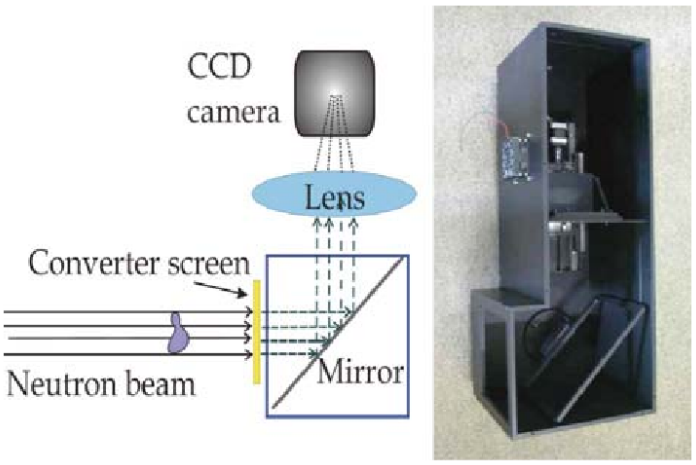

Figure 2.19: Neutron imaging system with a CCD as optical system. *Left*: Neutrons hitting the scintillator are converted into visible light that is collected on the CCD of a camera. *Right*: Light-proofed box containing mirror, CCD optics, and camera. After [And09].

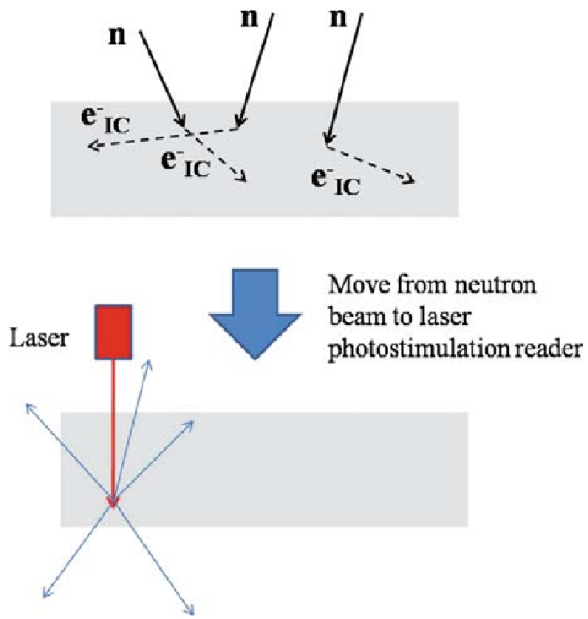

Figure 2.20: A gadolinium-157-based image plate accumulates energy from internal conversion electrons produced in neutron capture in its storage phosphor. The image plate is transferred to a reading system. A laser scans the image plate and photostimulates the release of blue photons from the storage phosphor in the image plate. After [And09].

Gas detectors

In a gas detector, the radiation enters in a chamber filled with gas and produces ionization events (*e.g.*, neutron capture). Inside the chamber an electrical potential difference causes the ions produced to accelerate and produce more ionization events (figure 2.21). This sequence of events repeats itself until the charge is detected by the plates responsible for the

potential [Kra88, And09]. Common gas converters are ^{4}He, ^{3}He and BF_3 (table 2.5).

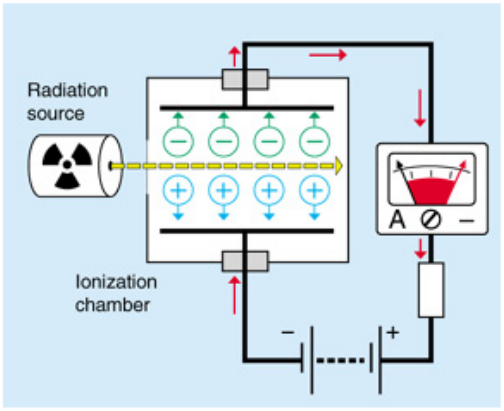

Figure 2.21: Gas detector principle. After [Soc].

Solid-state detectors

If the charged particles from a neutron capture enter a semiconductor device, the resultant ionized region will produce a pulse. If the pulse is large enough, the device becomes a neutron detector that can be coupled to fast readout counting electronics. Potential advantages of semiconductor detectors include high data rate, small size, and very low power requirements [And09].

2.2.5 Applications

There are several possible applications for neutron imaging. For example industrial research and investigation, homeland security, and museologic studies, among others. The next set of images shows some applications.

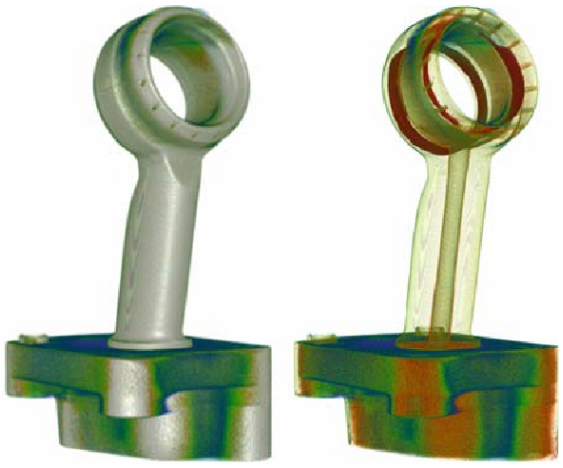

Figure 2.22: Three-dimensional reconstructions of parts of a fuel injector device. Metallic components can be extracted or suppressed by image processing. After [And09].

Figure 2.23: Neutron imaging applied to homeland security. Optical picture (left) and a neutron image of an aircraft container (right). After [And09].

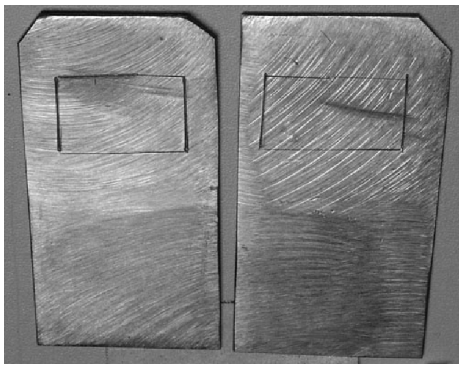

(a) Two smooth-polished metal sheets brought by the police to Schillinger's team, which were originally car chassis numbers plates.

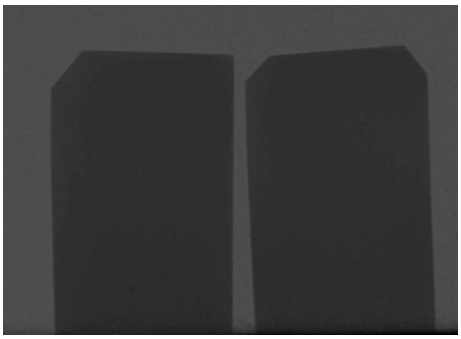

(b) X-ray image.

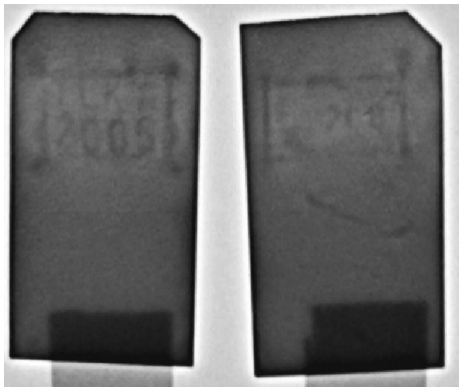

(c) Neutron image.

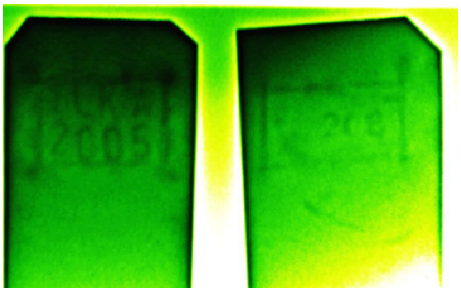

(d) Another neutron image with a different color scale.

Figure 2.24: Another example of neutron imaging applied to homeland security. After [Sch]

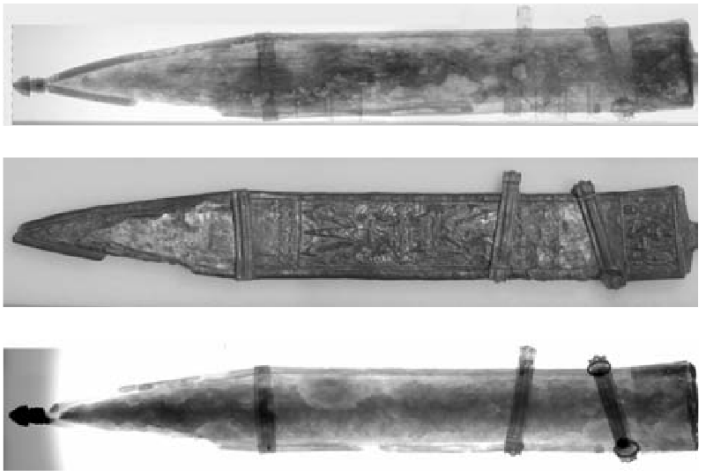

Figure 2.25: A Roman sword (photo in the middle) inspected with X-rays (upper image) and thermal neutrons (lower image). After [Leh06].

2.3 Neutron activation analysis

The principle of activation analysis is that a particle (neutron, proton, alpha particle, etc.) or photon (gammas, bremsstrahlung) induces a nuclear reaction in an atom of a target element [Fil95]. The product of the reaction is detected and quantified by prompt photon or particle emission or, more commonly, by its decay properties, if radioactive. For neutron activation analysis (NAA), in which neutrons are used, several nuclear reactions are possible depending on the target nucleus and the neutron energy [Fil95].

NAA is comprised by several different techniques:

- *Instrumental neutron activation analysis* (INAA): is the most commonly used technique and is characterized by the quantification of the product radionuclide. This quantification is dependent on its decay mode and half life and is done through high resolution gamma-ray spectroscopy using Ge, Ge(Li) or Si(Li) detectors [Fil95]
- *Radiochemical neutron activation analysis* (RNAA): with some elements, or combination of elements, an elemental separation from the sample is needed. This can be done before irradiation or after, and also re-irradiation can be performed if needed [Fil95]
- *Epithermal and fast neutron activation analysis* (ENAA and FNAA): with some elements can be advantageous to use epithermal or fast neutrons instead of thermal neutrons. This can be done to take advantage of some resonance in the excitation function of some elements (section 1.2) [Fil95]
- *Prompt gamma-ray neutron activation analysis* (PGNAA): this technique differs from the other activation methods in that the prompt gamma-rays are measured rather than the radioactive product [Fil95]

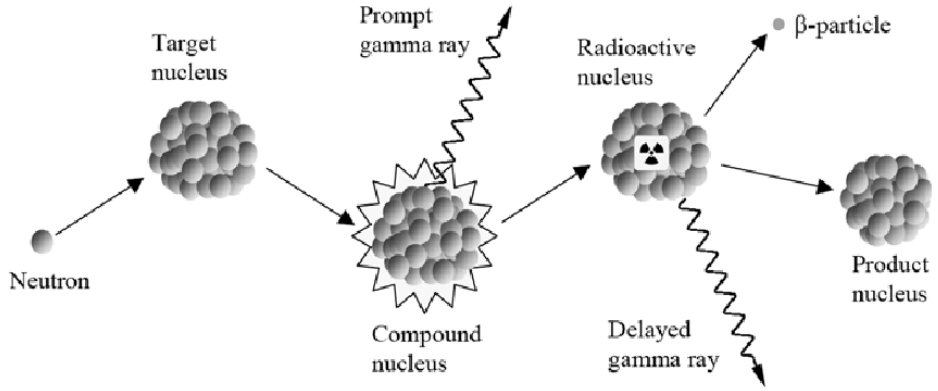

Figure 2.26: Nuclear processes involved in prompt gamma-ray neutron activation analysis and neutron activation analysis: neutron capture is immediately followed by emission of prompt gamma-rays. The compound nucleus decays by beta emission followed by the emission of delayed gamma-rays. After [And09].

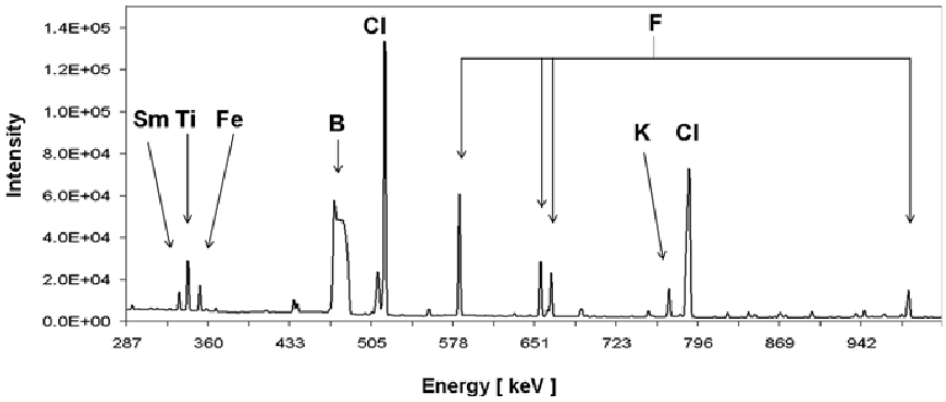

Figure 2.27: Example of prompt gamma-ray neutron activation analysis spectrum from an estuarine sediment. After [And09].

Part II

Simulation studies

Chapter 3

Validation of Geant4

Although several other models of physics processes are involved in the simulations (electromagnetic, optical, and decay, for example), the focus should be the hadronic models differences because this work involves protons and neutrons. Therefore, three hadronic models were tested:

- *Precompound model*: this model was tuned during this work, since the code came originally from the Geant4 hadrontherapy example. The difference from the model used was the cut values for electrons. All models together form a Geant4 physics list[1] and the hadronic options activated for the simulations were:
  - Elastic Scattering for all the hadrons and ions
  - Inelastic scattering: precompound + evaporation (generalized evaporation model) [2] for protons, neutrons, and pions
- *QGSP_BIC_HP*[3]: this package[4] uses Geant4 Binary cascade (BIC) for primary protons and neutrons with energies below ∼10 GeV. Also, it has the high precision (HP) neutron library to simulate the transport of neutrons below 20 MeV down to thermal energies [CER]
- *QGSP_BERT_HP*[5]: this is another Geant4 package, which uses the Bertini cascade for primary protons, neutrons, pions and kaons below ∼10 GeV. As the package name indicates, it has also the high precision neutron library [CER]

3.1 Validation of (p,n) reactions

One of the possible applications of proton cyclotrons is neutron production through (p,n) reactions. Validation of Geant4 aims at testing its accuracy in reproducing experimental data. The work of Verbinski and Burrus was used to perform such validation [Ver69].

[1] A physic list is a class which collects all the particles, physics processes and production thresholds needed for the application [Wri09b]

[2] See appendix C.2

[3] Quark-gluon string precompound binary cascade high-precision neutron library

[4] The term package is applied in this case because this is one of the many packages included with Geant4 that assembles all necessary models (and the recommended for specific cases) in one package. The packages in Geant4 can be initiated with only one command line in the main Geant4 file.

[5] Quark-gluon string precompound Bertini high-precision neutron library

3.1.1 Setup

Table 3.1: Proton stopping power and density of the target used. The value of proton stopping power and density are from NIST database [Phy] and from WebElements [Win], respectively.

Target	**Proton stopping power (MeV cm^2 g^{-1})**	**Density (g cm^{-3})**
beryllium-9	22.75	1.848

Table 3.2: Quantities related to proton energy and target thickness. Here the initial proton energy (E_p), the average proton energy in the target ($\langle E_p \rangle$), the loss of energy in the target (ΔE), and the calculated target thickness are presented. Adapted from [Ver69].

Target	**E_p (MeV)**	**$\langle E_p \rangle$ (MeV)**	**ΔE (MeV)**	**Target thickness (μm)**
beryllium-9	18.57	18.0	1.06	25.2

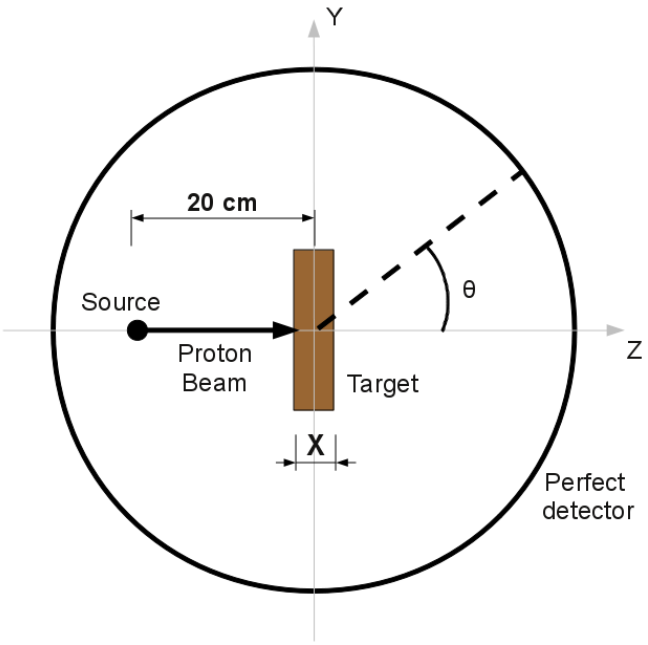

Figure 3.1: Setup used for Geant4 (p,n) reactions validation. Inside a perfect detector (spherical surface with a 30 centimeters radius), at the reference origin, is placed a target with a thickness of X (table 3.2). The proton source is localized at $z = -20\ cm$. This setup was simulated in vacuum and with an idealized pencil beam.

3.1.2 Results

In the first simulations with protons it was seen a shift of about 1% in the detected energy against the expected energy. This was corrected by introducing a correction for relativist

effects . Although this effect for deuterons and californium-252 is negligible due to the energies involved, its simulations were also made with this correction. So, the neutron kinetic energy was given by:

$$KE = \sqrt{{p_x}^2 + {p_y}^2 + {p_z}^2 + nRM^2} - nRM \tag{3.1}$$

Where KE is the neutron kinetic energy, p_x, p_y, and p_z are the three neutron momentum components, and nRM is the neutron rest mass (939.6 MeV/c^2).

Beryllium-9

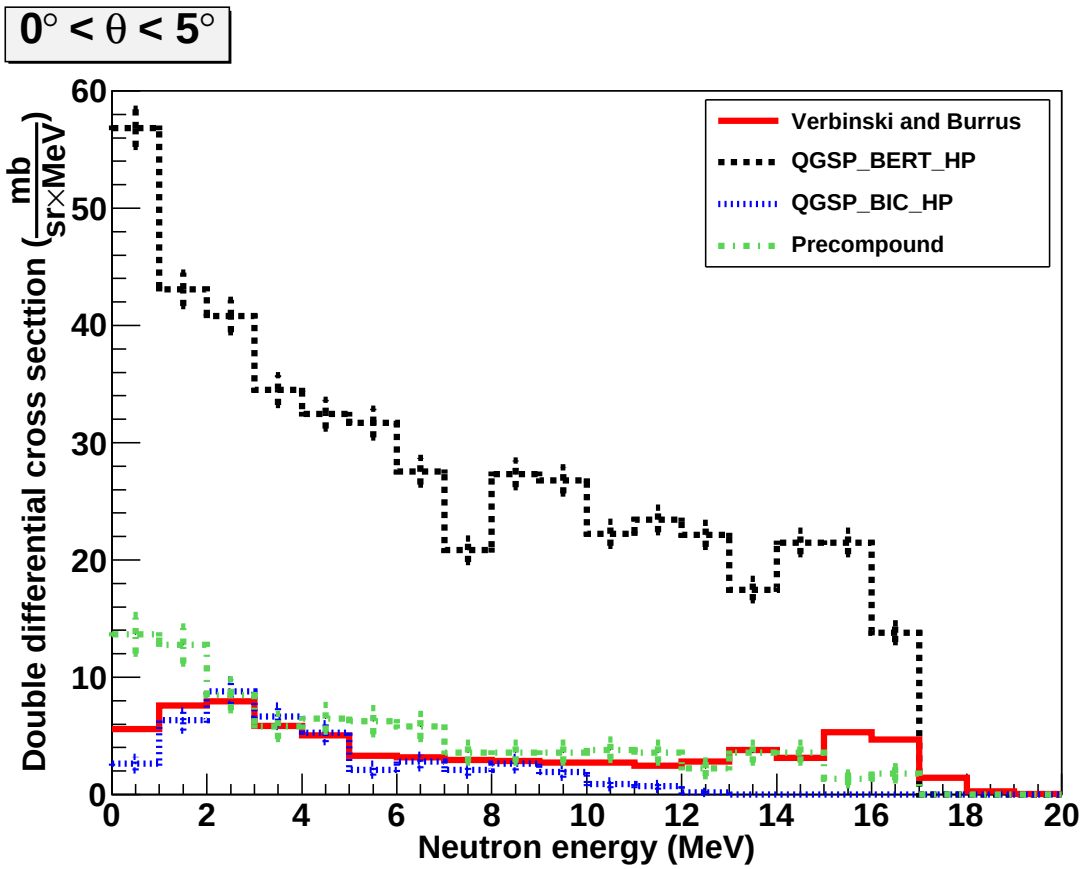

Figure 3.2: Comparison of experimental and simulated double differential cross sections for the ^{9}Be(p,n)^{9}B reaction ($0° < \theta < 5°$).

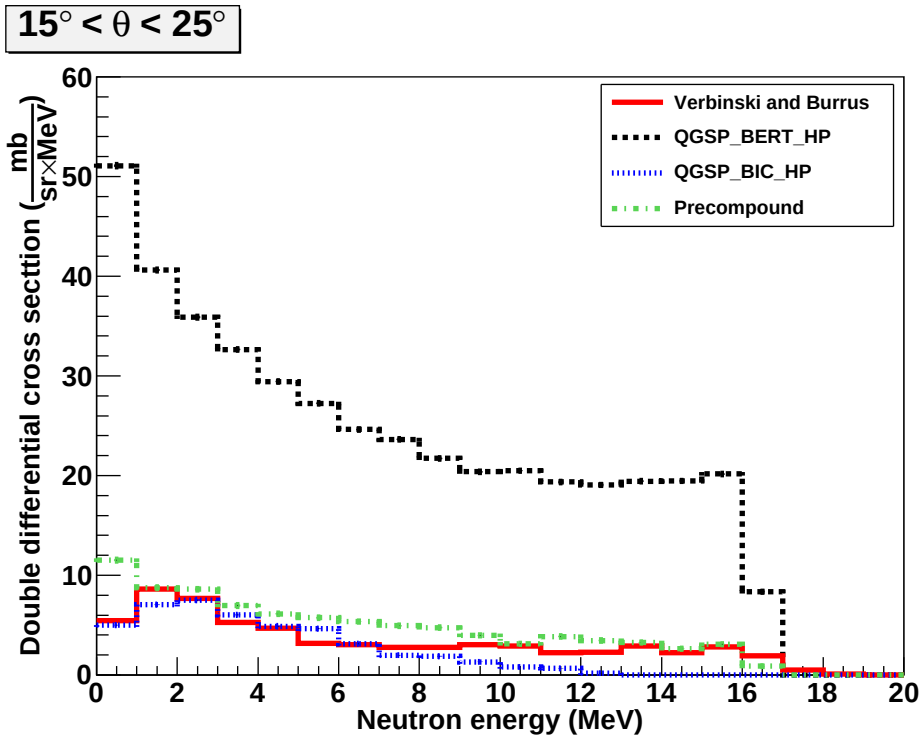

Figure 3.3: Comparison of experimental and simulated double differential cross sections for the ^{9}Be(p,n)^{9}B reaction ($15^{\circ} < \theta < 25^{\circ}$).

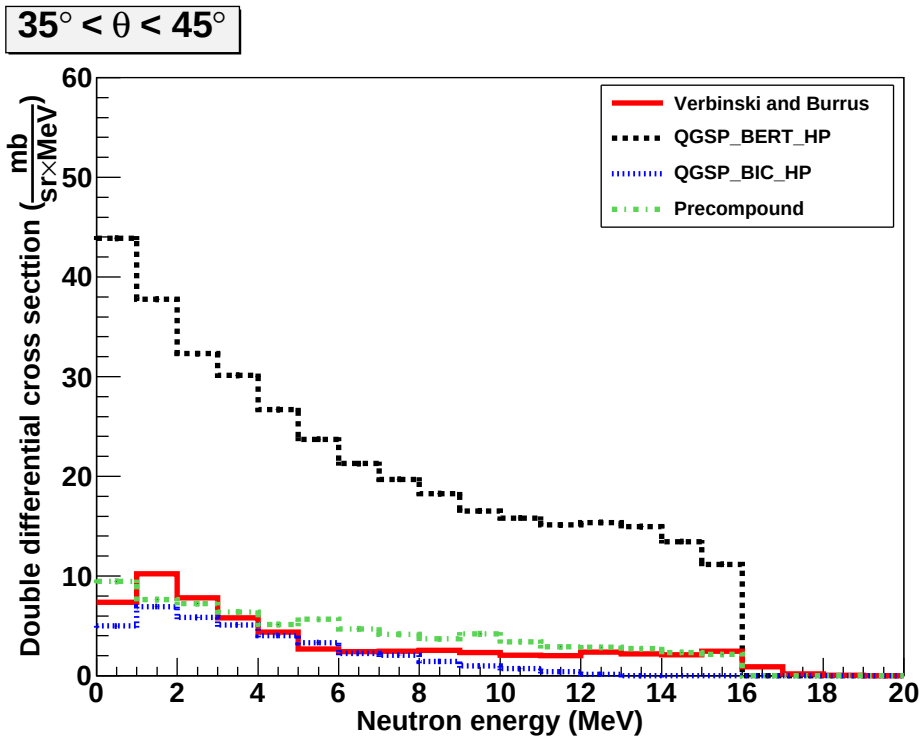

Figure 3.4: Comparison of experimental and simulated double differential cross sections for the ^{9}Be(p,n)^{9}B reaction ($35^{\circ} < \theta < 45^{\circ}$).

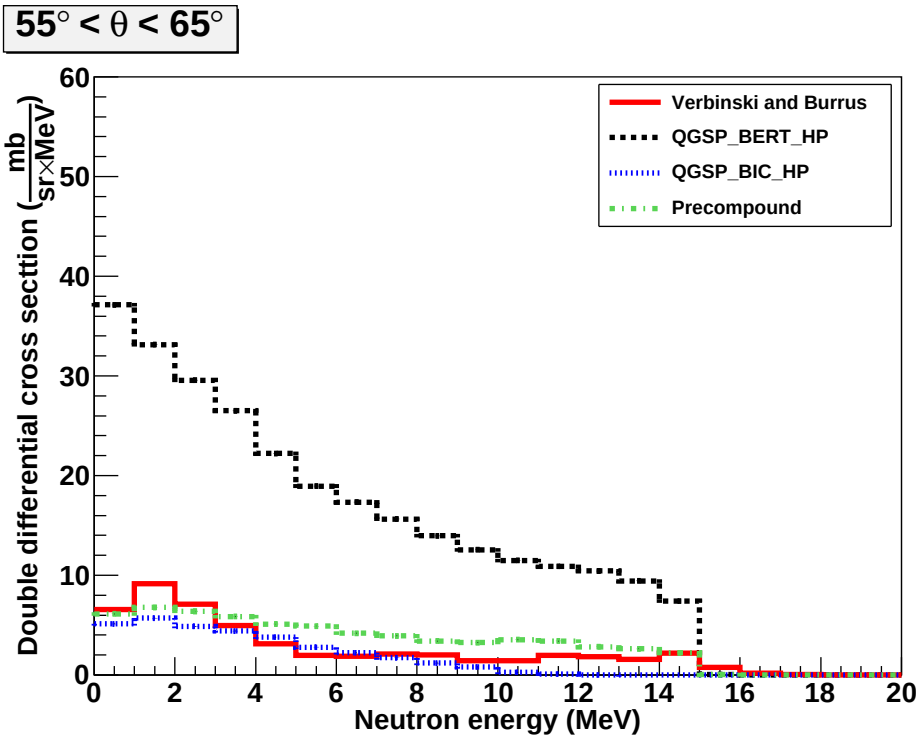

Figure 3.5: Comparison of experimental and simulated double differential cross sections for the ^{9}Be(p,n)^{9}B reaction ($55° < \theta < 65°$).

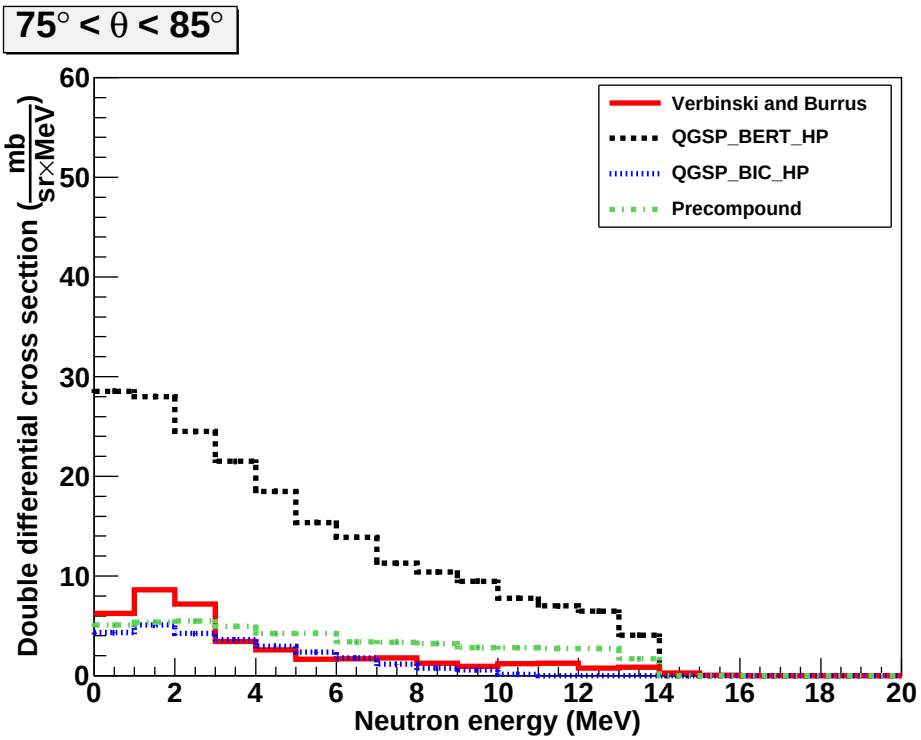

Figure 3.6: Comparison of experimental and simulated double differential cross sections for the ^{9}Be(p,n)^{9}B reaction ($75° < \theta < 85°$).

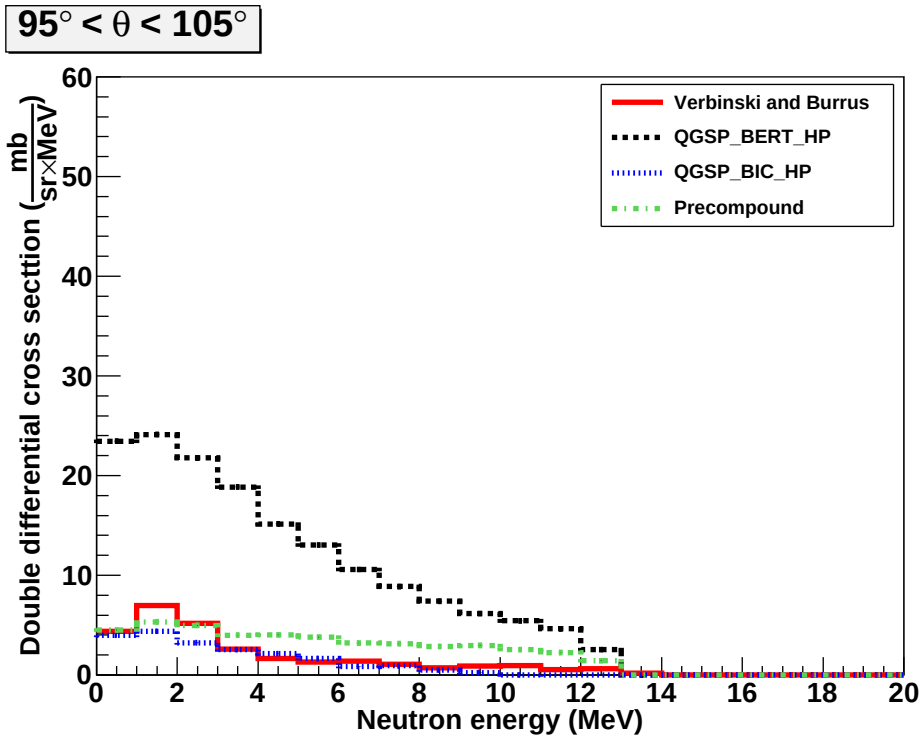

Figure 3.7: Comparison of experimental and simulated double differential cross sections for the ^{9}Be(p,n)^{9}B reaction ($95^{\circ} < \theta < 105^{\circ}$).

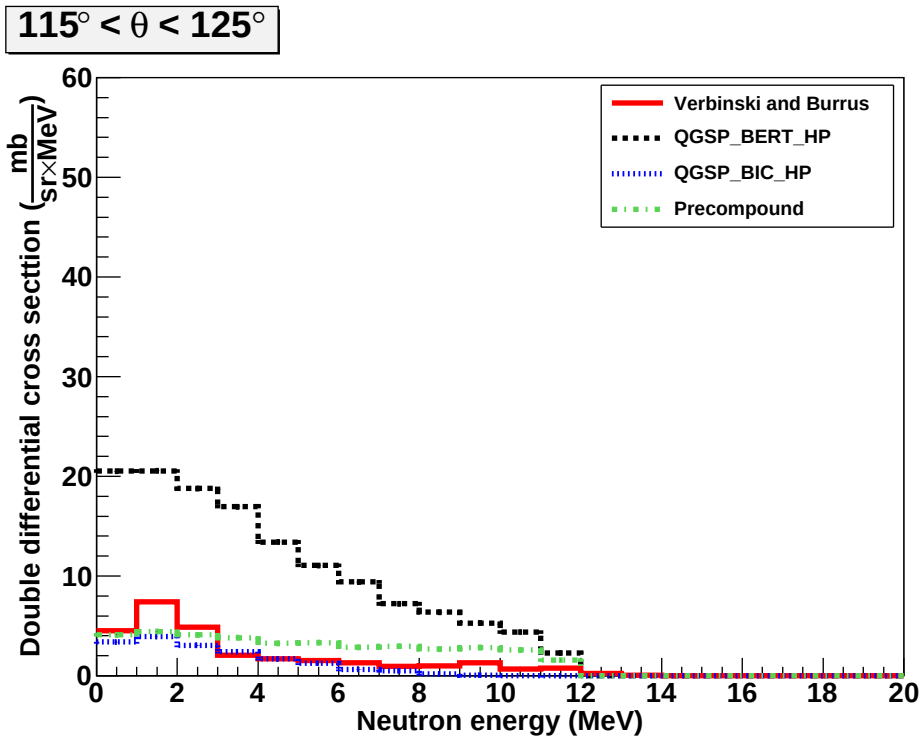

Figure 3.8: Comparison of experimental and simulated double differential cross sections for the ^{9}Be(p,n)^{9}B reaction ($115^{\circ} < \theta < 125^{\circ}$).

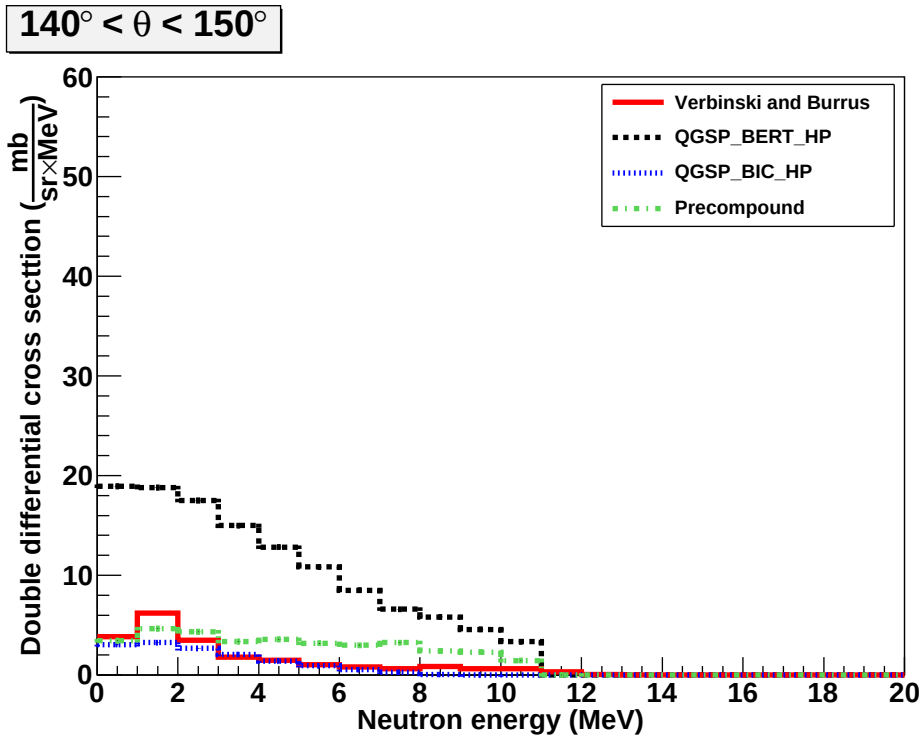

Figure 3.9: Comparison of experimental and simulated double differential cross sections for the ^{9}Be(p,n)^{9}B reaction ($140^{\circ} < \theta < 150^{\circ}$).

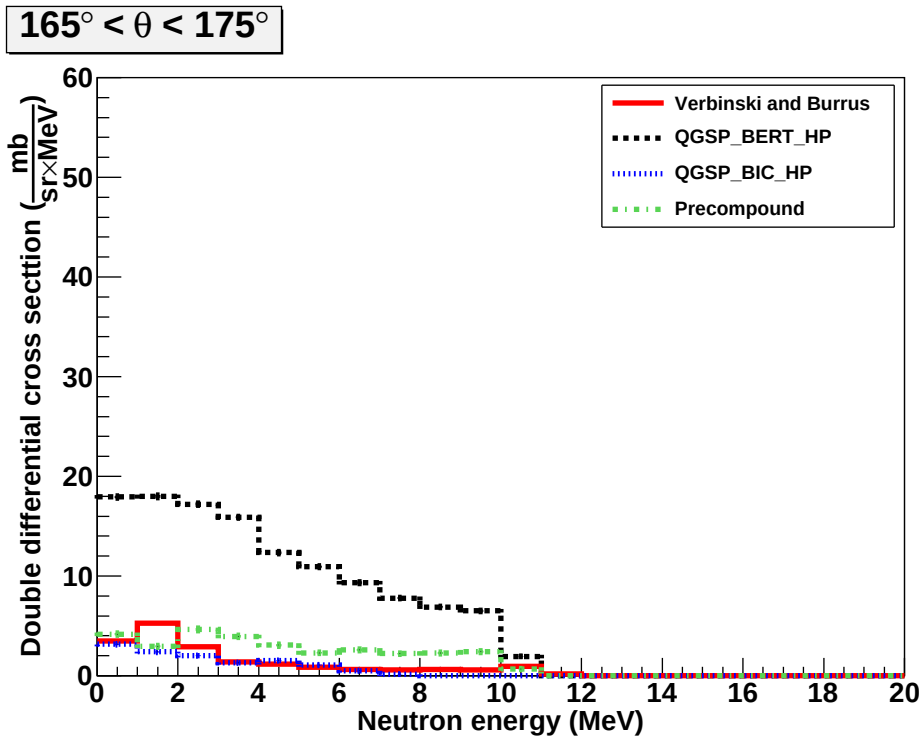

Figure 3.10: Comparison of experimental and simulated double differential cross sections for the ^{9}Be(p,n)^{9}B reaction ($165^{\circ} < \theta < 175^{\circ}$).

3.1.3 Considerations

Simulations with beryllium-9

The simulations with beryllium-9 have shown how different each model is. To make comparisons between each model an overall mean error was defined :

$$overall\ mean\ error\ =\ \frac{1}{9}\sum_{i=graph1}^{graph9}\frac{\sum_{j=1}^{20}|bin_{simulated}\ ij\ -\ bin_{experimental}\ ij|}{20} \tag{3.2}$$

Where bin is defined as a group of data (in the case of figures 3.2 to 3.10 each unit of energy is a bin).

The precompound model has demonstrated a good agreement with experimental data, with an overall mean error of 1.11, showing, however, an excessively flat neutron energy distribution. This means that some fluctuations in the experimental neutron energy were not verified with this model, the most evident being the energy peak observed near the end of experimental data.

The QGSP_BIC_HP package demonstrated results clearly not compatible with experimental data. In all angles the simulated neutron energies did not describe the full energy range, falling to zero much before the experimental ones. Although the overall mean error with QGSP_BIC_HP was 0.74 this value was achieved due to the small errors in the higher angles.

The QGSP_BERT_HP package was the worst of all, with an overall mean error of 10.68. Despite of this error, this package does not appear to have the same two problems encountered in the two previous cases: (1) it seems to describe the fluctuations of the experimantal data and (2) the neutron energy range is similar to the experimental one.

The decision of which model to use was between precompound model and QGSP_BERT_HP due to the mentioned reasons. However, to make QGSP_BERT_HP package suitable to use, one must find a constant to transform the simulated data to agree with the experimental data. Using a trial and error approach, the constant that minimizes the QGSP_BERT_HP package overall mean error is $^1/_{6.61}$ with an error of 0.59. Besides the lower error compared with precompound model, one of the features of Geant4 packages is the cpu optimization and this is obvious by comparing simulation times in section C.2 and, therefore, the QGSP_BERT_HP package will be the choice for simulating the ^{9}Be(p,n)^{9}B reaction. The next set of images shows the double differential cross sections with the QGSP_BERT_HP package correction factor.

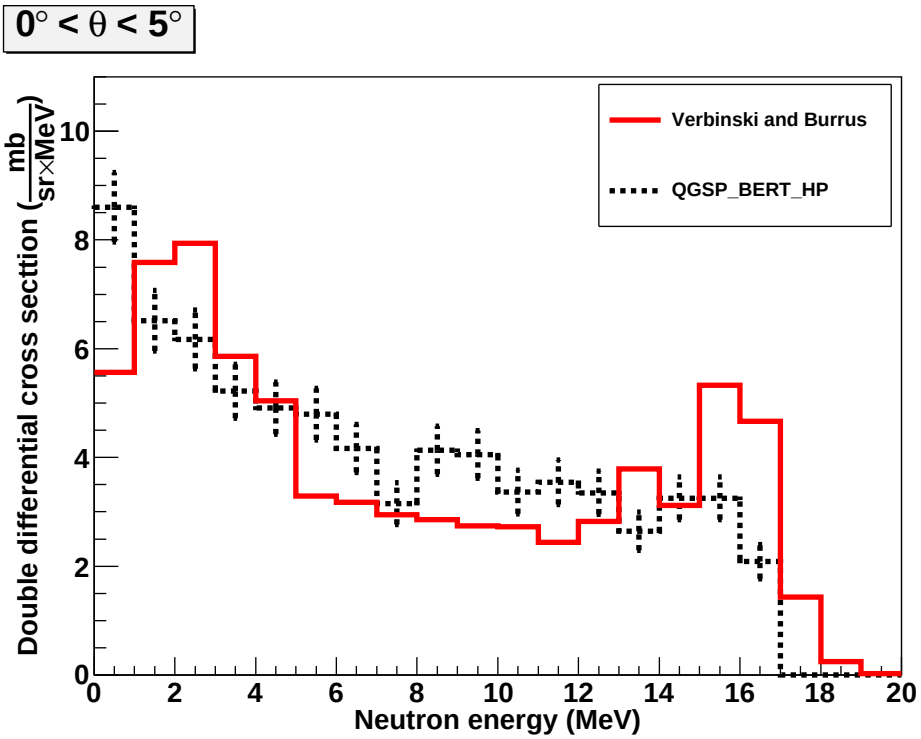

Figure 3.11: Comparison between experimental and corrected-QGSP_BERT_HP-package simulated double differential cross sections for the ^{9}Be(p,n)^{9}B reaction ($0° < \theta < 5°$).

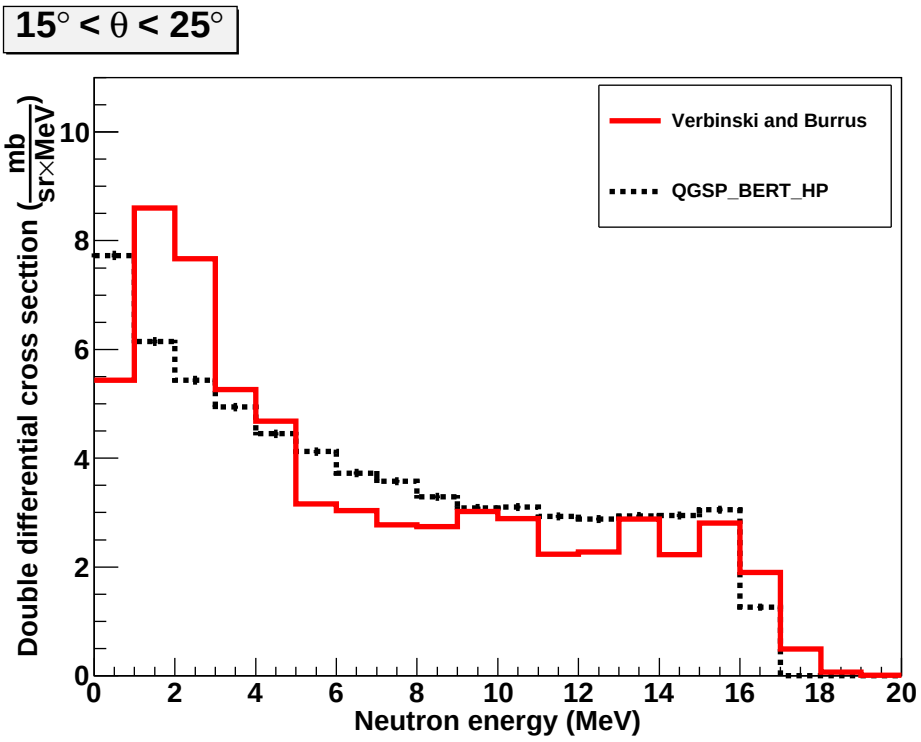

Figure 3.12: Comparison between experimental and corrected-QGSP_BERT_HP-package simulated double differential cross sections for the ^{9}Be(p,n)^{9}B reaction ($15° < \theta < 25°$).

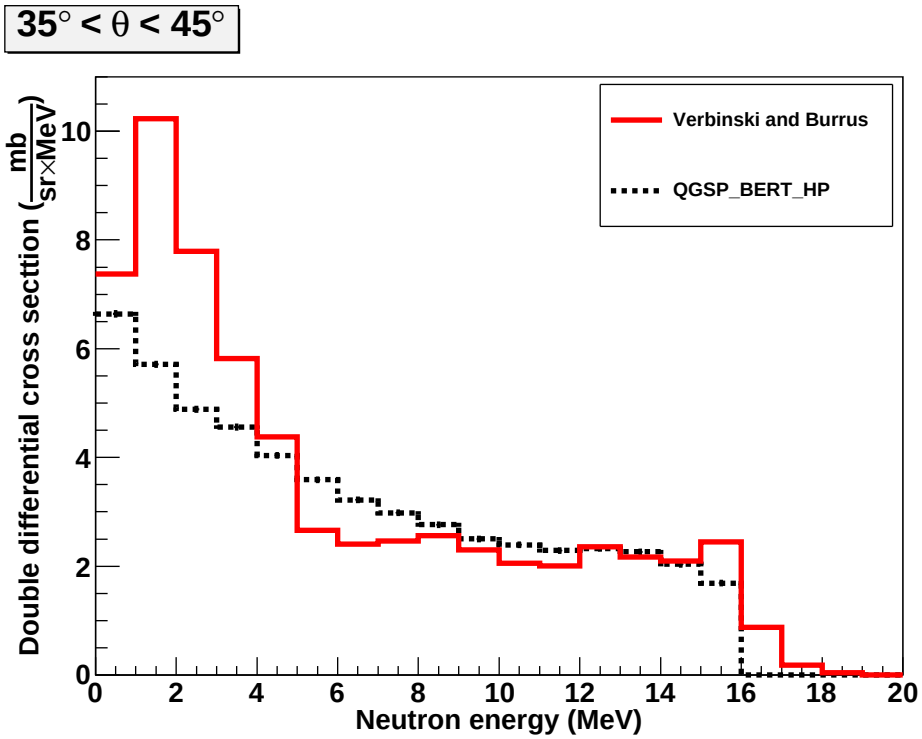

Figure 3.13: Comparison between experimental and corrected-QGSP_BERT_HP-package simulated double differential cross sections for the ^{9}Be(p,n)^{9}B reaction ($35° < \theta < 45°$).

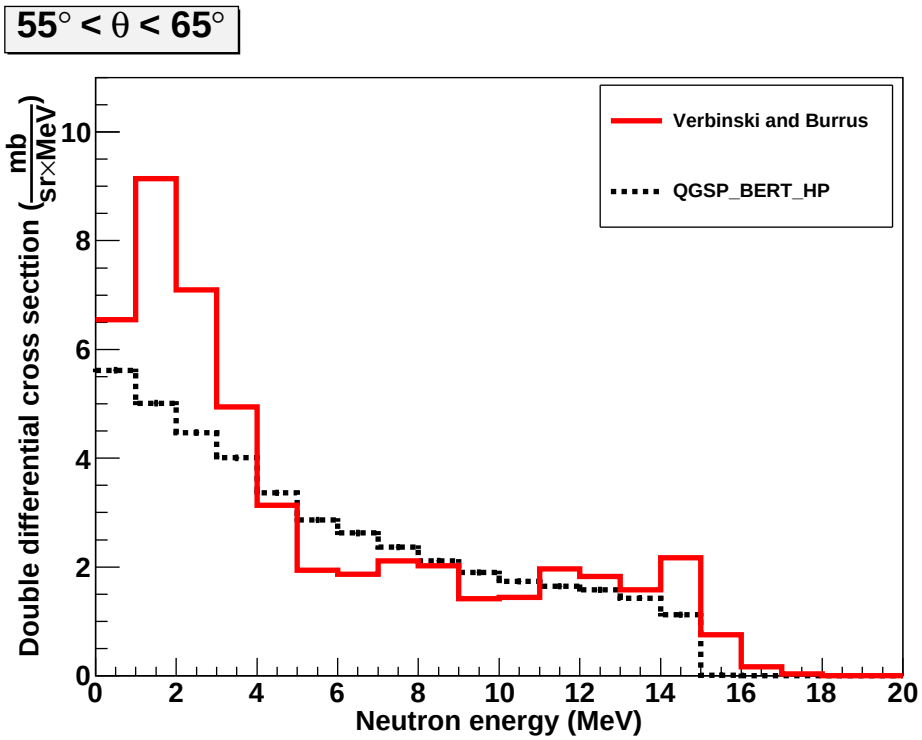

Figure 3.14: Comparison between experimental and corrected-QGSP_BERT_HP-package simulated double differential cross sections for the ^{9}Be(p,n)^{9}B reaction ($55° < \theta < 65°$).

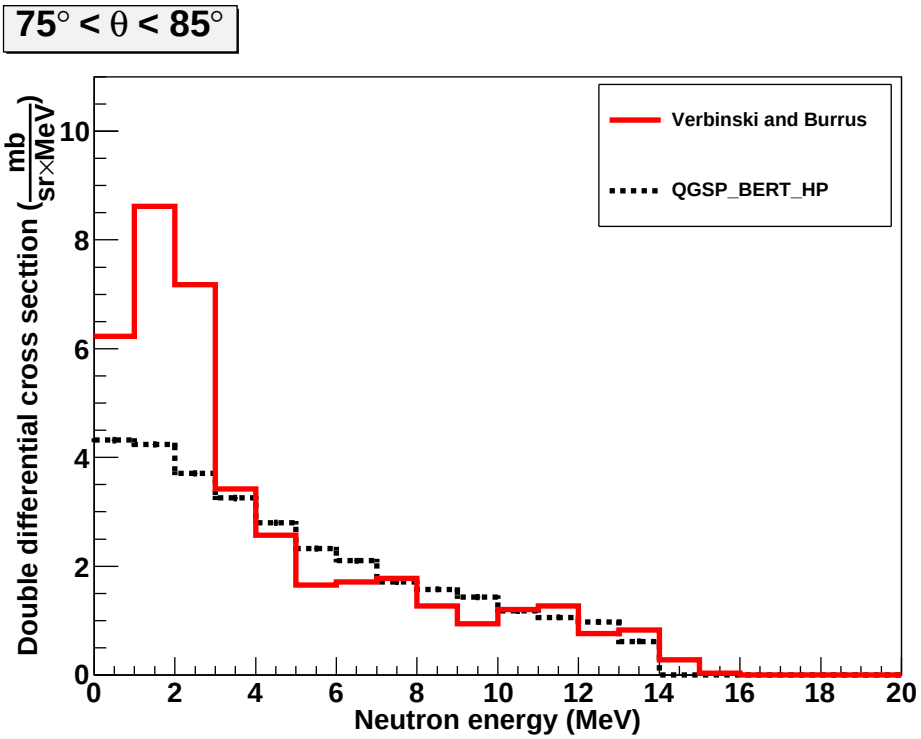

Figure 3.15: Comparison between experimental and corrected-QGSP_BERT_HP-package simulated double differential cross sections for the ^{9}Be(p,n)^{9}B reaction ($75° < \theta < 85°$).

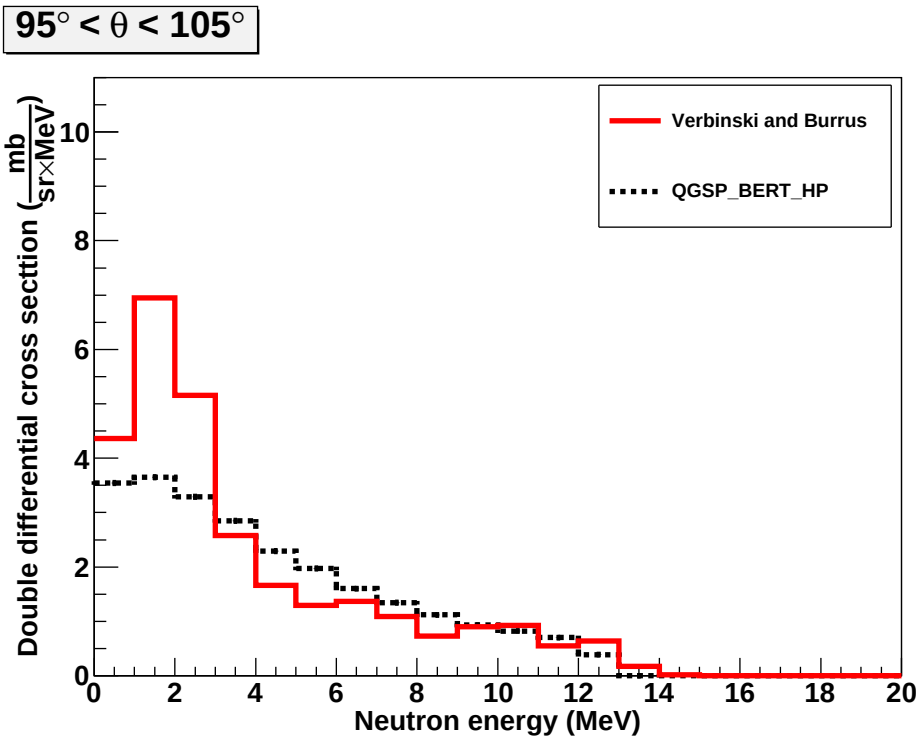

Figure 3.16: Comparison between experimental and corrected-QGSP_BERT_HP-package simulated double differential cross sections for the ^{9}Be(p,n)^{9}B reaction ($95° < \theta < 105°$).

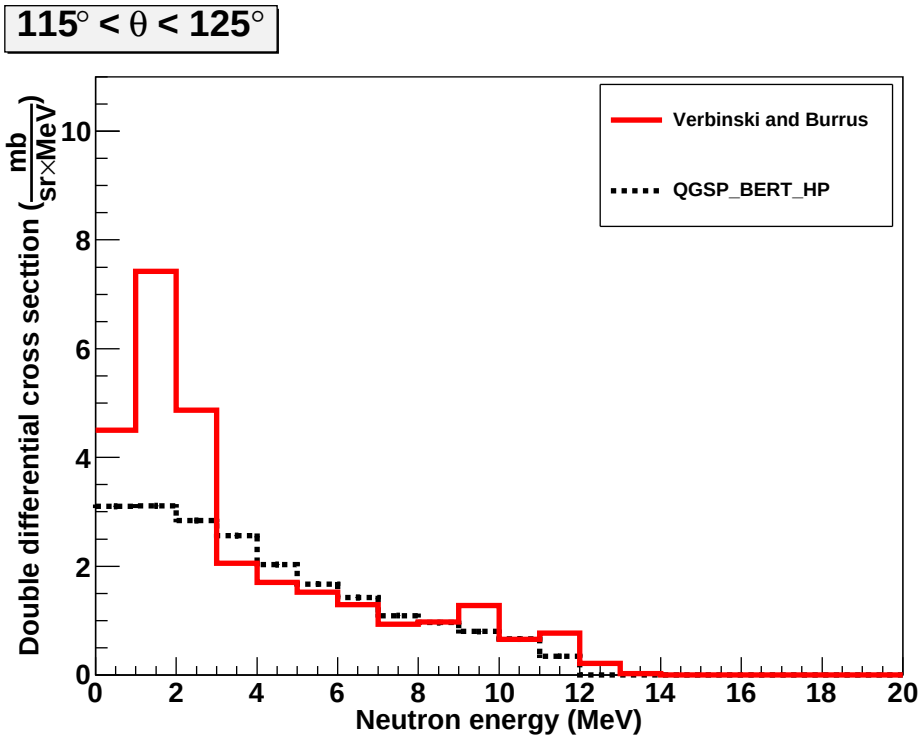

Figure 3.17: Comparison between experimental and corrected-QGSP_BERT_HP-package simulated double differential cross sections for the ^{9}Be(p,n)^{9}B reaction ($115^{\circ} < \theta < 125^{\circ}$).

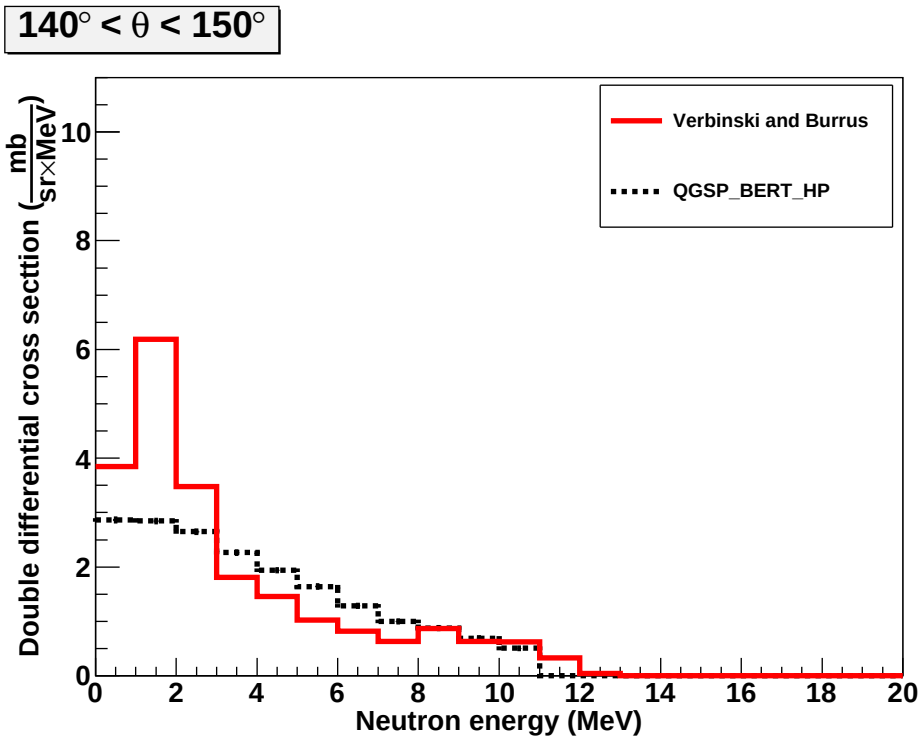

Figure 3.18: Comparison between experimental and corrected-QGSP_BERT_HP-package simulated double differential cross sections for the ^{9}Be(p,n)^{9}B reaction ($140^{\circ} < \theta < 150^{\circ}$).

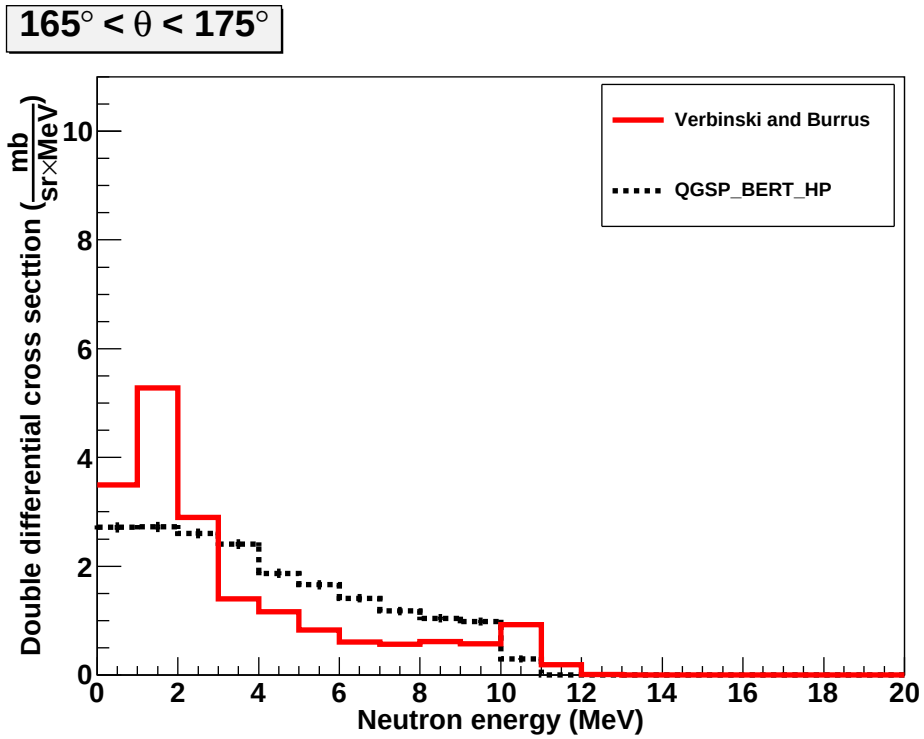

Figure 3.19: Comparison between experimental and corrected-QGSP_BERT_HP-package simulated double differential cross sections for the ^{9}Be(p,n)^{9}B reaction ($165° < \theta < 175°$).

3.2 Validation of (d,n) reactions

Some proton cyclotrons are also capable of accelerating deuterons, which through (d,n) reactions can be used to produce neutrons. The validation of Geant4 for the (d,n) reactions was made against experimental published data. It was used the work of Weaver *et al.* [Wea73].

3.2.1 Setup

The setup for this validation was the same for the (p,n) reactions validation (section 3.1.1). In table 3.3 deuterons energy and target thickness used for this validation are listed. This setup was simulated in vacuum and with an idealized pencil beam.

Table 3.3: Deuteron energy (E_d) and target thickness for (d,n) reaction validation. Adapted from [Wea73].

Target	**E_d (MeV)**	**Target thickness (μm)**
beryllium-9	8.8	53.57

3.2.2 Results

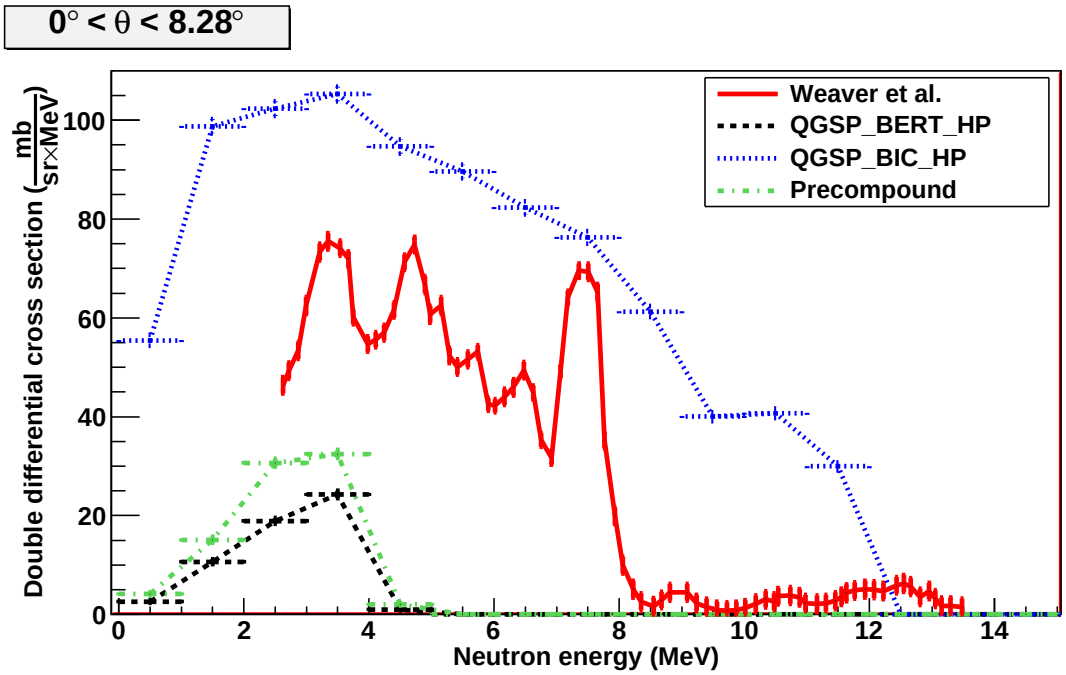

Figure 3.20: Comparison of experimental and simulated double differential cross sections for the ^{9}Be(d,n)^{10}B reaction ($0° < \theta < 8.28°$).

3.2.3 Considerations

It is difficult to analyze the graph depicted in figure 3.20 mainly because the experimental data are not equally distributed per bin. Nevertheless, one conclusion can be easily drawn: the precompound model and the QGSP_BERT_HP package are clearly not suitable for this application. The QGSP_BIC_HP package seems to yield simulated data in the same magnitude of the experimental ones. More considerations can not be drawn, not even trying a correction factor for QGSP_BIC_HP package. Despite these constraints, the package QGSP_BIC_HP will be used for ^{9}Be(d,n)^{1}0B reaction simulations.

3.3 Verification of californium-252 decay

Unfortunately, Geant4 does not have a built-in decay mode for californium-252 in its libraries[1]. Consequently, for this simulation the modelization of californium-252 decay mode was needed. Since only neutrons and gammas can pass through the double capsule of this radionuclide[2], they are the ones that should be simulated.

Neutron energy was obtained with equation 1.9 with 100 keV intervals and within the range of 0.4 MeV to 10.0 MeV. Gamma emission energy was considered to be a Gaussian distribution with an average of 0.87 MeV and a sigma of 0.020 MeV [Val99]. Both neutrons and gammas

[1] See appendix C.2 for informations about the version used
[2] Californium-252 is only available with a double encapsulation protection

have an isotropic spatial distribution[1].

3.3.1 Setup

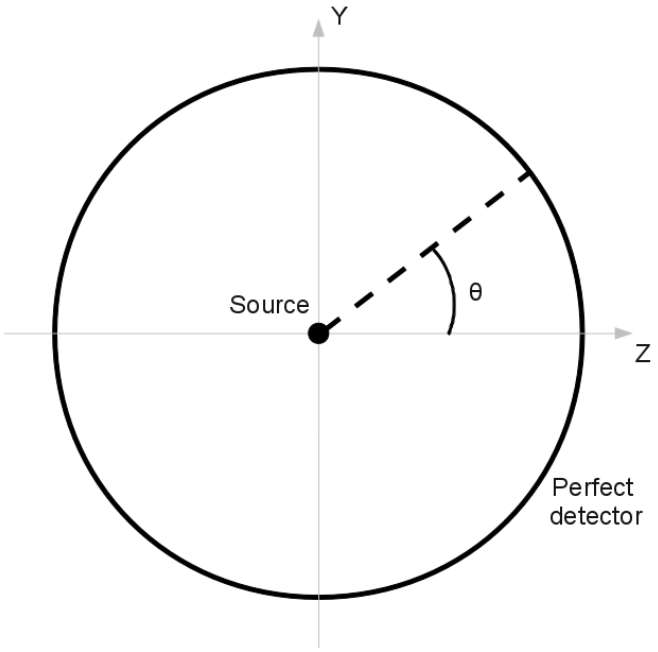

Figure 3.21: Setup used for Geant4 californium-252 decay mode verification. Inside a perfect detector (spherical surface with a 30 centimeters radius), at the reference origin, the source is placed. This setup was simulated in vacuum.

3.3.2 Results

Table 3.4: Parameters given by the Gaussian fit of californium-252 energy spectrum (bottom graph of figure 3.22).

	Mean (MeV)	**Sigma (MeV)**
Value	0.8700	0.0200
Error	5.4246×10^{-6}	3.8342×10^{-6}

Table 3.5: Californium-252 equivalent time-mass with the number of neutrons simulated.

Number of neutrons simulated	**Californium-252 equivalent time-mass ($\mu g\times s$)**
6.40227×10^{6}	$\sim$2.767

[1] Due to the encapsulation, this is not true, but for this study any eventual anisotropy is not an important issue because (1) the focus of this work is the viability of implementing a neutron beamline and not studying californium-252, and (2) the anisotropy is dependent on the californium-252 manufacturer due to different materials and methods used to make the capsule [Eis88, Rao78, Vei09]

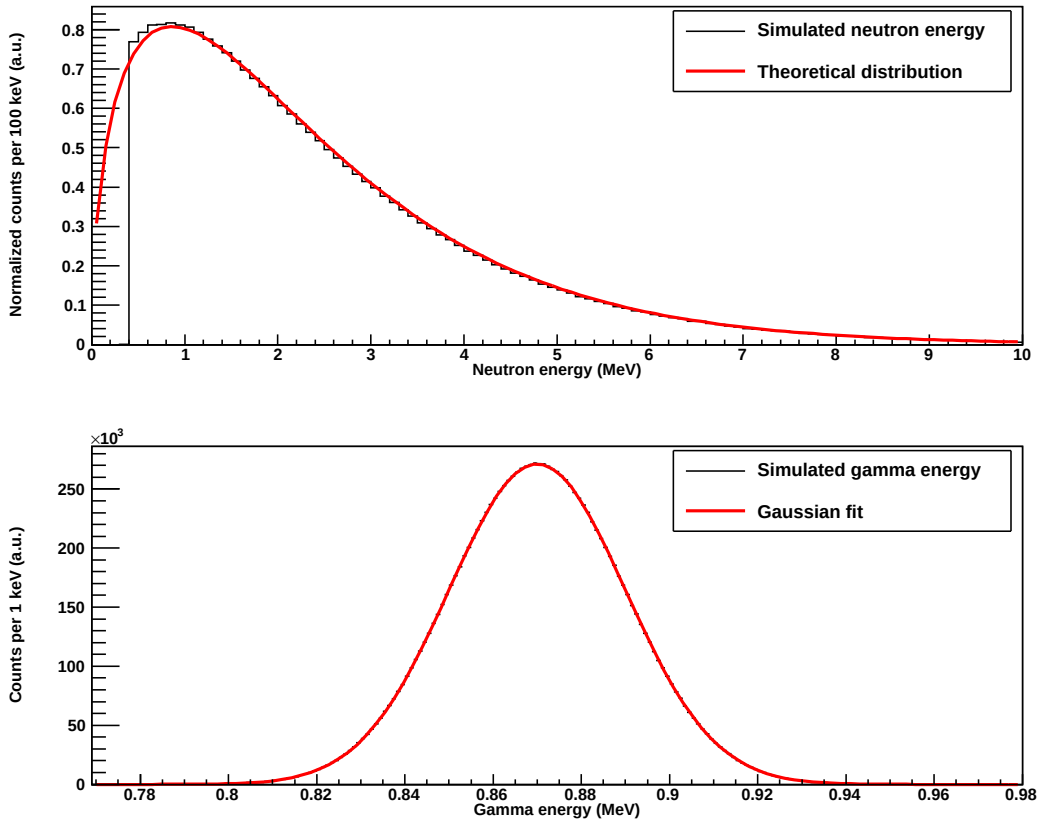

Figure 3.22: Californium-252 energy modelization verification. The upper graph is the simulated neutron energy with the theoretical spectrum yielded by equation 1.9. The bottom graph is the simulated gamma energy with a Gaussian fit. The parameters given by the fit are depicted in table 3.4

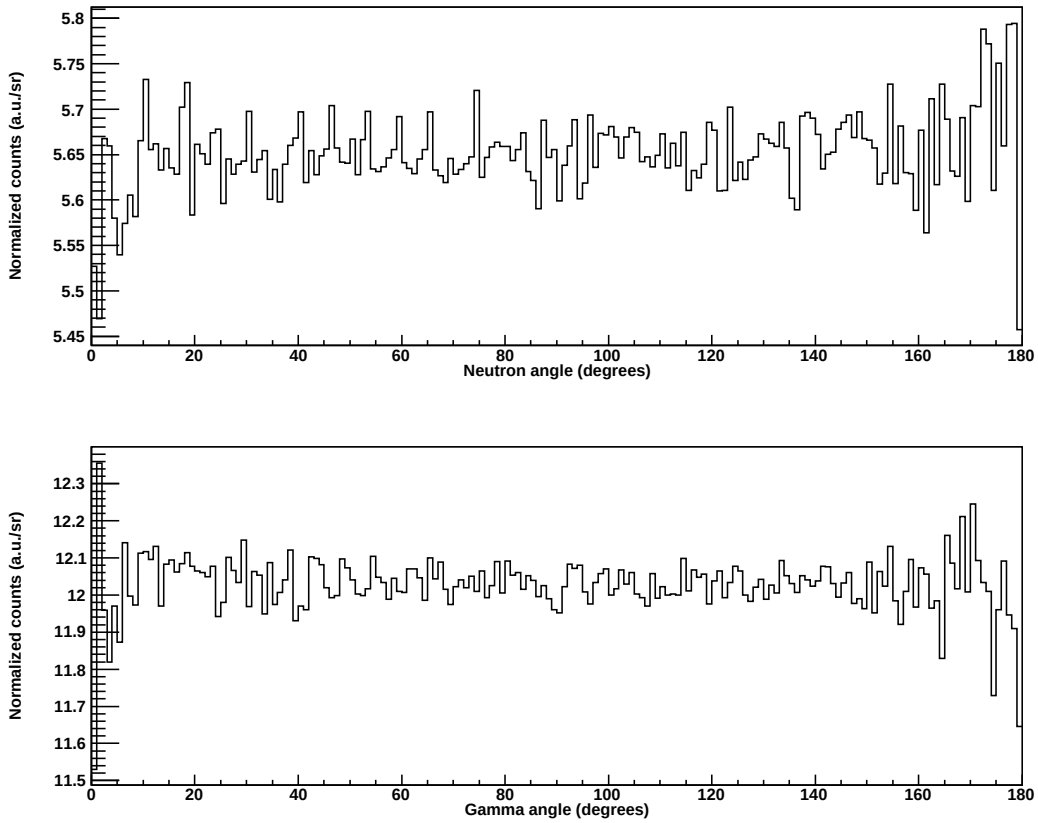

Figure 3.23: Verification of the isotropic emission of a Californium-252 source.

Chapter 4

Implementation viability

4.1 Cyclotron beam energy and dispersion

4.1.1 Setup

In order to have a good correlation with the cyclotron studied, it is also important to simulate the cyclotron port to better describe the experiment conditions. The setup used to perform this simulation was the same depicted in figure 1.6, having in this case an additional perfect detector (spherical surface with a 30 centimeters radius). The last target volume (aluminum) was placed at the reference origin and the initial beam was a pencil beam. This setup was simulated in vacuum. The table 4.1 summarizes the materials properties used in this simulation.

Table 4.1: Thicknesses and densities of the materials used in the simulation.

	Thickness (mm)	**Density**
Havar®	0.050	8.304 g cm^{-3}
Gaseous helium	20.0	0.0001786 g mL^{-1}
Aluminum	0.012	2.70 g cm^{-3}

4.1.2 Results

Protons

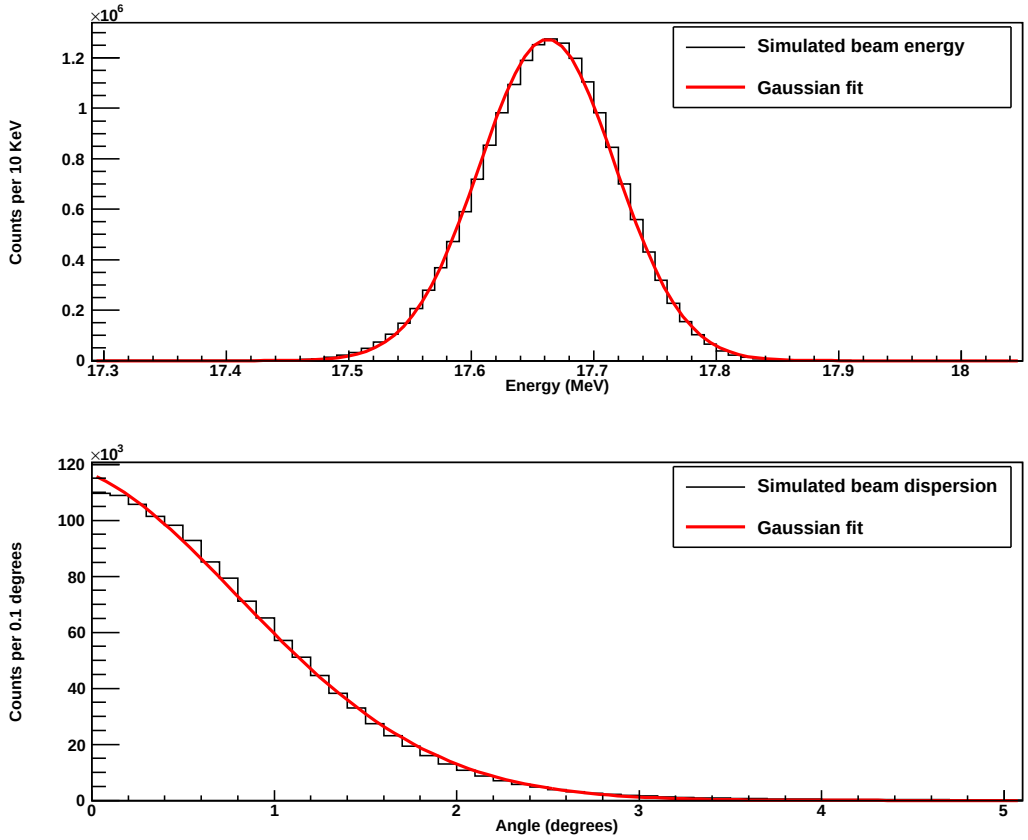

Figure 4.1: Cyclotron beam energy and dispersion for protons. The upper graph is the detected energy and the bottom graph is the angular dispersion. Both graphs were fit with a Gaussian function and the results are presented in table 4.2.

Table 4.2: Resulting parameters of the Gaussian fits depicted in figure 4.1.

	Energy (MeV)	**Angle (degrees)**
Mean	$17.66 \pm 1.34\times10^{-5}$	$-2.85\times10^{-1} \pm 6.66\times10^{-3}$
Sigma	$5.55\times10^{-2} \pm 9.31\times10^{-6}$	$1.08 \pm 2.65\times10^{-3}$

Deuterons

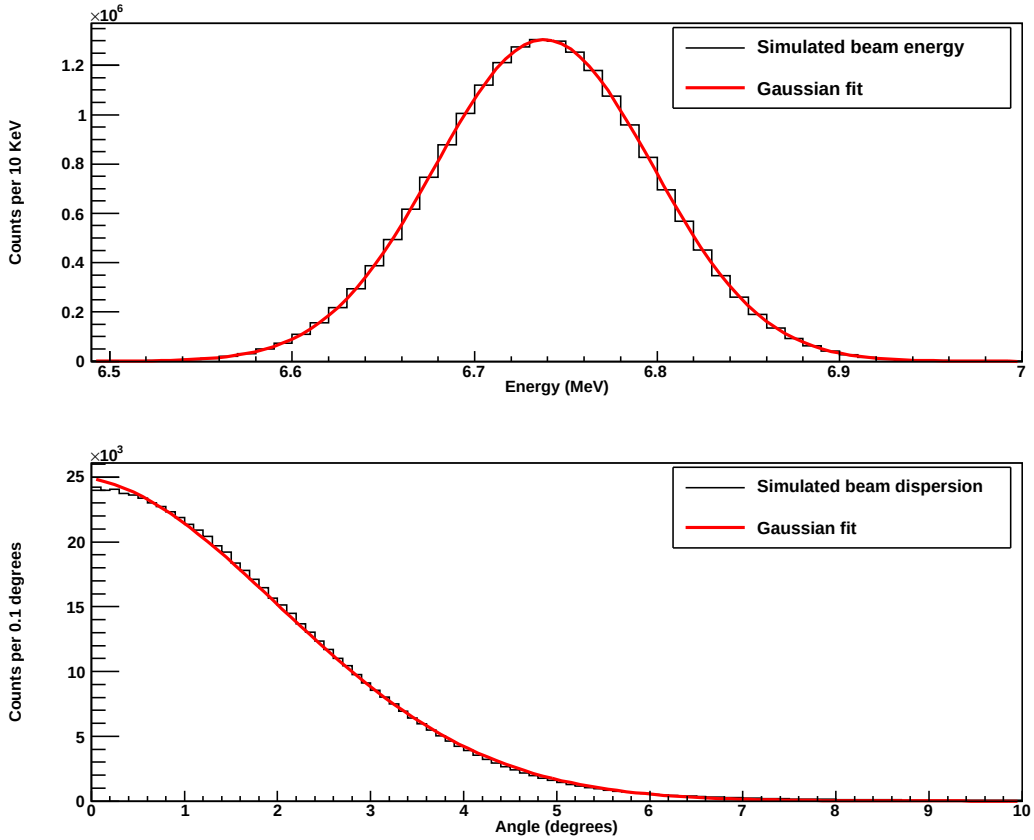

Figure 4.2: Cyclotron beam energy and dispersion for deuterons. The upper graph is the detected energy and the bottom graph is the angular dispersion. Both graphs were fit with a Gaussian function and the results are presented in table 4.3.

Table 4.3: Resulting parameters of the Gaussian fits depicted in figure 4.2.

	Energy (MeV)	**Angle (degrees)**
Mean	$6.74 \pm 1.35\times10^{-5}$	$-2.66\times10^{-1} \pm 1.68\times10^{-2}$
Sigma	$5.97\times10^{-2} \pm 9.65\times10^{-6}$	$2.26 \pm 7.10\times10^{-3}$

4.2 Thick target optimization

For thick target optimization, three different yields were considered, a total yield, a yield at 60°, and a yield at 89°. The total yield is related to the total neutron production in 4π sr. The yields at 60° and 89° are proportional to the neutrons produced in a forward solid angle of 60° and 89°, respectively. These different units can give a good idea of the neutron direction, and, if significant differences appear, it is possible to choose the optimal target thickness to get the maximum forward neutron beam. These simulations were perfomed in vacuum.

4.2.1 Reaction (p,n)

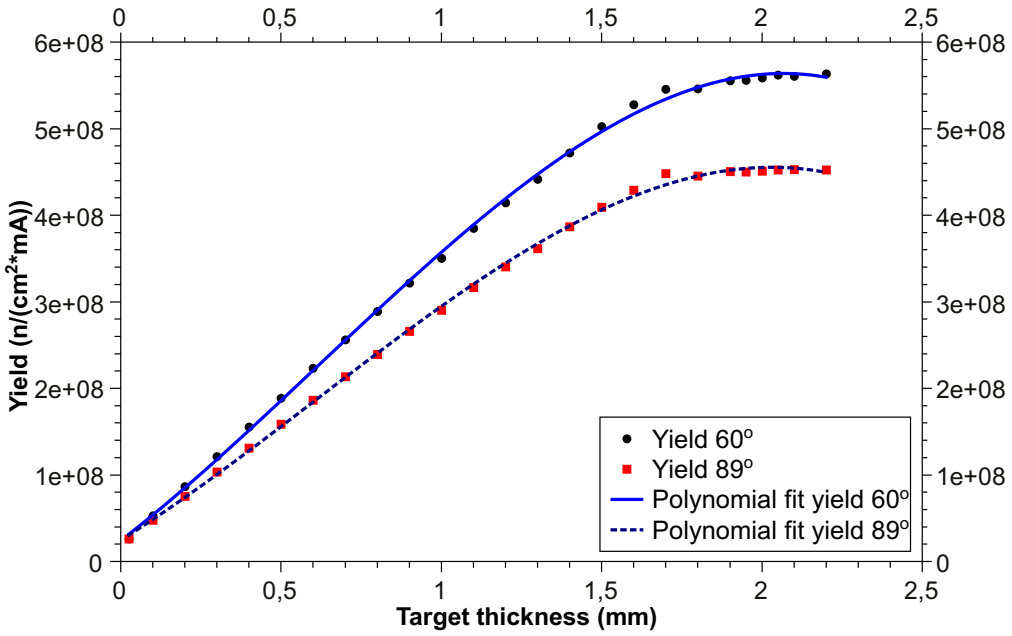

Figure 4.3: Thick target thickness optimization for the ^{9}Be(p,n)^{9}B reaction with yield 60°and yield 89°. Both curves were fit with a grade 3 polynomial function.

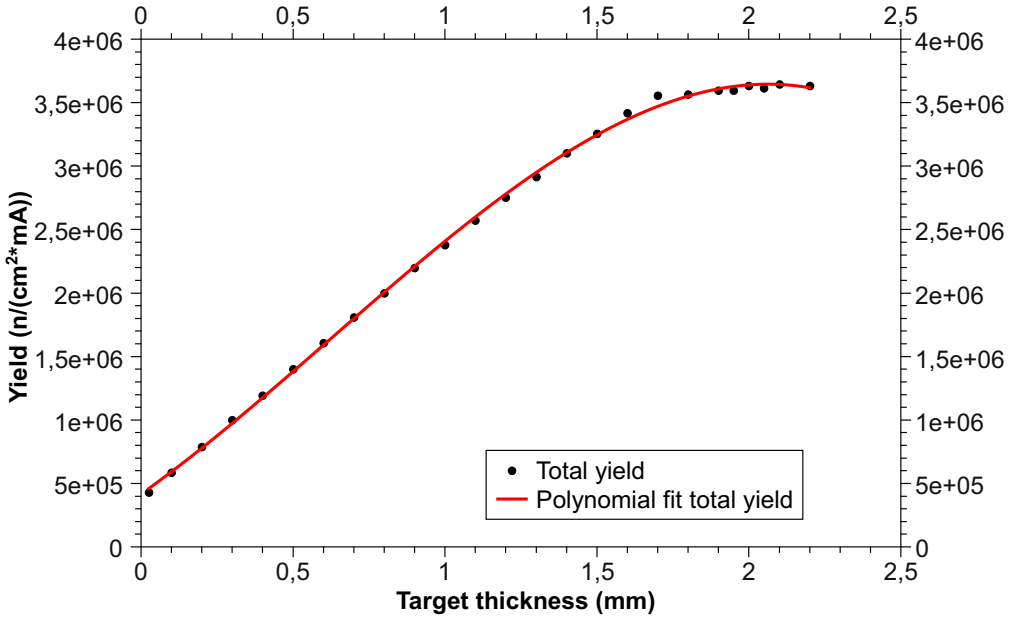

Figure 4.4: Thick target thickness optimization for the ^{9}Be(p,n)^{9}B reaction with total yield. The curve was fit with a grade 3 polynomial function.

Table 4.4: Optimal target thicknesses for the ^{9}Be(p,n)^{9}B reaction given by the grade 3 polynomial fit parameters. These fits are depicted in figures 4.3 and 4.4.

	Thickness (mm)
Total yield	2.063±0.1863
Yield 60°	2.067±0.1919
Yield 89°	2.031±0.1987

4.2.2 Reaction (d,n)

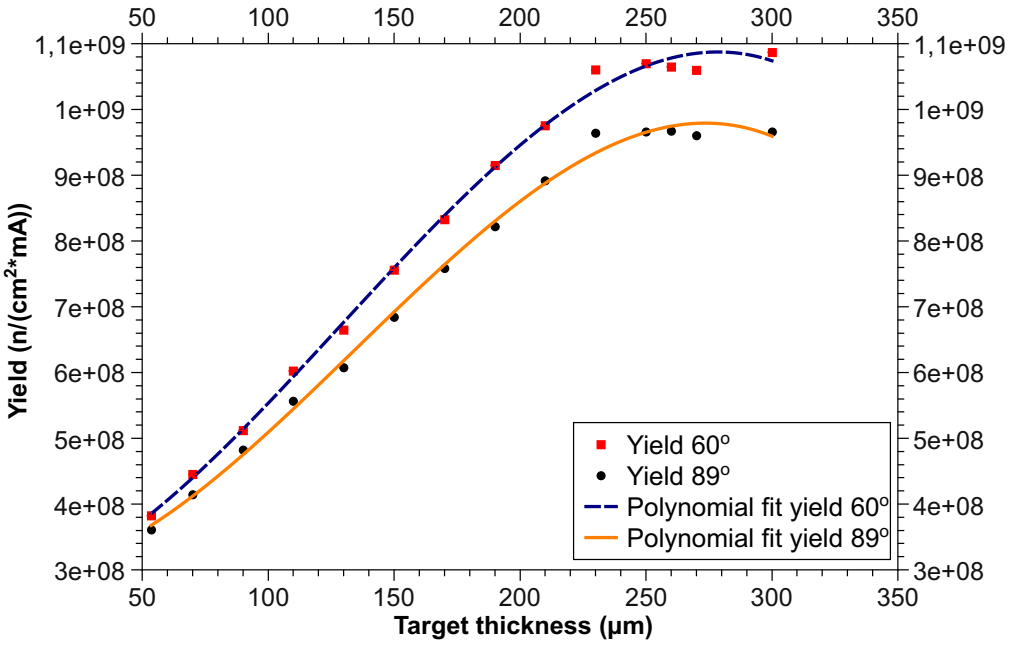

Figure 4.5: Thick target thickness optimization for the ^{9}Be(d,n)^{9}B reaction with yield 60°and yield 89°. Both curves were fit with a grade 3 polynomial function.

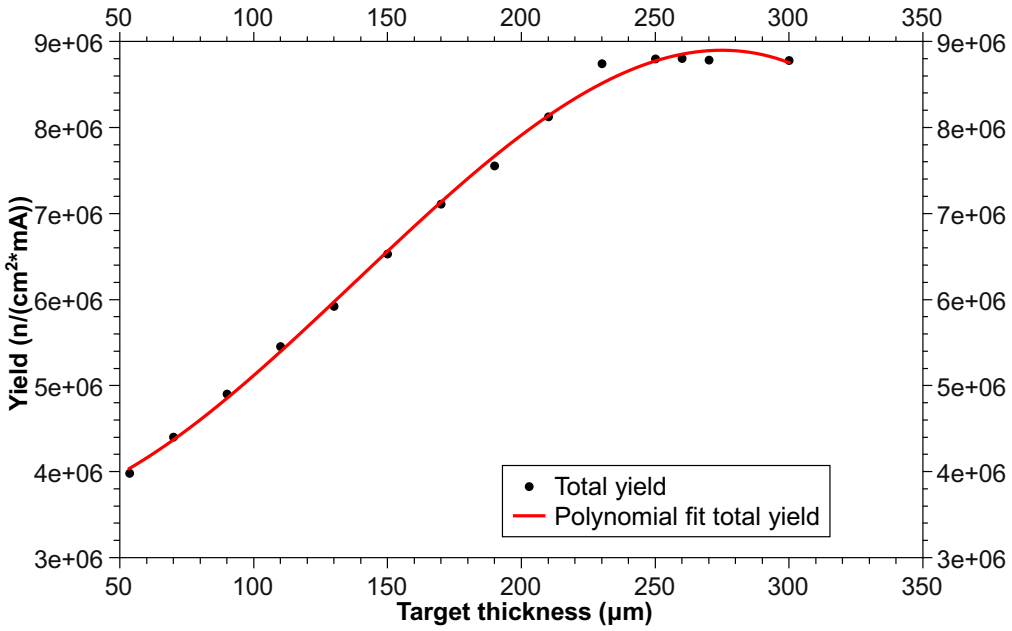

Figure 4.6: Thick target thickness optimization for the ^{9}Be(d,n)^{9}B reaction with total yield. The curve was fit with a grade 3 polynomial function.

Table 4.5: Optimal target thicknesses for the ^{9}Be(d,n)^{9}B reaction given by the grade 3 polynomial fit parameters. These fits are depicted in figures 4.5 and 4.6.

	Thickness (μm)
Total yield	274.92±67.777
Yield 60°	278.57±79.106
Yield 89°	273.53±75.889

4.3 Cyclotron-based neutron beamline

The choice of materials and their thicknesses for all implementation simulations was made based on literature and published data. The main influences were [Lev01, Mau98, Lud97].

The criterion used for choosing the targets thicknesses was the mean of the values given in tables 4.4 and 4.5 for protons and deuterons, respectively.

According to the manufacturer, the cyclotron has a proton beamline with about 80% of the particles inside 10 mm at 30 cm after cyclotron port (section 1.4.2). The simulation study depicted in section 4.1 has shown that, with a sigma of 1.08, 80% of particles are inside 10 mm at 20.72 cm after the double-window system. This was the value used since the Havar®, gaseous helium and aluminum were also simulated in each setup. For deuterons, 70% of the deuterons are inside 10 mm at 12.67 cm, and this was also the value used for the same reason as in the protons case.

All simulations with an implementation setup were performed in air.

Table 4.6: Densities of the materials used in the simulated setups.

Material	Density (g cm^{-3})
Aluminum	2.70
Aluminum fluoride	2.88
Aluminum oxide	3.97
Lead fluoride	7.75
Heavy water	1.1056
Boron carbide	2.52
Bismuth	9.78
Cadmium	8.65

4.3.1 Setups

In all setups, the length of the collimator and the length of the shield of collimator exit is 30 cm and 10 cm, respectively. The purpose of the shield of collimator exit is to prevent the passage of neutrons through the walls of the collimator, therefore imposing to the neutron beam a path throughout the collimator aperture. This shield should be made with a good neutron absorber, such as boronated compounds and polyethylene enriched with lithium fluoride, preferably lithium-6 flouride [Lev01].

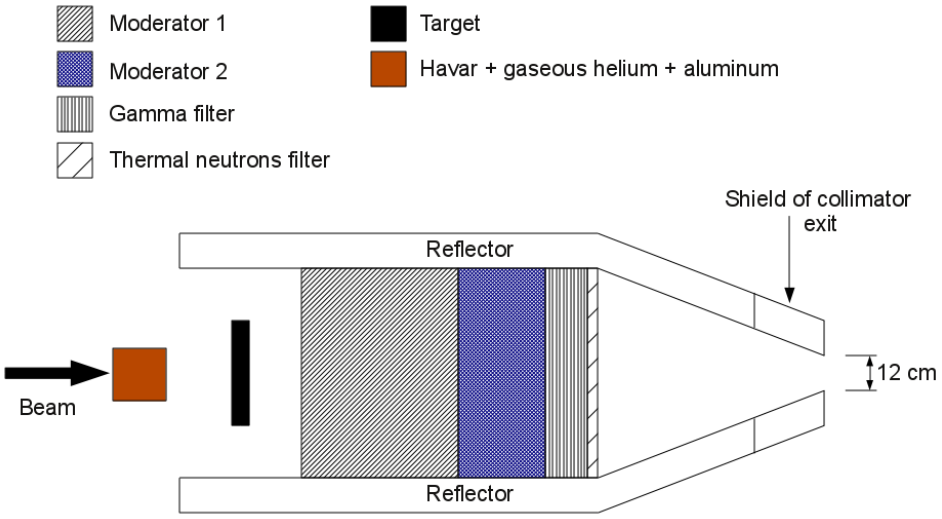

Figure 4.7: Scheme of setup type 1.

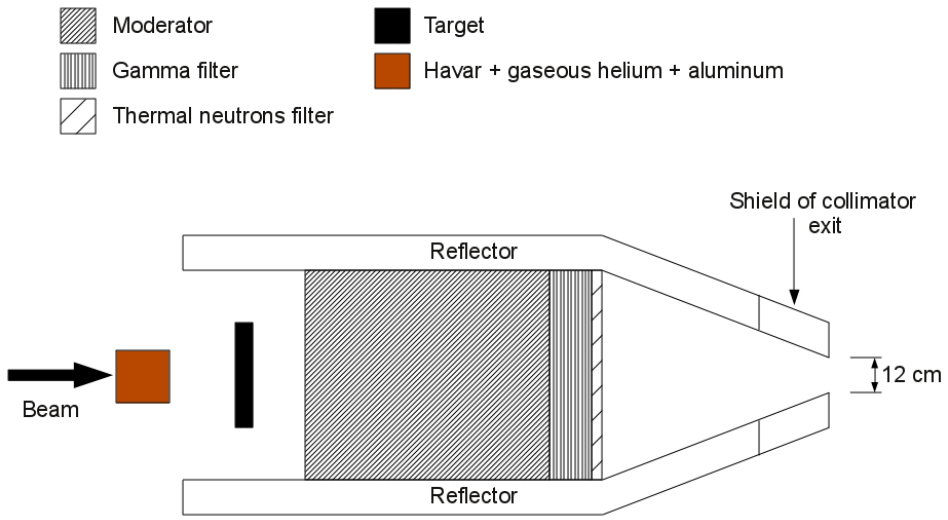

Figure 4.8: Scheme of setup type 2.

Table 4.7: Characteristics of the setups simulated for (p,n) and (d,n) reactions. The setup type column refers to figures 4.7 and 4.8. Only setup 7 was simulated with a deuteron beamline.

Setup number	Setup type	Moderator 1 [thickness (cm)]	Moderator 2 [thickness (cm)]	Reflector [thickness (cm)]
1	1	Aluminum [30]	Aluminum fluoride [20]	Lead fluoride [10]
2	2	Aluminum oxide [50]	—	Lead fluoride [10]
3	1	Aluminum [30]	Aluminum fluoride [20]	Lead fluoride [15]
4	1	Aluminum [36]	Aluminum fluoride [24]	Lead fluoride [10]
5	1	Aluminum [36]	Aluminum oxide [24]	Lead fluoride [10]
6	2	Heavy water [50]	—	Lead fluoride [10]
7	1	Aluminum [30]	Aluminum fluoride [20]	Lead fluoride [15]

Table 4.8: Materials and their thicknesses used for gammas filter, thermal neutrons filter, and shield of collimator exit.

Gamma filter [thickness (cm)]	Thermal neutrons filter [thickness (cm)]	Shield of collimator exit [thickness (cm)]
Bismuth [10]	Cadmium [0.05]	Boron carbide [the same as reflector]

4.3.2 Results

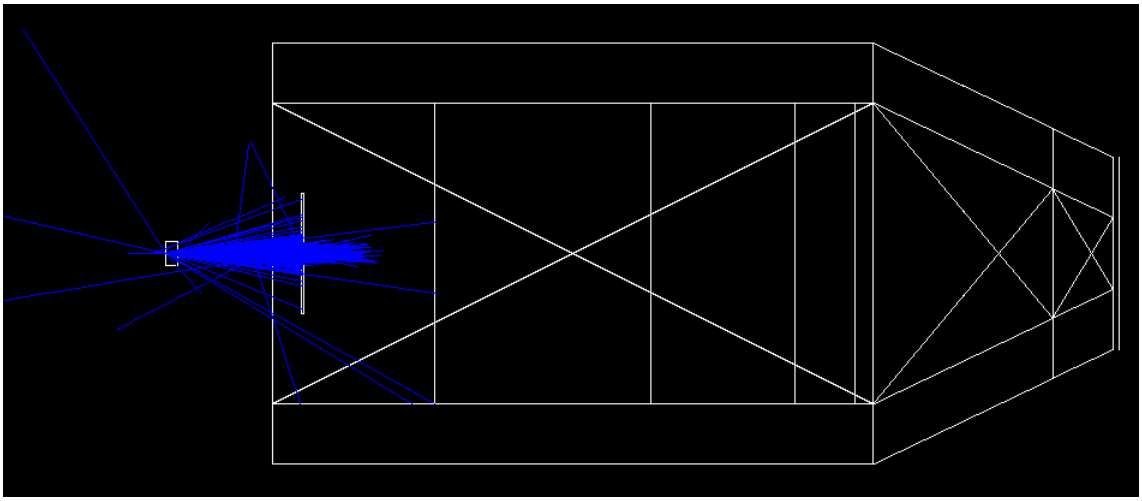

(a) Image with protons only.

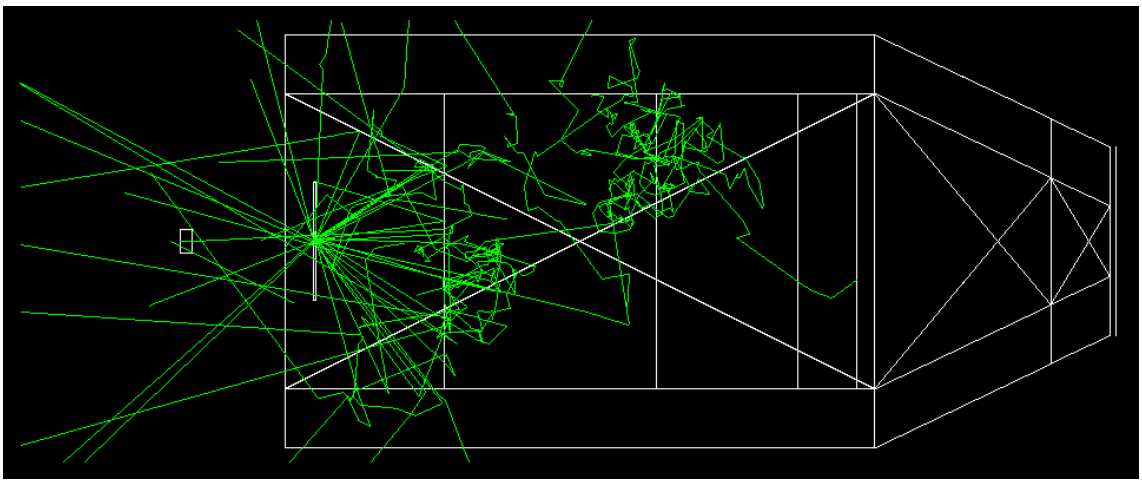

(b) Image with neutrons only.

Figure 4.9: Simulation of a beam with 10000 protons and with a setup type 1 (setup number 1). Both images are from the same simulation, protons being shown in the top, and neutrons in the bottom image.

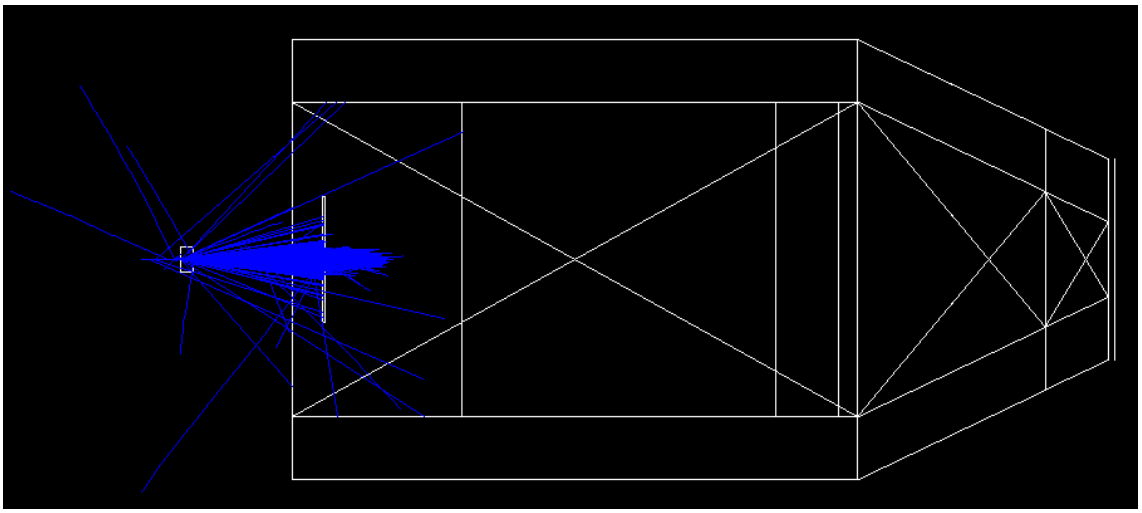

(a) Image with protons only.

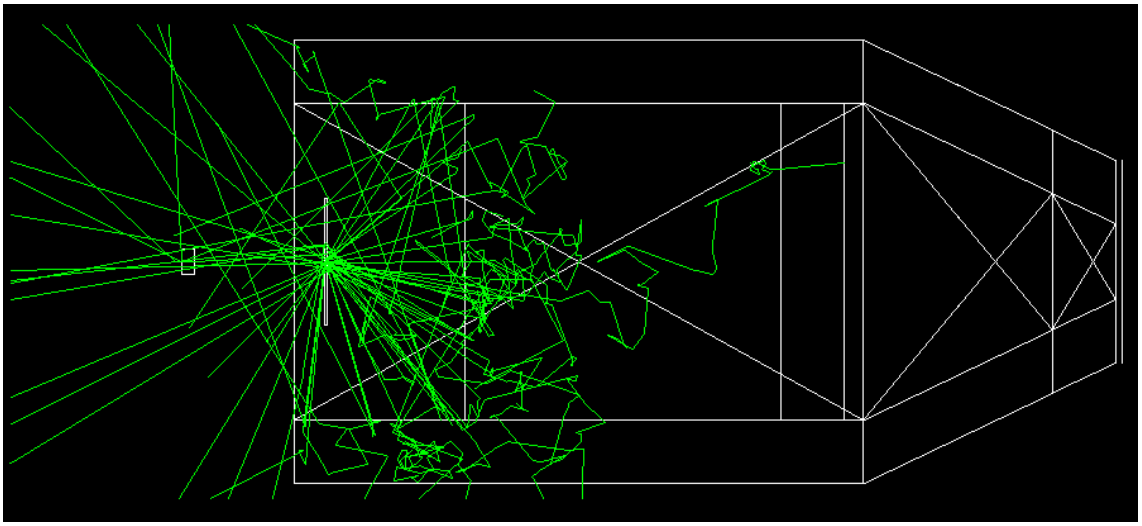

(b) Image with neutrons only.

Figure 4.10: Simulation of a beam with 10000 protons and with a setup type 2 (setup number 2). Both images are from the same simulation, protons being shown in the top, and neutrons in the bottom image.

Table 4.9: Epithermal, fast, and thermal neutrons density flux, and gamma density flux obtained with all (p,n) and (d,n) simulations.

Setup number	**Epithermal neutrons flux density** $(\frac{\times 10^5 \ n}{(150\mu A \times cm^2 \times s)})$	**Fast neutrons flux density** $(\frac{\times 10^5 \ n}{(150\mu A \times cm^2 \times s)})$	**Thermal neutrons flux density** $(\frac{\times 10^3 \ n}{(150\mu A \times cm^2 \times s)})$	**Gamma flux density** $(\frac{\times 10^6 \ n}{(150\mu A \times cm^2 \times s)})$
1	7.4	4.7	0	11.3
2	4.6	1.3	0	6.7
3	13.1	6.6	0	12.4
4	5.4	2.5	0	9.6
5	4.9	1.2	0	9.3
6	0.9	0.6	7.9	2.0
7	1.2	0.3	0	0.9

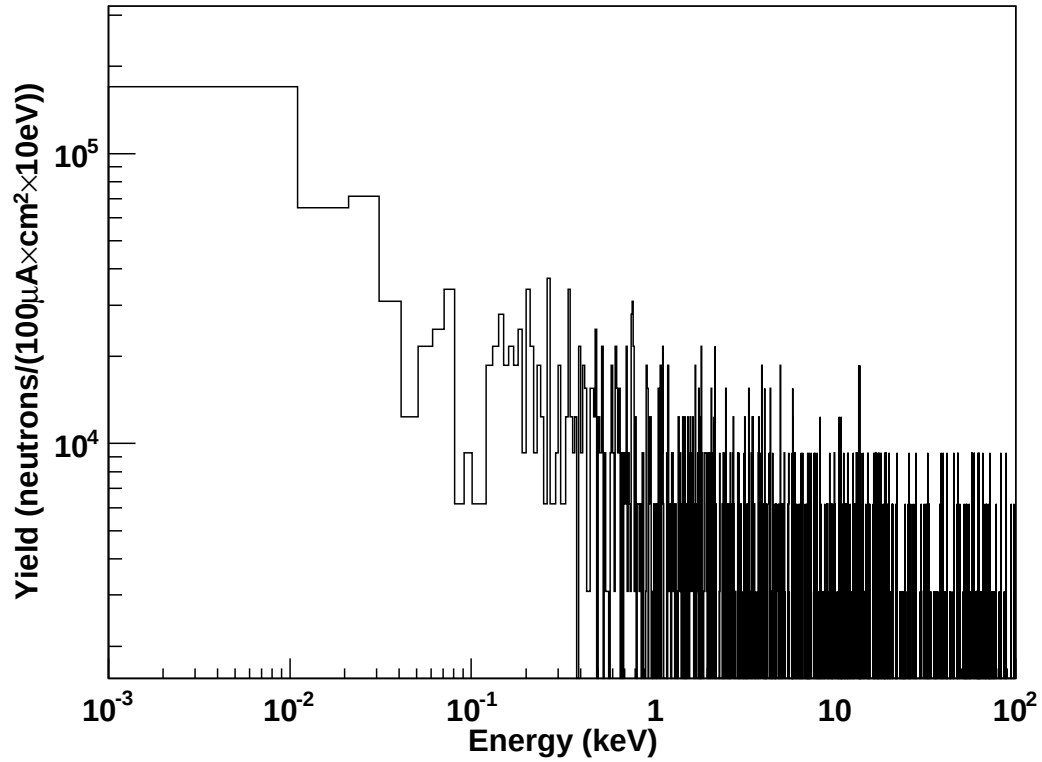

(a) Neutron energies.

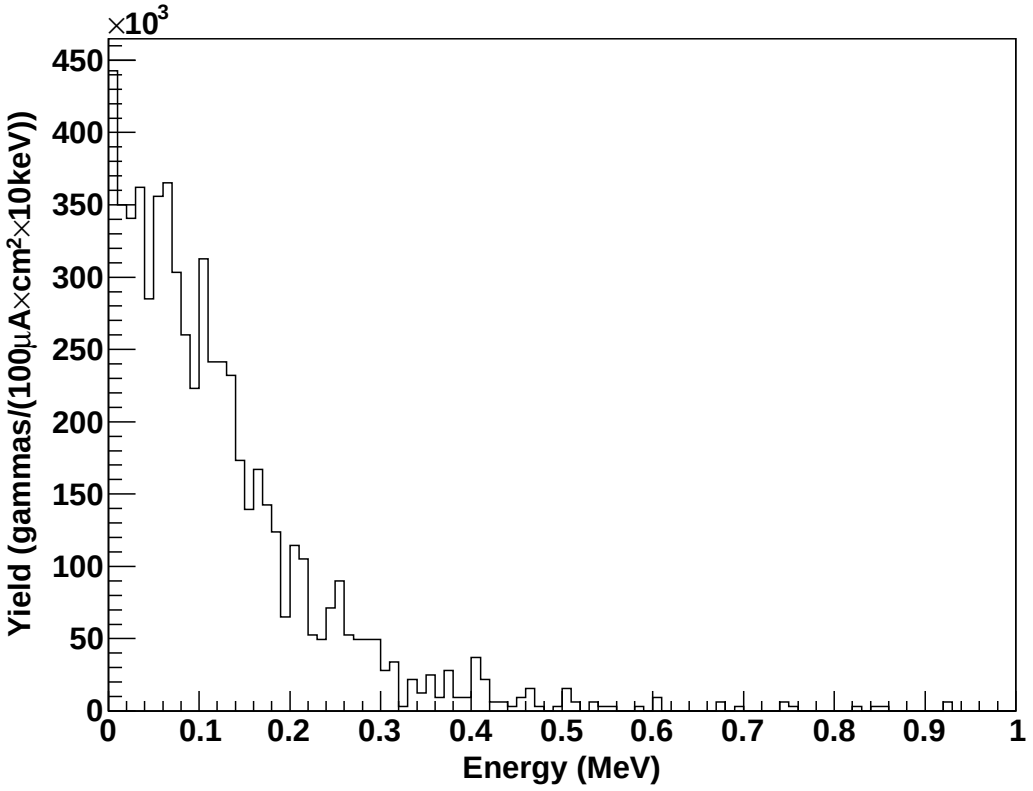

(b) Gamma energies.

Figure 4.11: Energy spectrum of both neutrons and gammas with setup 1. These results were obtained with 1.4×10^9 simulated protons.

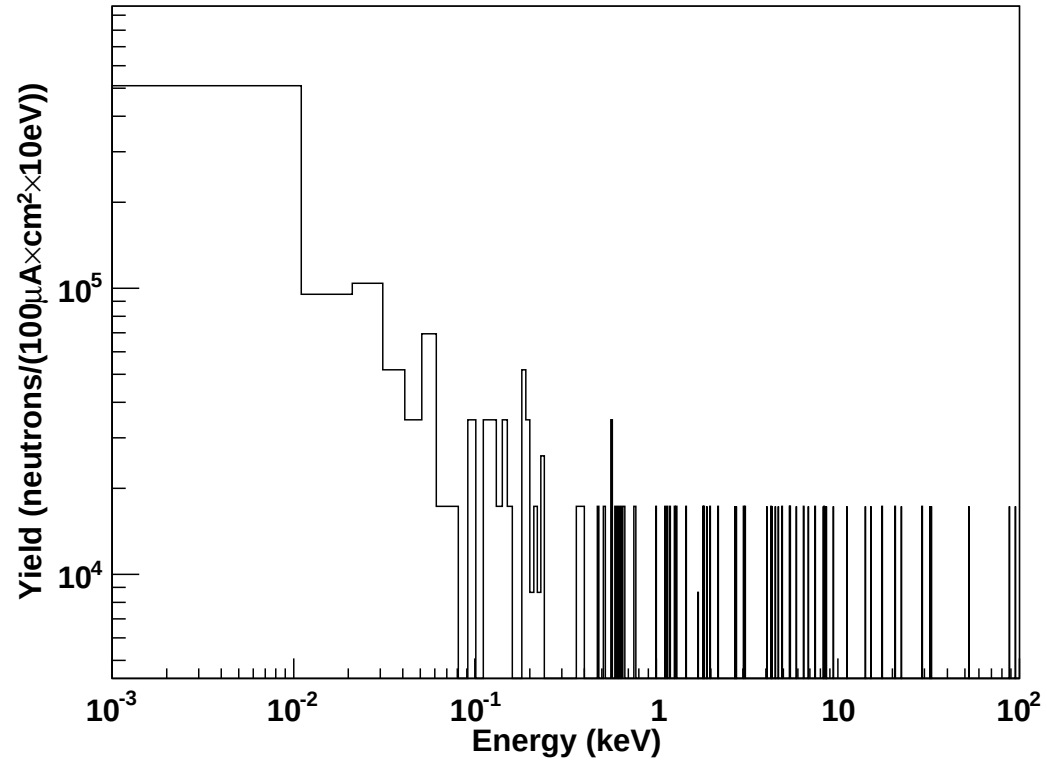

(a) Neutron energies.

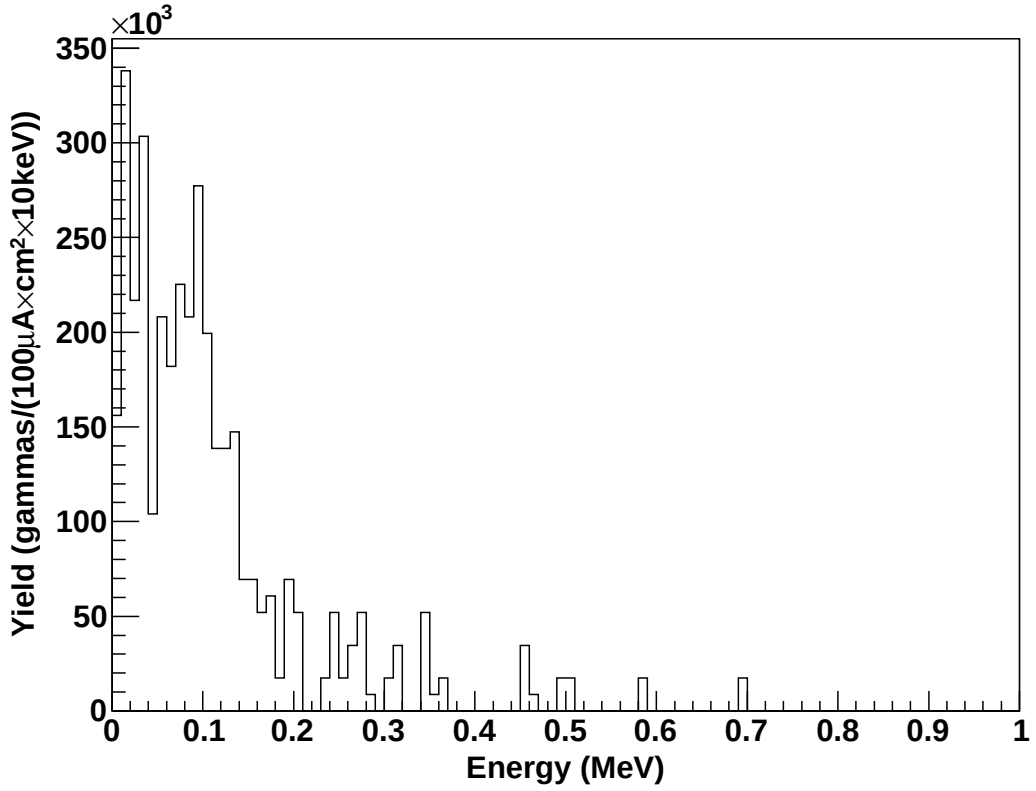

(b) Gamma energies.

Figure 4.12: Energy spectrum of both neutrons and gammas with setup 2. These results were obtained with 500×10^6 simulated protons.

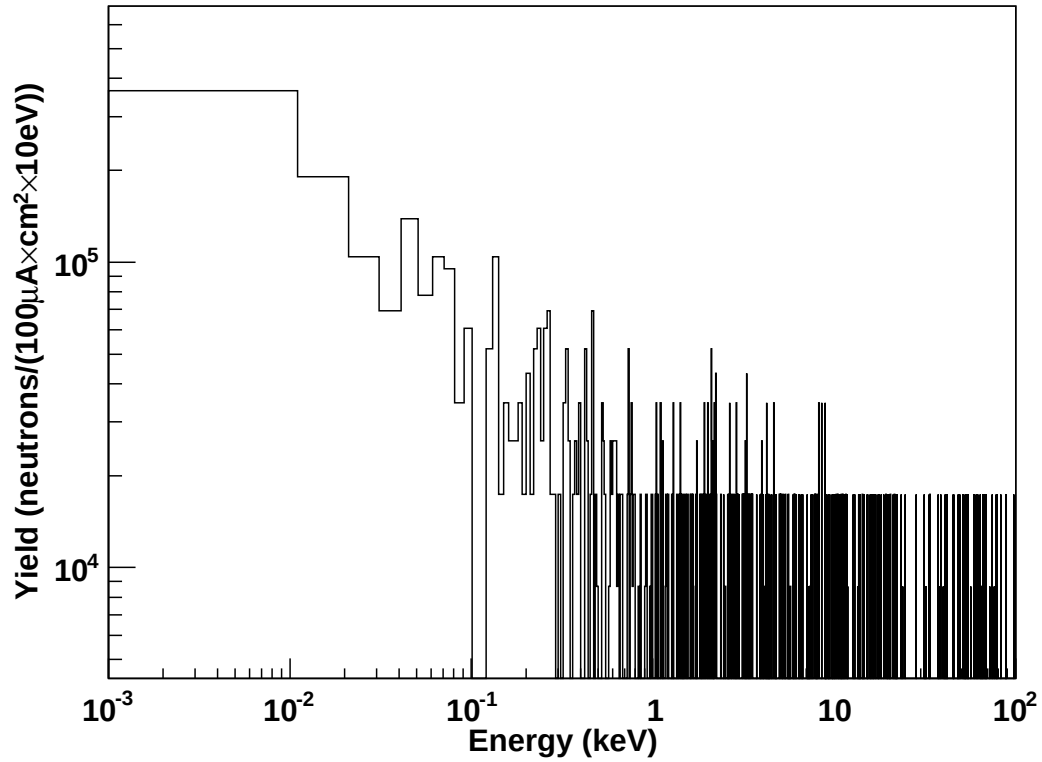

(a) Neutron energies.

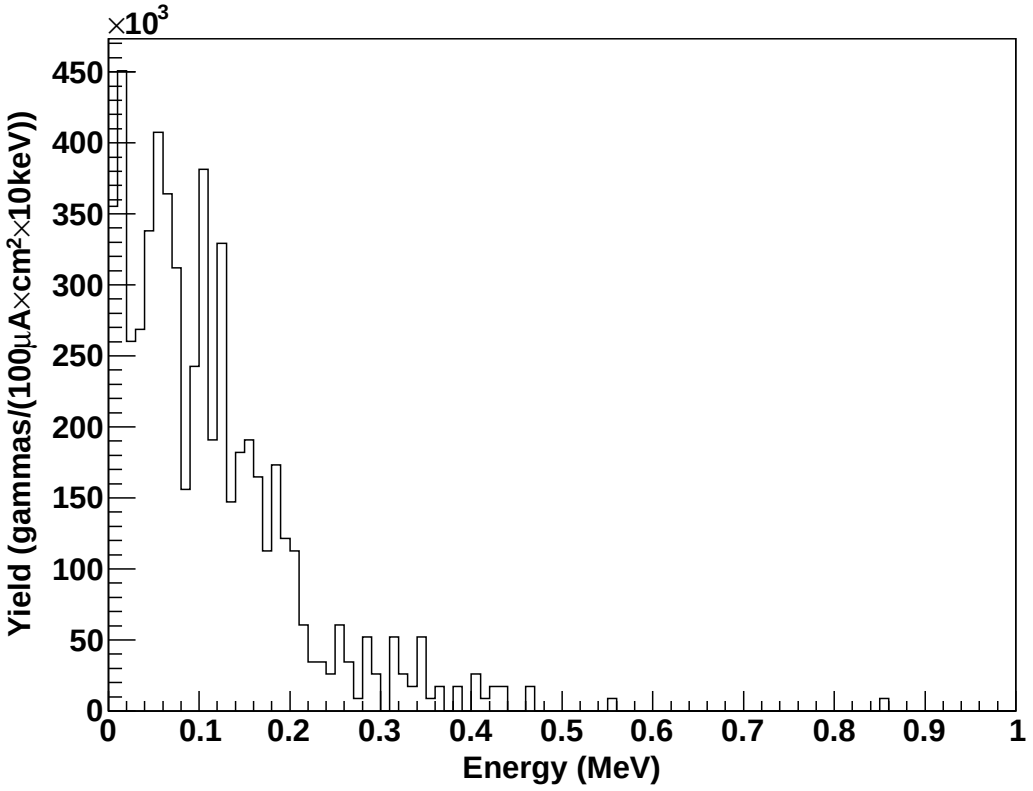

(b) Gamma energies.

Figure 4.13: Energy spectrum of both neutrons and gammas with setup 3. These results were obtained with 500×10^6 simulated protons.

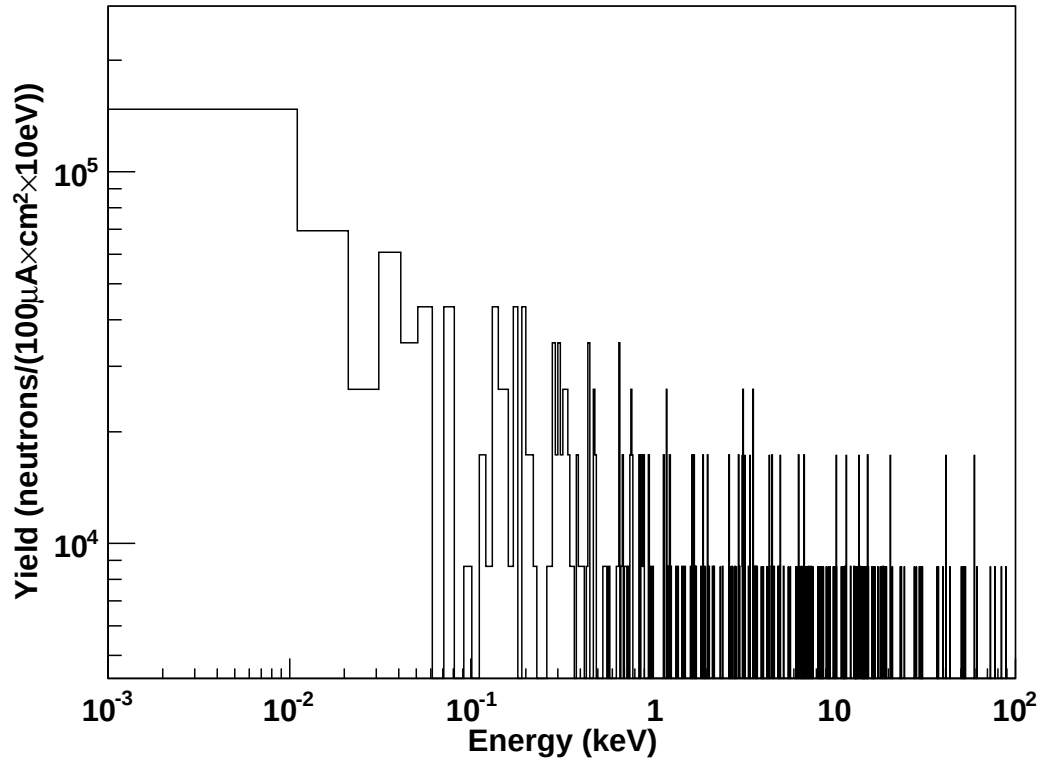

(a) Neutron energies.

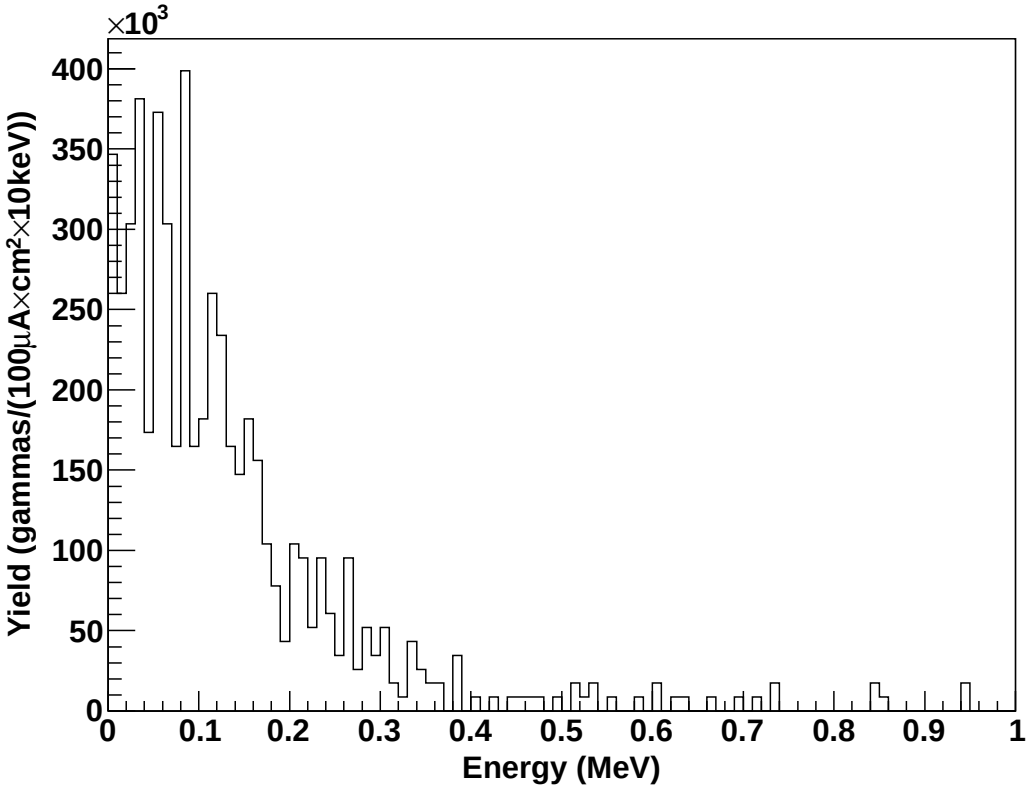

(b) Gamma energies.

Figure 4.14: Energy spectrum of both neutrons and gammas with setup 4. These results were obtained with 500×10^6 simulated protons.

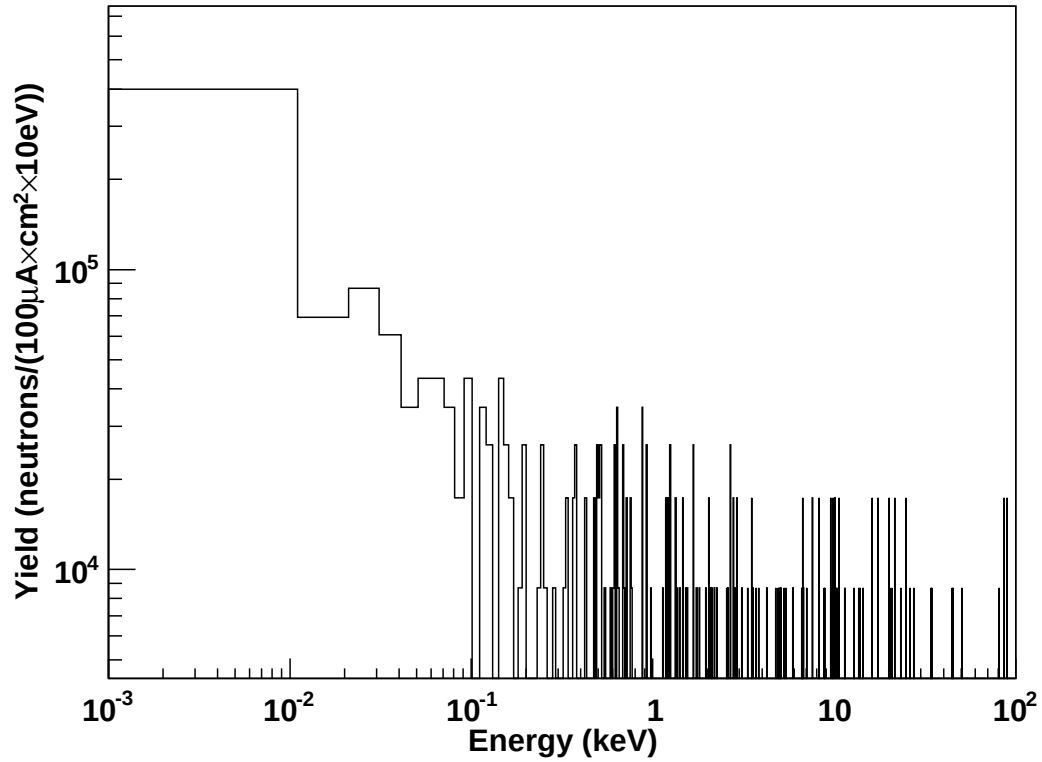

(a) Neutron energies.

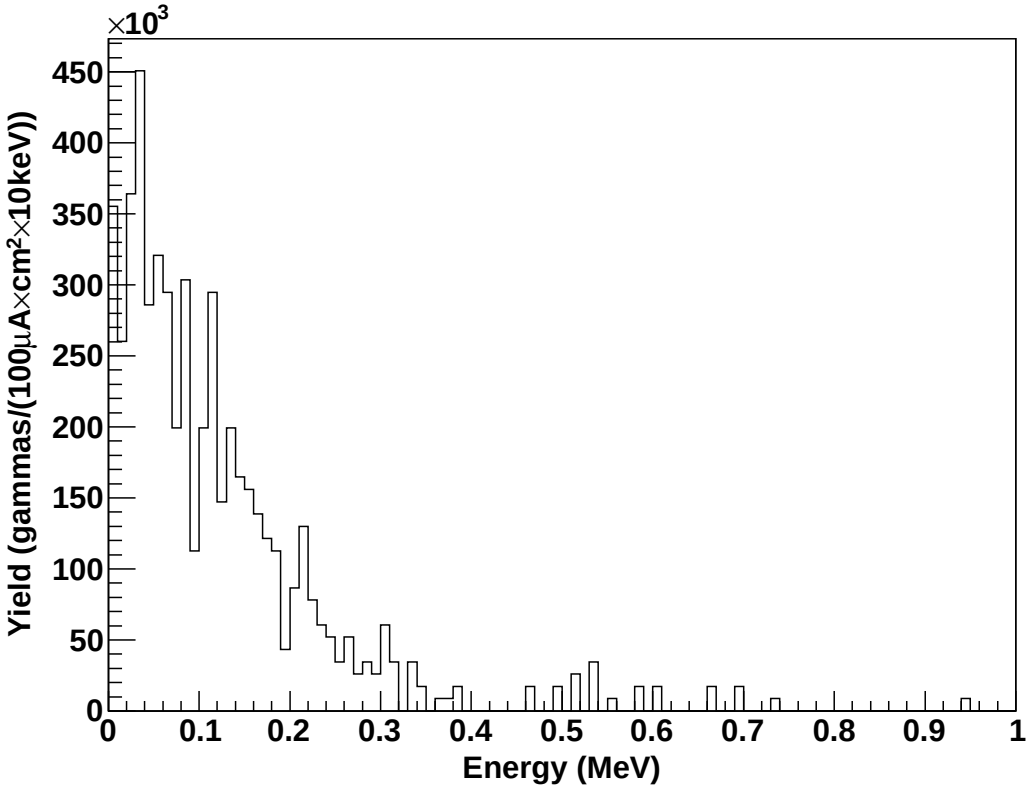

(b) Gamma energies.

Figure 4.15: Energy spectrum of both neutrons and gammas with setup 5. These results were obtained with 500×10^6 simulated protons.

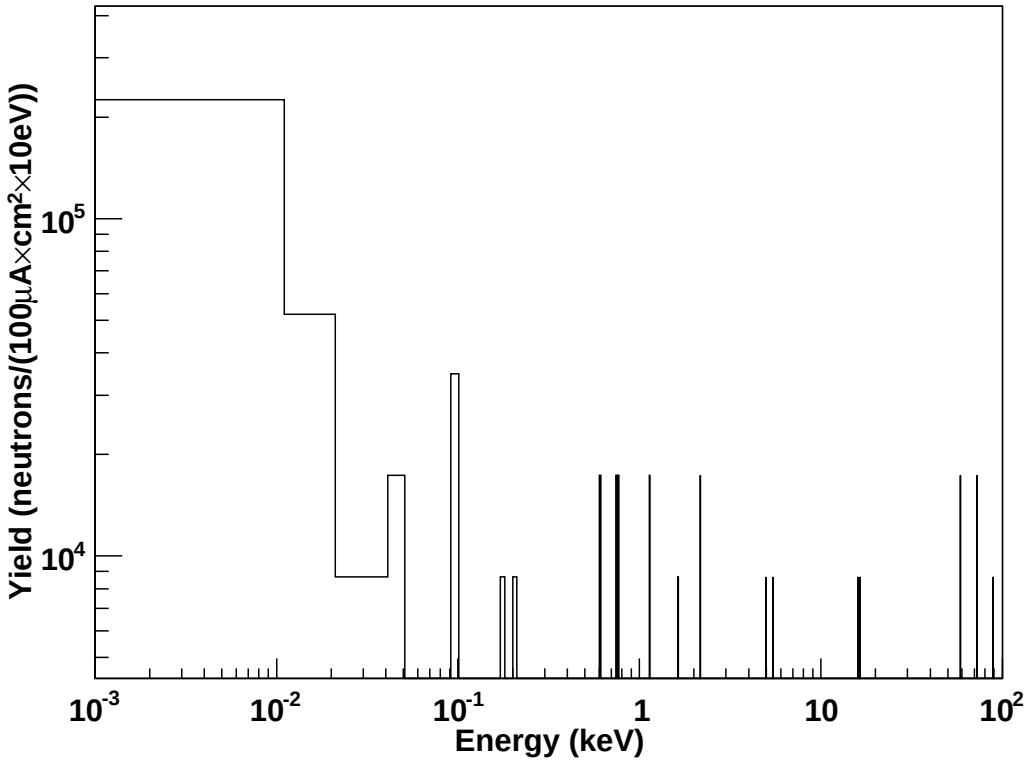

(a) Neutron energies.

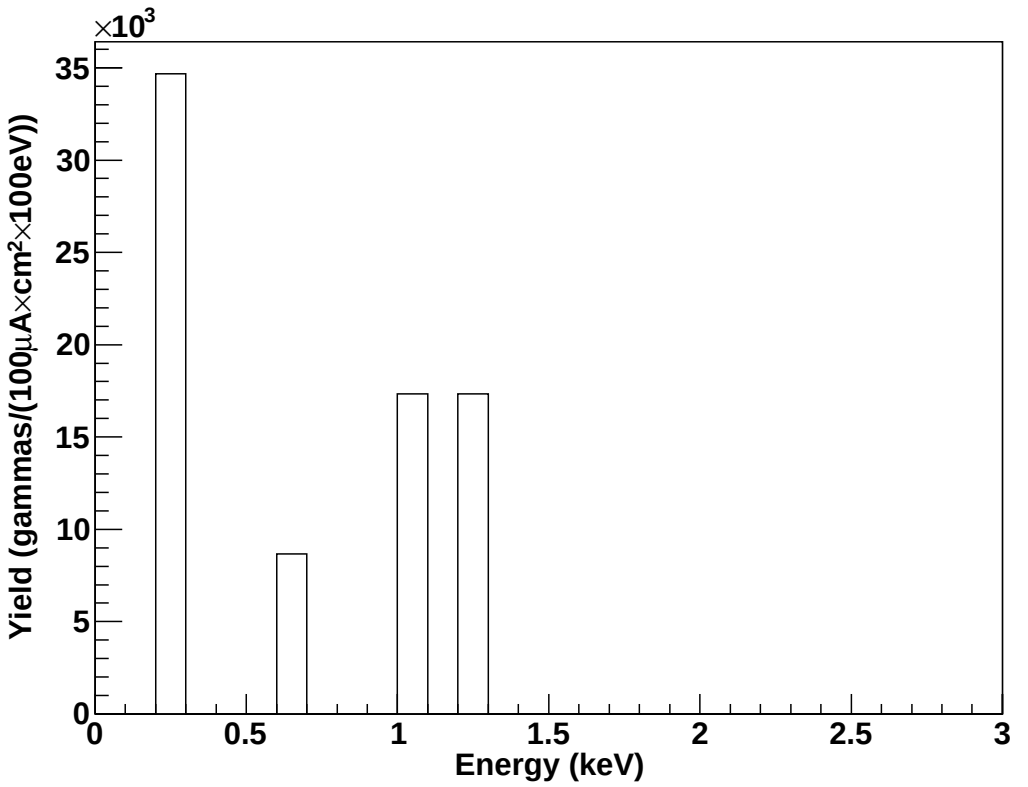

(b) Gamma energies.

Figure 4.16: Energy spectrum of both neutrons and gammas with setup 6. These results were obtained with 500×10^6 simulated protons.

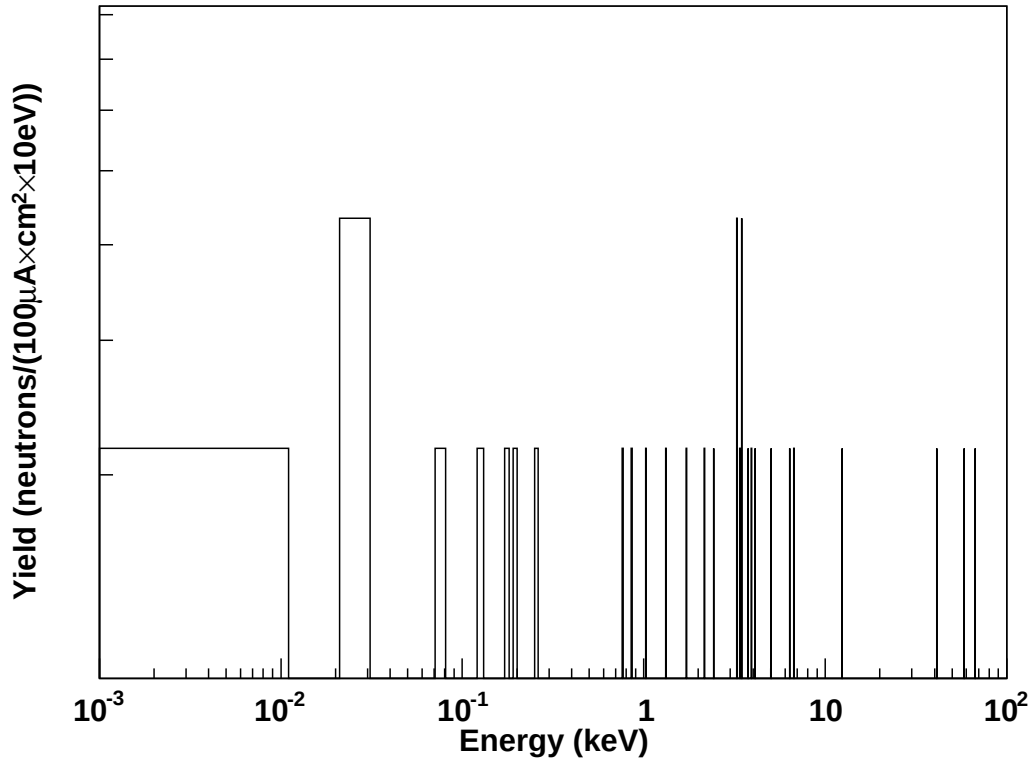

(a) Neutron energies.

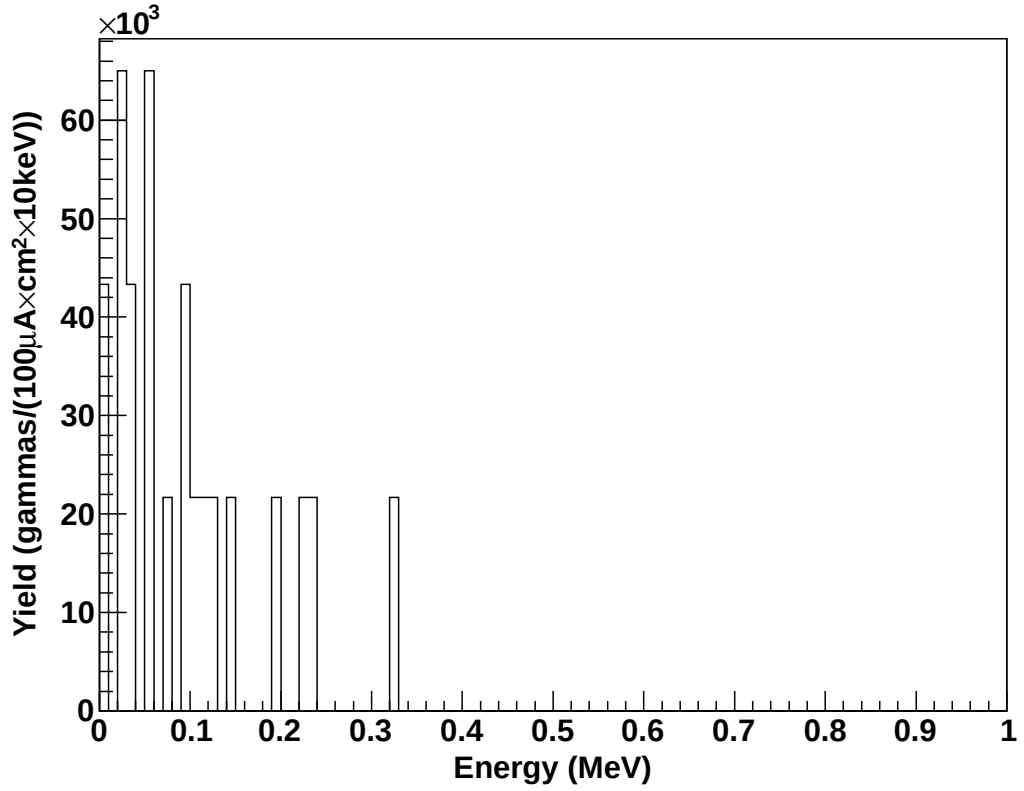

(b) Gamma energies.

Figure 4.17: Energy spectrum of both neutrons and gammas with setup 7. These results were obtained with 200×10^6 simulated deuterons.

4.4 Californium-252-based neutron beamline

4.4.1 Setup

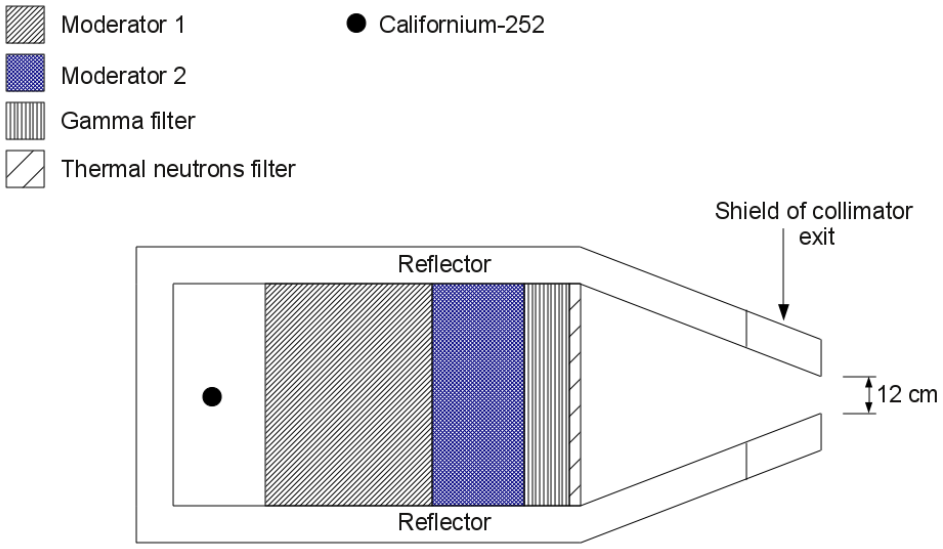

Figure 4.18: Scheme of the setup used for californium-252 simulations.

Table 4.10: Characteristics of the setup simulated with californium-252.

Moderator 1 [thickness (cm)]	Moderator 2 [thickness (cm)]	Reflector [thickness (cm)]
Aluminum [30]	Aluminum fluoride [20]	Lead fluoride [10]

4.4.2 Results

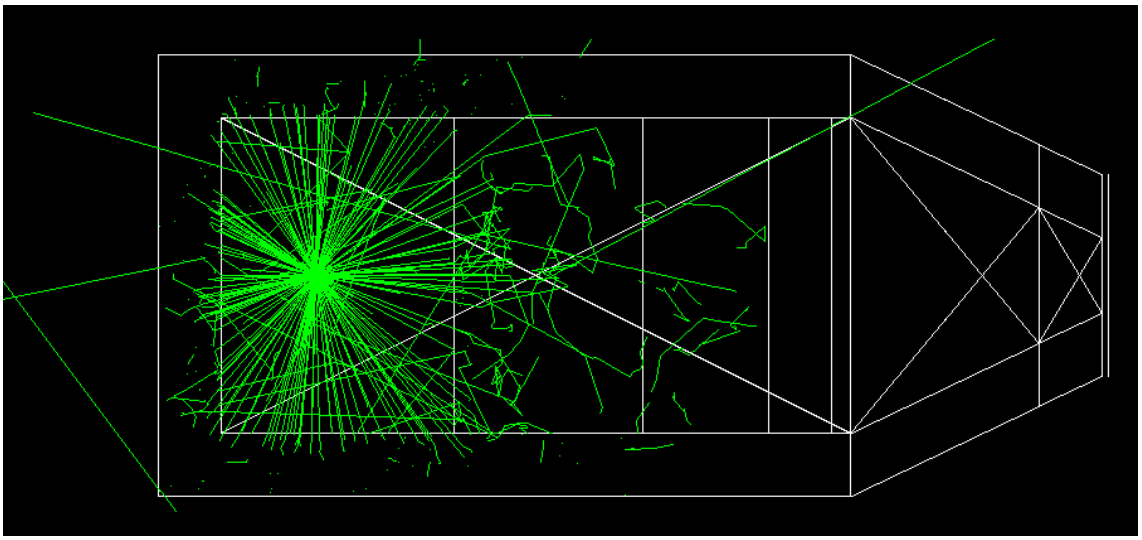

(a) Image with gammas only.

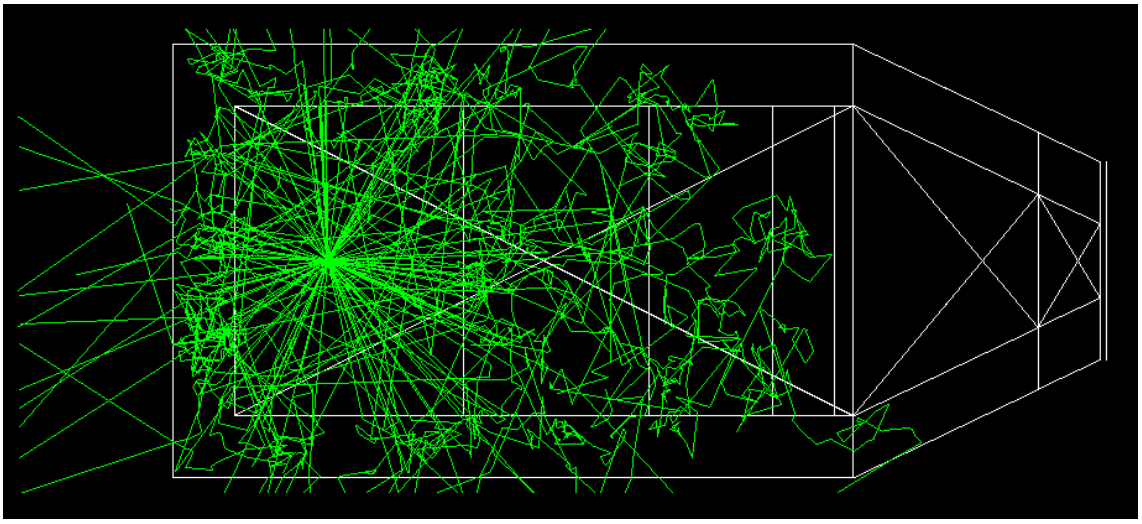

(b) Image with neutrons only.

Figure 4.19: Californium-252 decay simulation with the setup depicted in figure 4.18 and about 21 decays simulated. Both images are from the same simulation, gammas being shown in the top, and neutrons in the bottom image.

Table 4.11: Epithermal, fast, and thermal neutrons density flux, and gamma density flux obtained with the californium-252 setup (figure 4.18).

Epithermal neutrons density flux $\left({}^{n}/_{(cm^2 \times \mu g \times s)}\right)$	**Fast neutrons density flux** $\left({}^{n}/_{(cm^2 \times \mu g \times s)}\right)$	**Thermal neutrons density flux** $\left({}^{n}/_{(cm^2 \times \mu g \times s)}\right)$	**Gamma density flux** $\left({}^{n}/_{(cm^2 \times \mu g \times s)}\right)$
3.6	1.6	0	4.1

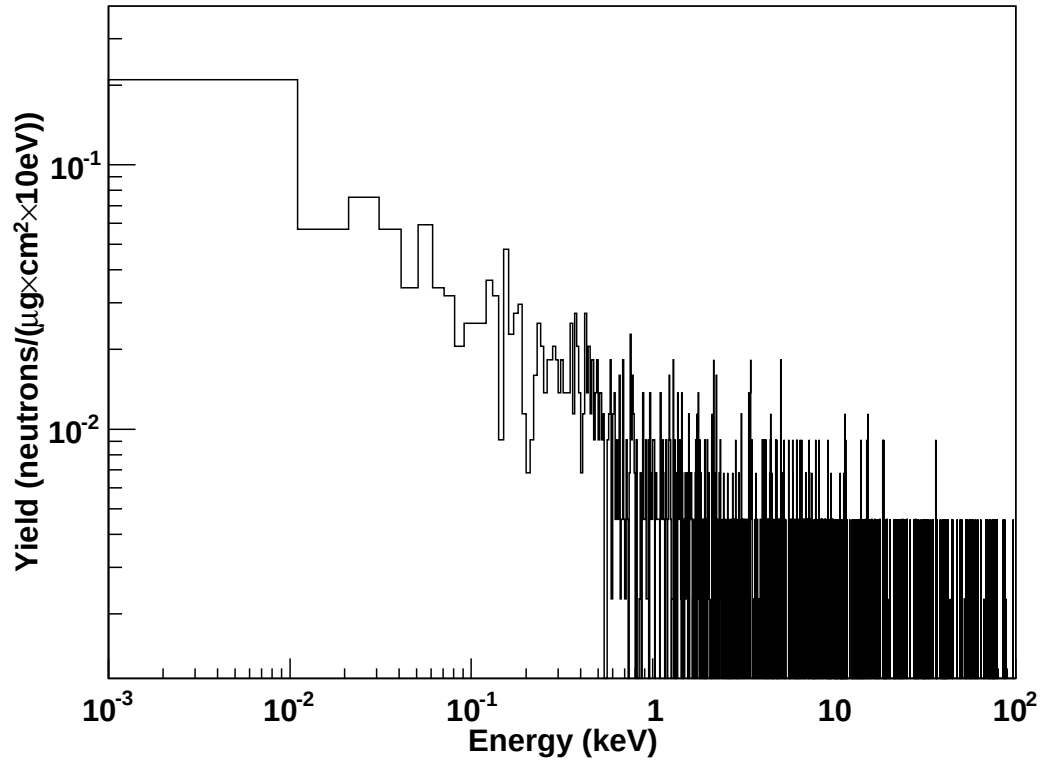

(a) Neutron energies.

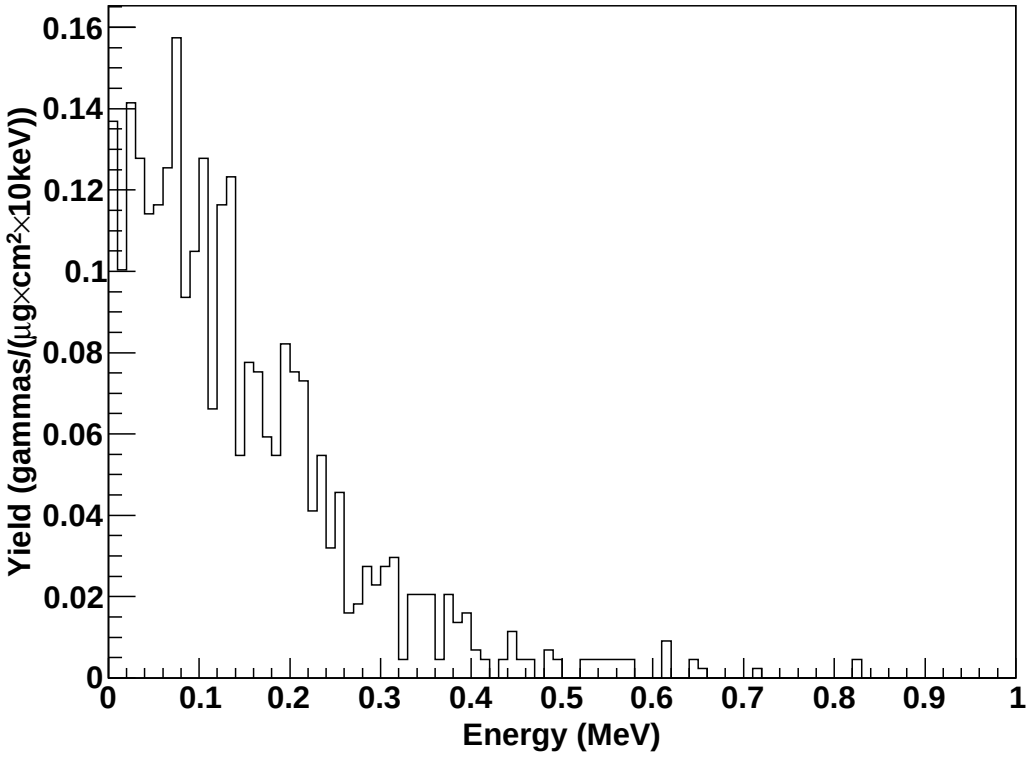

(b) Gamma energies.

Figure 4.20: Energy spectrum of both neutrons and gammas for simulation with californium-252. These results were obtained with 7×10^6 simulated neutrons and considering a source with initial activity.

4.5 Implementation and operational costs

Both cyclotron-based neutron beamline and californium-252-based neutron beamline have advantages and disadvantages in terms of costs. The setup construction for each case is very similar, therefore the costs are nearly the same with some advantage for californium-252-based beamline due to lower neutrons energies and less moderating material needed. Probably, comparing with the other costs, this difference is negligible. However, this implementation analysis is not considering the acquisition of a californium-252 source, whereas the cyclotron is already available at ICNAS. Californium-252 can be bought or be loaned. The loan has some advantages since the initial cost is inferior and the manufacturer is responsible for replacing the source after the loan period (in general five years) or if any capsule defect or damage is detected. The disadvantage of loaning is the existence of a loan fee that goes from about $3000 to about $10000 depending on source mass. Also, the acquisition of a source has some handling and transport fees [Mar99]. The estimated cost for a californium-252 source is detailed in table 4.12, without considering fees.

Table 4.12: Estimated cost for a californium-252 source. Adapted from [Mar99].

Date (month/year)	**Number of sources**	**Requested ^{252}Cf mass per source (μg)**	**Estimated cost**
12/98	1	0.2	$7400
08/98	1	6	$9200
03/99	1	10	$10600
05/99	1	50	$13600
11/98	1	300	$14200
08/98	1	8000	$23000
01/99	2	27000	$51700 (single source $34800)
07/99	2	50000	$80800 (single source $44500)

The operational cost of the cyclotron is around 400€/h [Alv10c] and the californium-252-based neutron beamline does not have any operational cost (not considering staff and consumables in both cases). This difference in the two solutions is the key for choosing between them. If the neutron beamline is to be used intensively (*i.e.*, for long time periods) californium-252 becomes a more affordable solution, if not, the cyclotron is the obvious choice. It is important to consider the decay of californium-252 and to quantify the intensities needed to determine its useful lifetime. Another cost issue is between the use of protons and deuterons. Although the deuterium source is more expensive than the hydrogen source, it seems that this difference is insignificant compared with the cyclotron power consumption [Alv10d].

Part III

Conclusions and future work

Chapter 5

Conclusions and future work

A neutron beamline is an added value to a cyclotron-based facility, since it has a wide range of applications such as basic research, radiobiological and material science studies, and homeland security. The main aim of this thesis work was to provide a first scientific and financial viability analysis of the implementation of a neutron beamline assembled at a low-energy cyclotron machine, which included the specificity of achieving thermal and epithermal neutron flux densities appropriate for radiobiological studies (*i.e.*, with energies below 10 keV).

Before a first-setup cost estimation could be put forward, an effort of estimating by means of Monte Carlo the neutron production yield achievable with an 18-MeV cyclotron-based proton beam was necessary in order to allow estimating with acceptable accuracy the amount and type of material needed for reaching the main goal: a neutron radiobiological setup.

With this objective set, the Geant4 package was chosen as a simulation toolkit. Although Geant4 shows a growing acceptance in the scientific community, due to the ground-breaking aspect inherent to this thesis work, an initial emphasis was dedicated to a thorough, first-step simulation and corresponding validation against published experimental results regarding neutron yield. For this, a thin ^{9}Be target was subject by simulation to a pencil-shaped proton beam, with the results of the reaction ^{9}Be(p,n)^{9}B being collected and compared to experimental data. Three different physical models/packages were tested independently, namely the precompound model, the QGSP_BIC_HP package, and the QGSP_BERT_HP package. All models/packages agreed with experiment in terms of the order of magnitude of absolute double-differential cross-sections, with errors inferior to $\sim$20 % being obtained in all cases, a remarkable achievement in terms of nuclear physics. Due to the better agreement obtained with the QGSP_BERT_HP package, all following simulations regarding first-setup optimization made use of this physics package. Namely, optimization studies were performed regarding (1) the double-window system cyclotron-port made of successive Havar®-Helium-Aluminum materials, (2) ^{9}Be thick-target optimization in terms of neutron yields, and (3) six different moderator/collimator setups, with simulations results showing that the thickness of the reflector material in the neutron-beam collimator can optimize the epithermal flux density by a factor of 2, reaching $\sim 10^{6}$ neutrons/(150μA$\times$s$\times$cm^{2}) after only first educated-guesses regarding the input of moderator thicknesses.

The same conclusions apply to the efforts presented through the remaining scientific fields described in this thesis: the use of beams of deuterons was equally investigated, together with the possibility of using a spontaneously-fissing californium-252 source. In the case of deuteron beams, validation against thin-target ^{9}Be targets were performed, as well as simulations for

thick-targets, a double-window-system-based cyclotron port, and one full moderator/collimator setup.

The results obtained with these first and preliminary simulations show that the flux density is not enough for using in BNCT clinical trials/treatments, unless boronated compounds are improved. However, the flux density achieved can give input to the BNCT main problem: the development and testing of new boronated compounds. Moreover, flux densities in the order of 10^6 neutrons/($150\mu A \times s \times cm^2$), as are the ones obtained in this work, can be used for radiobiological studies. Also, such beam permits the implementation of neutron imaging and neutron imaging activation analysis.

Finally, the simulation of a californium-252 source is not provided by default within Geant4. Therefore, software was constructed within this thesis that allowed introducing fission-physics modelling within Geant4, followed once again by the full simulation of moderaror/collimator setup.

Comparing a californium-252-based neutron beamline with a cyclotron-based one, it can be seen that the former is more disadvantageous. That is due not only to logistic issues (it is not possible to 'turn off' a radioactive source) but also, and mainly, to its high cost, since it is necessary a large mass of californium-252 to produce the required fluxes.

Deuterons should, in theory, yield higher flux densities than protons according to the double differential cross sections of the $^{9}Be(d,n)^{10}B$ reaction. This was not verified in this work, which was unexpected and must be reviewed if an implementation is considered. In order to carry out such review, one must start by collecting more experimental double differential cross section data to make a more accurate validation of Geant4 for (d,n) reactions.

It is important to point out that all simulation/analysis software prepared in the framework of this thesis is now ready for fast and detailed setup optimization by making use of Coimbra's Milipeia high-performance computing cluster. The use of this infrastructure, planned to be available within days, will allow the simulated statistics collected so far, presented throughout this thesis, to be increased by about a factor 100 for each day of simulation burden.

Part IV

Appendices and bibliography

Appendix A

Stopping power

Charged particles lose energy in matter by their electro-magnetic interactions with atomic electrons. This process is called energy loss by ionization. This change in energy per unit distance traversed is called dE/dx, stopping power or Bethe-Bloch equation. The ionization loss depends on the speed of the particle as well as properties of the medium. At small speeds, dE/dx is inversely proportional to the square of the speed. At relativistic speeds, dE/dx passes through a minimum and then grows logarithmically [Roh94].

This equation has different forms because of the many corrections that can be introduced. According to Krane, the Bethe-Bloch equation is given by [Kra88]:

$$\frac{dE}{dx} = \left(\frac{e^2}{4\pi\epsilon_0}\right)^2 \frac{4\pi z^2 N_A Z\rho}{mc^2\beta^2 A}\left[\ln\left(\frac{2mc^2\beta^2}{I}\right) - \ln\left(1 - \beta^2\right) - \beta^2\right] \tag{A.1}$$

Table A.1: Variables and values of the Bethe-Bloch equation according to [Hag02] and [Kra88].

Symbol	Definition	Units or value
$\frac{dE}{dx}$	energy loss	MeV g^{-1} cm^2
A	atomic mass of medium	g mol^{-1}
N_A	Avogadro's number	$6.0221367(36)\times10^{23}$ mol^{-1}
ρ	density of medium	g cm^2
ze	charge of incident particle	
Z	atomic number of medium	
mc^2	electron rest energy	0.51099906(15) MeV
I	mean excitation energy	eV
βc	velocity of the particle	m s^{-1}
ϵ_0	electric constant	C^2 N^{-1} m^{-2}

Appendix B

Havar®

Havar® was originally developed in the late 1940's by the Hamilton Watch Company as an 'unbreakable' mainspring material [Rob03]. As watches moved from spring to battery power, thin Havar® strip found a second life in high strength, non-magnetic, corrosion resistant pressure sensing diaphragms for process control equipment [Rob03].

According to the technical sheet of Havar® [HPM], this material is a heat treatable cobalt base alloy that provides very high strength. The alloy has excellent corrosion resistance and is non-magnetic. Applications have included pressure diaphragms, power springs, gap spacers in magnetic heads, and target foils in nuclear physics [HPM].

Table B.1: Nominal composition of Havar®. After [HPM].

Element	**Elemental percentage**
Cobalt	42.0%
Chromium	19.5%
Nickel	12.7%
Tungsten	2.7%
Molybdenum	2.2%
Manganese	1.6%
Carbon	0.2%
Iron	Balance

Table B.2: Physical properties of Havar®. After [HPM].

Property	**Value**
Density	8.304 g cm^{-3}
Melting point	1480℃
Electrical resistivity @ R. T.	92.0 $\mu\Omega$ cm
Thermal expansion coefficient (0℃ to 50℃)	12.5 $\times$ 10^{-6} $℃^{-1}$
Thermal conductivity	13.0 W m^{-1} K
Magnetic attraction	none

Appendix C

Software and hardware used

C.1 Hardware

For this work, three different machines were used, however the major part of the work was done on machine 1 (table C.1).

Table C.1: Machines used to perfom the simulations

	CPU	Number of cores	RAM Memory
Machine 1	Intel® Core™ 2 Duo T7500 2.20GHz	2	4 GB
Machine 2	Intel® Core™ 2 Quad Q6600 2.40GHz	4	4 GB
Machine 3	Intel® 2140 1.60GHz	2	1 GB

C.2 Geant4 simulation toolkit

Geant4 is a public, costless software toolkit that simulates the passage of particles through matter [Ago03, All06] and relies on Monte Carlo technique to accomplish that. It is a very flexible solution with innumerous models of physics processes in a wide range of energies [Ago03]. It can cover hadronic, electromagnetic and optical interactions and has libraries to a large set of materials, elements and long-lived particles [Ago03, All06]. It is designed to be used as object-oriented language and is implemented in C++ [Ago03].

The hadronic interactions with Geant4 are divided in three major groups: (1) cascade state, (2) pre-equilibrium state, and (3) equilibrium state. Each state has its own models, but in some cases it is not necessary to have a model for each state. For example, interactions at low energy ($<$ 100 MeV) can be modelized without the cascade phase [Wri09a, Ago03]. The cascade state describes the intra-nuclear projectile-nucleon and nucleon-nucleon interactions after the projectile enters the nucleus. The two main models for this phase are the Bertini cascade and binary cascade. The main code for modelization of pre-equilibrium state is the precompound model that takes a nucleus from a highly-excited set of particle-hole states down to equilibrium energy by emitting protons, neutrons, deuterons, tritium nuclei, helium-3 nuclei, and alphas [Wri09a]. The final phase, the equilibrium state, is known also as nuclear evaporation or nucleus de-excitation phase. After the pre-equilibrium phase, the nucleus is supposed to be left in an equilibrium state, in which the excitation energy is shared by a large number

of nucleons. If the excitation energy is higher than the separation energy[1], it can still eject nucleons and light particles (deuterons, tritium nuclei, helium-3 nuclei, and alphas) [Gea09]. The generalized evaporation model (GEM) is an example of an evaporation model.

Geant4 performance

Table C.2: Geant4 performance measured in machine 1 with different setups and reactions.

Setup number (if applicable)	Number of events (or particles)	Simulation time (s)	Geant4 physics used
4	1M	277.92	QGSP_BERT_HP
7	1M	684.96	QGSP_BIC_HP
californium-252	3.2×10^4 neutrons	167.99	QGSP_BERT_HP

C.3 Other software

Besides Geant4 9.3 other software was used.

- **Operating system**: openSuse 11.2 64-bit version (Linux kernel 2.6.31.12)[2]
- **Library for high energy physics**: CLHEP version 2.0.4.5.
- **C++ compiler**: GCC version 4.4.1
- **Geant4 visualization system**: HepRApp version 3.15.0
- **Data analysis**: ROOT framework version 5.26/00 and QtiPlot version 0.9.7.14
- **Error propagation software**: LAB Fit version 7.2.48
- **Numerical computation software**: Octave version 3.2.4

[1] Separation energy is the energy needed to remove a nucleon or other particle from a nucleus

[2] Other versions of openSuse were also used, but almost all simulations were done with openSuse 11.2 64-bit version

Bibliography

[Ago03] S. Agostinelli and others. Geant4 — a simulation toolkit. *Nucl. Instr. and Meth. in Phys. Res. A*, 506(3):250–303, 2003.

[All06] J. Allison and others. Geant4 Developments and Applications. *IEEE Trans. Nucl. Sci.*, 53(1):270–278, 2006.

[Alp98] Edward L. Alpen. *Radiation Biophysics*. Academic Press, 1998.

[Alv08] Francisco J. C. Alves. O ciclotrão e a produção de radionuclídeos. In J. J. Pedroso de Lima, editor, *Física em Medicina Nuclear: Temas e aplicações*, chapter 2. Imprensa da Universidade de Coimbra, 1st edition, 2008.

[Alv10a] Francisco J. C. Alves, August 17^{th} 2010. private communication.

[Alv10b] Francisco J. C. Alves, July 6^{th} 2010. private communication, information given by Michel Guillot, Field Engineer from IBA.

[Alv10c] Francisco J. C. Alves, July 9^{th} 2010. private communication.

[Alv10d] Francisco J. C. Alves, July 6^{th} 2010. private communication.

[And09] Ian S. Anderson, Robert L. McGreevy and Hassina Z. Bilheux, editor. *Neutron Imaging and Applications - A Reference to the Imaging Community*. Springer, 2009.

[Bar92] Rolf F. Barth, Albert H. Soloway, Ralph G. Fairchild and Robert M. Brugger. Boron Neutron Capture Therapy for Cancers: Realities and Prospects. *Cancer*, 70(12):2995–3007, 1992.

[Bar03] Rolf F. Barth. A critical assessment of boron neutron capture therapy: an overview. *J. Neuro. Oncol.*, 62(1-2):1–5, 2003.

[Bar05] Rolf F. Barth, Jeffrey A. Coderre, M. Graça H. Vicente and Thomas E. Blue. Boron Neutron Capture Therapy of Cancer: Current Status and Future Prospects. *Clin. Cancer Res.*, 11(11):3987–4002, 2005.

[Bar09] Rolf F. Barth. Boron neutron capture therapy at the crossroads: Challenges and opportunities. *Appl. Radiat. Isot.*, 67(7-8 Suppl):S3–S6, 2009.

[Bur05] A. A. Burlon, A. J. Kreiner, A. A. Valda, D. M. Minsky, H. R. Somacal, M. E. Debray and P. Stoliar. Optimization of a neutron production target and a beam shaping assembly based on the ^{7}Li(p,n)^{7}Be reaction for BNCT. *Nucl. Instrum. Meth. B*, 229(1):144–156, 2005.

[CER] CERN, European Organization for Nuclear Research. Geant4 Reference Physics Lists. Internet, available August 2010 at `http://geant4.cern.ch/support/proc_mod_catalog/physics_lists/referencePL.shtml`. Last update October 2^{nd}, 2008.

[Chu99] W. T. Chu. Hadron therapy. In W.R. Hendee, editor, *Biomedical Uses of Radiation*, pages 1055–1131. Wiley-VCH Publishers, 1999.

[Cra91] T. W. Crane and M. P. Baker. Neutron Detectors. In D. Riley, N. Ensslin and H. Smith Jr., editor, *Passive Nondestructive Assay of Nuclear Materials*, chapter 13. 1991.

[Cul04] Christopher N. Culbertson and Tatjana Jevremovic. Computational assessment of improved cell-kill by gadolinium-supplemented boron neutron capture therapy. *Phys. Med. Biol.*, 48(23):3943–3959, 2004.

[Eis88] C. M. Eisenhauer and J. B. Hunt. Anisotropic Neutron Emission from a ^{252}Cf Source. *Radiat. Prot. Dosimetry*, 22(4):253–258, 1988.

[Fil95] R. H. Filby. Neutron Activation Analysis. Technical report, International Union of Pure and Applied Chemistry, IUPAC, 1995. Published in Pure&Appl. Chem., vol. 67(11), pp. 1929-1941.

[Fil09] Detlef Filges and Frank Goldenbaum. *Handbook of Spallation Research: Theory, Experiments and Applications*. Wiley, 1st edition, 2009.

[Gah89] R. A. Gahbauer, J. Goodman and T. E. Blue. Some thoughts on tolerance, dose, and fractionation in boron neutron capture therapy. *Basic Life Sci.*, 50:81–85, 1989.

[Gea09] Geant4 team. *Physics Reference Manual*, December 2009. Version: Geant4 9.3.

[Gol73] V. V. Golushko, K. D. Zhuravlev, Yu. S. Zamyatnin, N. I. Kroshkin and V. N. Nefedov. The average number of neutrons emitted in the spontaneous fission of Cm^{244}, Cm^{246}, and Cm^{248}. *Atomic Energy*, 1973.

[Gup94] N. Gupta, R. A. Gahbauer, T. E. Blue and A. Wambersie. Dose prescription in boron neutron capture therapy. *Int. J. Radiat. Oncol. Biol. Phys.*, 28(5):1157–1166, 1994.

[Gup03] N. Gupta, R. A. Gahbauer, T. E. Blue and B. Albertson. Common challenges and problems in clinical trials of boron neutron capture therapy of brains tumors. *J. Neuro. Oncol.*, 62(1-2):197–210, 2003.

[Hag02] K. Hagiwara et al. Review of Particle Physics. *Phys. Rev. D*, 66, 2002. Internet, available Jun. 2005 at `http://pdg.lbl.gov`.

[Hal00] Eric J. Hall. *Radiobiology for the radiologist*. Lippincott Williams & Wilkins, 5th edition, 2000.

[HPM] HPM®: Hamilton Precision Metals. *Havar®*. Available at `www.hpmetals.com/pdfs/Havar.pdf`.

[Ima98] Yoshio Imahori and others. Fluorine–18–Labeled Fluoroboronophenylalanine PET in Patients with Glioma. *J. Nucl. Med.*, 39(2):325–333, 1998.

[Ins] Institute of Atomic and Subatomic Physics, Vienna University of Technology, Vienna, Austria. Neutron radiography. Internet, available August 2010 at `http://www.ati.ac.at/~neutropt/experiments/Radiography/radiography.html`. Last update December 4^{th}, 2001.

[Joe03] Heikki Joensuu and others. Boron neutron capture therapy of brain tumors: clinical trials at the finnish facility using boronophenylalanine. *J. Neurooncol.*, 62(1-2):123–134, 2003.

[Kab97] George W. Kabalka and others. Evaluation of Fluorine–18–BPA–Fructose for Boron Neutron Capture Treatment Planning. *J. Nucl. Med.*, 38(11):1762–1767, 1997.

[Kar97] Yevgeni A. Karelin, Yan N. Gordeev, Valentin I. Karasev, Vyacheslav M. Radchenko, Yevgeni V. Schimbarev and Rostislav A. Kuznetsov. Californium-252 Neutron Sources. *Appl. Radiat. Isot.*, 48(10-12):1563–1566, 1997.

[Kat04] Itsuro Kato and others. Effectiveness of BNCT for recurrent head and neck malignancies. *Appl. Radiat. Isot.*, 61(5):1069–1073, 2004.

[Kig03] W. S. Kiger III, M. R. Palmer, K. J. Riley, R. G. Zamenhof and P. M. Busse. Pharamacokinetic modeling for boronophenylalanine-fructose mediated neutron capture therapy: ^{10}B concentration predictions and dosimetric consequences. *J. Neuro. Oncol.*, 62(1-2):171–186, 2003.

[Kor04] M. Kortesniemi, T. Seppälä, I. Auterinen and S. Savolainen. Enhanced blood boron concentration estimation for BPA-F mediated BNCT. *Appl. Radiat. Isot.*, 61(5):823–827, 2004.

[Kra88] Kenneth S. Krane. *Introductory Nuclear Physics*. John Wiley & Sons, Inc., 1st edition, 1988.

[Leh06] Eberhard H. Lehmann. Scientific Reviews: Using Neutron Imaging Methods for Non-Invasive Investigation of Museum Objects. *Neutron News*, 2006.

[Lev01] V. Levin, P. Andreo and B. Dodd. Current status of neutron capture therapy. Technical report, International Atomic Energy Agency, May 2001.

[Lud97] B. A. Ludewigt and others. Clinical requirements and accelerator concepts for BNCT. In *IEEE particle accelerator conference*, Vancouver (Canada), May 1997.

[Mar99] R. C. Martin, J. B. Knauer and P. A. Balo. Production, Distribution, and Applications of Californium-252 Neutron Sources. Technical report, Oak Ridge National Laboratory, 1999.

[Mau98] Marko Maučec. Conceptual Design of Epithermal Neutron Beam for BNCT in the Thermalizing Column of TRIGA Reactor. In *Nuclear Energy in Central Europe*, Slovenia, September 1998.

[Mor01] G. M. Morris, P. L. Micca, M. Rezvani, J. W. Hopewell and J. A Coderre. Boron neutron capture therapy: effects of split dose and overall treatment time. *J. Neurooncol.*, 52(2):101–110, 2001.

[Nak03] Yoshinobu Nakagawa, Kyonghon Pooh, Toru Kobayashi, Teruyoshi Kageji, Shinichi Uyama, Akira Matsumura and Hiroaki Kumada. Clinical review of the Japanese experience with boron neutron capture therapy and a proposed strategy using epithermal neutron beams. *J. Neuro. Oncol.*, 62(1-2):87–99, 2003.

[Nia98] A. H. W. Nias. *An Introduction to Radiobiology*. Wiley, 2nd edition, 1998.

[Par08] S. K. Paranjpe and others. Neutron Imaging: A Non-Destructive Tool for Materials Testing. Technical report, International Atomic Energy Agency, September 2008.

[Pau05] Paulo Alexandre Vieira Crespo. *Optimization of In-Beam Positron Emission Tomography for Monitoring Heavy Ion Tumor Therapy*. PhD thesis, Technischen Universität Darmstadt, Germany, 2005.

[Phy] Physics Laboratory, National Institute of Standards and Technology, USA. Stopping-power and range tables for protons. Internet, available August 2010 at `http://physics.nist.gov/PhysRefData/Star/Text/PSTAR.html`. Last update August 23^{rd}, 2010.

[Pod06] E. B. Podgorsăk. *Radiation Physics for Medical Physicists*. Biological and Medical Physics, Biomedical Engineering. Springer, 1st edition, 2006.

[Rao78] U. S. Rao, Arun Kumar, S. C. Misra, P. S. Nagarajan and U.C. Gupta. Anisotropic neutron emission from laboratory sources. *Nucl. Instrum. Methods*, 155(1-2):249–252, 1978.

[Reu08] Paul Reuss. *Neutron Physics*. EDP Sciences, 2008.

[Rob03] Mark Robinson. Havar® a New, Old Co-Cr Biocompatible Alloy for Implants. In Sanjay Shrivastava, editor, *Medical Device Materials: Proceedings of the Materials & Processes for Medical Devices Conference*, pages 324–328, Anaheim, California, USA, September 2003. ASM International.

[Roh94] James William Rohlf. *Modern Physics from α to Z^0*. Wiley, 1st edition, 1994.

[Ryy02] Päivi Ryynänen, Aki Kangasmäki and others. Non-linear model for the kinetics of ^{10}B in blood after BPA-fructose complex infusion. *Phys. Med. Biol.*, 47(5):737–745, 2002.

[Sal04] C. Salt, A. J. Lennox, M. Takagaki, J. A. Maguire and N. S. Hosmane. Boron and gadolinium neutron capture therapy. *Russian Chemical Bulletin, International Edition*, 53(9):1871–1888, 2004.

[Sch] B. Schillinger and others. Neutron imaging at the neutron radiography and tomography facility ANTARES. Internet, available August 2010 at `http://www.frm2.tum.de/fileadmin/stuff/events/VDI_WExpertenforum/talks/TUM-Industrietag_Schillinger.pdf`. Last update October 21^{st}, 2006.

[Smi57] A. B. Smith, P. R. Fields and J. H. Roberts. Spontaneous Fission Neutron Spectrum of Cf^{252}. *Phys. Rev.*, 108(2):411–413, 1957.

[Soc] European Nuclear Society. Ionizaton chamber. Internet, available August 2010 at `http://www.euronuclear.org/info/encyclopedia/i/ionizationchamber.htm`. Last update July 14^{th}, 2010.

[Sol97] Albert H. Soloway, Rolf F. Barth, Reinhard A. Gahbauer, Thomas E. Blue and Joseph H. Goodman. The rationale and requirements for the development of boron neutron capture therapy of brain tumors. *J. Neuro. Oncol.*, 33(1-2):9–18, 1997.

[Sta01] Gelsomina De Stasio and others. Gadolinium in Human Glioblastoma Cells for Gadolinium Neutron Capture Therapy. *Cancer Res.*, 61(10):4272–4277, 2001.

[Sta05] Gelsomina De Stasio and others. Are gadolinium contrast agents suitable for gadolinium neutron capture therapy? *Neurol. Res.*, 27(4):387–398, 2005.

[Sun05] N. Suntharalingam, E. B. Podgoršak and J. H. Hendry. Basic radiobiology. In E. B. Podgoršak, editor, *Radiation Oncology Physics: A Handbook for Teachers and Students*, chapter 14, pages 485–504. International Atomic Energy Agency, 1st edition, 2005. Available August 2010 at `http://www-naweb.iaea.org/nahu/dmrp/syllabus.shtm`.

[Tak03] S. Takács, Z. Szűcs, F. Tárkányi, A. Hermanne, M. Sonck. Evaluation of proton induced reactions on ^{100}Mo: New cross sections for production of ^{99m}Tc and ^{99}Mo. *J. Radioanal. Nucl. Ch.*, 257(1):195–201, 2003.

[Tak05] Kazunori Takahashi and others. Synthesis and in vivo biodistribution of BPA–Gd–DTPA complex as a potential MRI contrast carrier for neutron capture therapy. *Bioorg. Med. Chem.*, 13(3):735–743, 2005.

[Tam08] C. Tamburella and T. J. Giles. Beam diagnostics for an 18 MeV medical cyclotron. *Nucl. Instr. and Meth. in Phys. Res. B*, 266(19-20):4678–4681, 2008.

[Val99] Timothy E. Valentine. Evaluation of prompt fission gamma ray for use in simulating nuclear safeguard measurements. Technical report, Oak Ridge National Laboratory, 1999.

[Vei09] K. G. Veinot and J. S. Bogard. Anisotropy factors for a ^{252}Cf source. *Nucl. Technol.*, 168(2):364–368, 2009.

[Ver69] Victor V. Verbinski and Walter R. Burrus. Direct and Compoud-Nucleus Neutrons from 14-18-MeV Protons on ^{9}Be, ^{14}N, ^{27}Al, ^{56}Fe, ^{115}In, ^{181}Ta, and ^{208}Pb and from 33-MeV Bremsstrahlung on ^{27}Al, ^{206}Pb, and ^{209}Bi*. *Phys. Rev.*, 177(4):1671–1686, 1969.

[Wea73] K. A. Weaver, J. D. Anderson, H. H. Barschall and J. C. Davis. Neutrons from the Bombardment of Beryllium by Deuterons. *Phys. Med. Biol.*, 18(1):64–70, 1973. Note: the cross section data was gathered from the Experimental Nuclear Reaction Data (EXFOR) from the International Atomic Energy Agency, available at `http://www-nds.iaea.org/exfor/exfor.htm`.

[Whi73] Donald H. White and Toufiq A. Siddiqi. Gamma-ray spectra and positive parity bands in ^{158}Gd. *Nucl. Phys. A*, 217(2):410–419, 1973.

[Win] Mark Winter. WebElements Periodic Table of the Elements. Internet, available August 2010 at `http://www.webelements.com`. Last update August 23rd, 2010.

[Wri09a] Dennis Wright. Hadronic Physics I. Internet, available August 2010 at `http://geant4.slac.stanford.edu/SLACTutorial09/Agenda.html`, November 2009. SLAC Geant4 Tutorial.

[Wri09b] Dennis Wright. Physics I: Physics Lists. Internet, available August 2010 at `http://geant4.slac.stanford.edu/SLACTutorial09/Agenda.html`, November 2009. SLAC Geant4 Tutorial.

Acknowledgements

First I would like to thank Prof. Dr. Rui Ferreira Marques, Prof. Dr. Francisco Alves, and Prof. Dr. Paulo Crespo for making the concretization of this work possible. I thank them for their permanent availability, help and scientific guidance.

This project began by the initiative of Prof. Luís F. Metello who established the institutional contacts. Many thanks.

I also would like to express my gratitude to Prof. Dr. Filomena for showing availability for supporting this work.

I also would like to thank LIP and ITN for all the support and ISEC by sharing the computational resources available. For ITN, my acknowledgements go to Prof. Dr. Pedro Vaz and to Prof. Dr. José Marques.

I can not forget my family and the enormous support given by them, mãe, pai e Sara, muito obrigado por tudo.

Finally I would like to express my gratitude to the one who always followed this work with me and always stood there for me, obrigado Micaela.